

Wind Farm Characterization and Control using Coherent Doppler Lidar

by

Raghavendra Krishnamurthy

A Dissertation Presented in Partial Fulfillment
of the Requirements for the Degree
Doctor of Philosophy

Approved April 2013 by the
Graduate Supervisory Committee:

Ronald Calhoun, Chair
Kangping Chen
Huei-Ping Huang
Matthew Fraser
Patrick Phelan

ARIZONA STATE UNIVERSITY

May 2013

ABSTRACT

Wind measurements are fundamental inputs for the evaluation of potential energy yield and performance of wind farms. Three-dimensional scanning coherent Doppler lidar (CDL) may provide a new basis for wind farm site selection, design, and control. In this research, CDL measurements obtained from multiple wind energy developments are analyzed and a novel wind farm control approach has been modeled.

The possibility of using lidar measurements to more fully characterize the wind field is discussed, specifically, terrain effects, spatial variation of winds, power density, and the effect of shear at different layers within the rotor swept area. Various vector retrieval methods have been applied to the lidar data, and results are presented on an elevated terrain-following surface at hub height. The vector retrieval estimates are compared with tower measurements, after interpolation to the appropriate level. CDL data is used to estimate the spatial power density at hub height. Since CDL can measure winds at different vertical levels, an approach for estimating wind power density over the wind turbine rotor-swept area is explored. Sample optimized layouts of wind farm using lidar data and global optimization algorithms, accounting for wake interaction effects, have been explored.

An approach to evaluate spatial wind speed and direction estimates from a standard nested Coupled Ocean and Atmosphere Mesoscale Prediction System (*COAMPS*) model and CDL is presented. The magnitude of spatial difference between observations and simulation for wind energy assessment is researched. Diurnal effects and ramp events as estimated by CDL and COAMPS were inter-compared.

Novel wind farm control based on incoming winds and direction input from CDL's is developed. Both yaw and pitch control using scanning CDL for efficient wind farm control is analyzed. The wind farm control optimizes power production and reduces loads on wind turbines for various lidar wind speed and direction inputs, accounting for wind farm wake losses and wind speed evolution. Several wind farm control configurations were developed, for enhanced integrability into the electrical grid. Finally, the value proposition of CDL for a wind farm development, based on uncertainty reduction and return of investment is analyzed.

I dedicate this dissertation to my Parents (N. Krishnamurthy and Sheela), who have always had the wisdom to stand back and guide me in every step of my life. I also dedicate this to my brother, Santosh, and Sister-in-law, Sujatha, who are an ever-present source of inspiration and encouragement in my life. To my niece, Sanjana, and nephew, Shreyas, who remind me that it is the simple things in life that deserve the smiles.

ACKNOWLEDGMENTS

I would like to express my sincere gratitude to my advisor Professor Ronald Calhoun, for his devotion to this research. He has been the most instrumental person for my academic and research achievements. He provided the motivation, encouragement, guidance and advice which have prepared me for various challenges in life. Several hours of discussion on futuristic ideas for wind energy & lidar development, are burnt in my memory. Sincerely thank once again for treating me well and making my PhD a pleasurable experience. The ASU Environmental Remote Sensing Group would like to acknowledge the generous support of Intel Corporation, and especially the technical guidance of Dr. Annabelle Pratt during this research, the Army Research Office, sponsor awards W911NF0410146 and W911NF0710137 (Program Officer: Walter Bach), NSF grant 0522307, and Department of Energy (Award Number #DE-EE0005379). The author also recognizes the support of Naval Research Laboratory (Dr. James Doyle) in Monterey, CA, for performing multiple COAMPS simulations.

I would also like to thank, Dr. Huei-ping Huang, Dr. Patrick Phelan, Dr. Kangping Chen and Dr. Matthew Fraser for serving on my committee and providing valuable suggestions and feedback on my research. I also thank all my lab mates for laughing at my silly jokes and giving me good company. Finally, I would like to thank all my friends here in Tempe who have always given me company when most required.

TABLE OF CONTENTS

	Page
LIST OF TABLES	viii
LIST OF FIGURES	x
1. MOTIVATION AND BACKGROUND	1
1.1 Coherent Doppler lidar for wind energy	2
1.2 Mesoscale model evaluation with CDL.....	4
1.3 Wind farm control with scanning coherent Doppler lidar	7
2. DATA COLLECTION AND SIMULATION.....	11
2.1 CDL and tower measurements at Colorado study site.....	11
2.2 Offshore wind farm data at New Jersey site	13
2.3 Wind farm remote sensing campaign – Indiana	15
2.3.1 Galion lidar parameters.....	15
2.4 CDL data filtering.....	18
2.5 COAMPS simulation set-up	18
3 WIND FARM CHARACTERIZATION THEORY.....	21
3.1 Volume velocity processing.....	21
3.1.1 Interpolation of winds to hub height.....	28
3.2 Wind farm layout design.....	31
3.2.1 Global optimization	32
3.2.2 Wind farm layout wake interaction effects	33
4 LIDAR DATA VALIDATION	35

	Page
5 WIND FARM CHARACTERIZATION ANALYSIS	44
5.1 Terrain-following wind maps	44
5.2 Wind distributions.....	45
5.3 Diurnal variation of wind speed.....	49
5.4 Wind power production	50
5.5 Wind farm layout design.....	52
5.6 Wind farm wake analysis.....	54
5.7 Layered approach.....	55
6 MESOSCALE MODEL FORECAST COMPARISON.....	59
6.1 Tower, CDL and COAMPS inter-comparison.....	60
6.2 Spatial wind speed and power production deviations.....	66
6.3 Spatial wind distribution variations	68
6.4 Ramp events.....	70
6.5 Stability (α) variation across the domain	73
6.6 Diurnal variation effects on wind, direction and power estimates.....	74
6.7 Wind speed bias corrections	79
7. VALUE PROPOSITION OF CDL FOR WIND FARM DEVELOPMENT	85
7.1 Uncertainty on the future energy production	87
7.2 Sources of uncertainties	87
7.3 Net present value and return of investment	92
8. LIDAR ASSISTED WIND FARM CONTROL – FEASIBILITY STUDY	95
8.1 Wind turbine and farm control theory	95

	Page
8.1.1 Wind turbine control basics	95
8.1.2 Classical control designs.....	101
8.1.3 Modern control designs.....	102
8.1.4 Turbine modeling.....	104
8.1.5 Wind farm wake modeling.....	107
8.1.6 Wind speed evolution model	112
8.1.7 Lidar assisted wind farm control theory	117
8.1.8 Wind farm demand based control	120
8.2 LAWF control results	122
8.2.1 LAWF comparison to NREL FAST model	122
8.2.2 Remote dispatch based control	129
9. WIND FARM CONTROL OPTIMIZATION.....	134
9.1 Wind farm power optimization.....	134
9.2 Wind farm power optimization results	137
10. SUMMARY	145
JOURNAL ARTICLES FROM CURRENT RESEARCH	148
REFERENCES	150
APPENDIX A.....	161
APPENDIX B	166
APPENDIX C	173
APPENDIX D.....	176

LIST OF TABLES

Table	Page
1. Characteristics of the Doppler lidar system	13
2. Scan Pattern Definitions	17
3. Characteristics of the Galion Doppler lidar system	18
4: Fourier Series in azimuth angle, holding elevation fixed	23
5. Tower – Lidar wind speed statistics over the period of observation at Site 1	36
6. Tower – Lidar direction statistics over the period of observation at Site 1	36
7. Wind Speed RMS difference statistics for various time averaging periods at Site 1 ..	36
8. Percent change in wind power density estimates at various layers with respect to hub height at Site 2	57
9. Tower, Lidar and COAMPS wind speed statistics over the period of observation at 50 m (AGL) at Site 2	64
10. Tower, Lidar and COAMPS direction statistics over the period of observation at 50 m (AGL) at Site 2.....	64
11. Ramp Statistics comparison between Lidar and COAMPS at Site 2.....	72
12. Tower, Lidar and COAMPS (after bias correction) wind speed statistics over the period of observation at 50 m (AGL)	80
13. Uncertainties in wind farm resource assessment	90
14. P-Values for various uncertainty estimates from lidar and tower (blah)	91
15. Return of Investment calculations for various resource assessment configurations for a 250MW wind farm.....	94
16: IEC Standard Parameters	116

Table	Page
17. Average power increase in downwind turbines for various upwind reference powers and input wind speed of 11 ms^{-1}	142
18. Average thrust coefficient reduction in downwind turbines for various upwind reference powers and input wind speed of 11 ms^{-1}	142
19. 12 Elevation angles (deg) for stack of PPI's from each lidar's	168
20. Azimuth Angles (deg) for stack of PPI's from each lidar's.....	168
21. NREL 5MW - Mass and Inertia Properties.....	174
22. NREL 5MW - Hub and Nacelle Properties	174
23. NREL 5MW - Drive train and generator Characteristics	174
24. NREL 5MW - Control Characteristics	175
25. NREL 5MW - Tower Properties.....	175

LIST OF FIGURES

Figure	Page
1. Wind Power variability over 24 hours in California (by California Independent System Operator [CAISO]) on March 19 th , 2013. A ramping event is also shown, 1,000 MW increase in power over a period of one hour.	8
2. The framework of multiple time-scale coordinated power control system (Wu et al. 2012).	9
3: Shows the terrain of the site 2 (oriented facing north). Position of the lidar (center) and tower (north of lidar) shown. The lidar scan radius is shown (dotted red line) and 1, 2 and 3 (cross marks) are locations where different wind speed distributions were observed. Discussed in Sections below.	12
4. Offshore Terrain and lidar scan extent. Five turbines (dots) are located in the blind zone of lidar measurement, reason for hard targets in data sets. Lidar (x) location is also shown. Color bar indicates radial velocity magnitude in m s^{-1}	14
5. Remote sensing instrument setup in the Indiana wind farm.	16
6. Percentage of scanning performed for the period of campaign (Barthelmie et al. 2012).	17
7. Volume velocity processing algorithm analysis volume (Xin et al. 1997).	28
8. Percentage of power law used to obtain an 80 m terrain following surface from lidar measurements. The color bar represents the percentage of power law used over the entire period of study. A total of 3,459 observations were included for this analysis.	30

Figure	Page
9. Terrain cross-section from lidar location, through the tower, till the end of scan radius is shown above. Lidar (x) and tower location are shown. Scans at various elevation angles are displayed. The power law ‘dip’ height used to estimate wind speed at terrain-following surface (80 m hub height) is approximately 20 m.	31
10. (a) Comparison between one minute averaged tower and ten minute interpolated lidar wind speed at 50m. (b) Comparison between one minute averaged tower and ten minute interpolated lidar direction at 50 m. A total of 3,459 ten minute periods are chosen for both figures. Gaps in the series correspond to bad signal-to-noise ratio at those time periods, hence was neglected.	38
11. (a) Scatter plot of tower versus lidar wind speed at 50 m. Standard regression analyses produced the best fit line ($y = 0.95x + 0.4$), showing 94 % correlation (solid line) and the linear fit through origin is also shown (dotted line), (b) Scatter plot of tower versus lidar wind direction at 50 m. Data analyzed between directions 60-300 deg.	38
12. Scatter plot of tower versus lidar wind speed at orthogonal directions to mean wind direction ($170^\circ \pm 45^\circ$) at 50 m. A linear regression fit ($y = 0.9x + 0.56$) showing 89 % correlation (solid line) and the linear fit through origin is also shown (dotted line).	39

Figure	Page
13. (a) U –component scatter plot of tower versus lidar at 50 m. A linear regression fit ($y=0.89x -0.27$) showing 96% correlation (solid line) and the linear fit through origin is also shown (dotted line). (b) V –component scatter plot of tower versus lidar at 50 m. A linear regression fit ($y=0.81x -0.2$) showing 88% correlation (solid line) and the linear fit through origin is also shown (dotted line).....	39
14. (a) Tower wind rose for the period of observation at 50 m (b) Lidar wind rose for the period of observation at 50 m. Wind speeds (6 bins of 4 ms^{-1}) were divided into twelve directional sectors. Percentage circles (10, 20, 30 and 40%) are also shown.	40
15: Off-mean wind directions at tower locations. Lidar measurements perpendicular to the tower direction were collected for correlations.....	40
16. Tower and lidar wind speed comparison at the Indiana wind farm from PPI scans..	41
17. Tower and lidar direction comparison at the Indiana wind farm from PPI scans.....	42
18. Wind speed comparison between tower and lidar (VVP algorithm) at a wind farm in Indiana. The lidar measurements were picked one (1) km ahead of the tower measurements. Correlation of wind speed is 84%.	42
19. Direction comparison between tower and lidar (VVP algorithm) at a wind farm in Indiana. The lidar measurements were picked one (1) km ahead of the tower measurements. The correlation of wind direction is 94%.....	43

20. Lidar terrain-following averaged wind speed measurement at 80 m hub height. The colour bar represents wind speed from 5 to 12 ms^{-1} . The lidar is at the centre and the tower is located 3.42 km north-west of the lidar. The radius of the scan is 5.75 km. 45
21. (a) Distribution of wind speed comparison between tower and lidar measurements at 50 m (from all directions). (b) Wind speed distribution between the tower and lidar in the radial direction at 50 m. Wind speed data selected from directions $170 \pm 45^\circ$ and $350 \pm 45^\circ$ were chosen for this distribution (mean wind direction is 170°). (c) Wind speed distribution between the tower and the lidar in the transverse direction at 50 m. Wind speed data selected from directions $80 \pm 45^\circ$ and $260 \pm 45^\circ$ were chosen for the distribution (mean wind direction is 170°). The distribution is less well defined due to reduced amount of data perpendicular to the mean wind direction. 47
22. Distribution of wind speed from lidar at three vertical levels within the turbine rotor region from lidar measurements, showing bimodal distribution (i.e., one peak near $5\text{--}7 \text{ ms}^{-1}$ and another at 10 ms^{-1}) at 50 m, 80 m and 110 m heights (from all directions) 48
23. Different distribution of wind speed observed at various locations from lidar measurements, 50 m above ground level (from all directions). Locations 1, 2 and 3 are shown in Figure 1. 49

Figure	Page
24. Monthly two-hour averaged vertical profiles of wind speed for 24-hours (data collected 3km north of the site) showing strong diurnal variations from lidar measurements. The legend displays local times.	50
25. Lidar terrain-following machine power production at 80 m hub height. The colour bar represents the power in kW.	52
26. Locations of wind turbines (75), based on simple algorithm, overlaid over averaged wind map. The white circular dots represent locations of wind turbines based on the algorithm. The color bar shows wind speed in ms^{-1} at 80 m hub height.	53
27. Optimized layout (25 turbines) based on Genetic Algorithms overlaid over power production map. The + symbols represent optimized turbine locations. A minimum separation of 7D was used in this analysis. Wind turbine wake interaction effects (Kusiak et al. 2010) were also included for optimal energy and cost output.....	54
28. Cumulative wind farm wake deficit measured by lidar at site 2. Park model with turbine wake interaction effects for several decay constants is also shown. A decay constant of 0.09, seems to approximate the wind speeds reasonably well.	55
29. Terrain-following wind power density estimates at various heights of the rotor swept area. The “combined” wind power density estimated from all the three layers is also shown. Where X (km) and Y (km) is the distance from lidar in the respective directions.....	58
30. Terrain of the site with lidar scan overlaid. Four locations (x) shown were used to compare distributions between lidar and COAMPS. Tower is located at location 4. Color bar represents terrain height.....	59

Figure	Page
31. COAMPS estimated wind speed for the period of observation at Site 2.....	60
32. COAMPS rectangular grid (x) and Lidar Polar grid (o) overlaid over terrain. The sub-figure shows the points averaged from lidar estimate for appropriate comparison with COAMPS data. Each dotted box shown in the sub-figure represents COAMPS grid cell of 333 m. Four locations (square boxes with white background) on the terrain were chosen for further analysis. The color bar represents the terrain height in meters. <i>X</i> and <i>Y</i> represent distances from lidar location.	62
33. A) Lidar versus COAMPS direction comparison at 50 m for the period of observation. The gaps in lidar series show time periods when measurement with very low signal-to-noise ratio was observed. B) Wind speed comparison between COAMPS, lidar and tower simulation at 50 m. The gaps in lidar series show time periods when measurement with very low signal-to-noise ratio was observed.....	63
34. (a) COAMPS and (b) Lidar wind rose at 50 m. The color bar represents wind speeds in 4 ms ⁻¹ intervals and percentage of wind speed in each direction sector is provided on the dotted circles.	65

Figure	Page
35. A) Wind speed scatter plot Lidar and COAMPS wind speed (30 minutes). Wind speed correlation of $\sim 40\%$ ($y = 0.74x + 2$) is observed between lidar measurements and COAMPS forecasts. Similar correlations are observed between tower and COAMPS forecasts. A total of 1296 values were used in the above plot. B) Direction scatter plot Lidar and COAMPS wind speed (30 minutes). Direction correlation of $\sim 22\%$ ($y = 0.54x + 83$) is observed between lidar measurements and COAMPS forecasts. Similar correlations are observed between tower and COAMPS forecasts. Data analyzed between 60 and 300 degrees. A total of 1,270 data points were used in this analysis.	65
36. Spatial map of mean wind speed (ms^{-1}) difference between lidar and COAMPS simulation for the period of observation (Lidar minus COAMPS). The contour lines show terrain height.....	67
37. Normalized spatial map of mean machine power difference between lidar and COAMPS simulation for the period of observation (Lidar - COAMPS). The contour lines represent terrain height. (Normalized by turbine rated power)	68
38. Wind speed distribution comparison between lidar and COAMPS simulation at all four locations shown in Figure 30. A) location 1, b) location 2, c) location 3 and d) location 4 on Figure 30.	70
39. Cumulative wind farm power (MW) comparison between lidar measured and COAMPS forecasts. The dotted rectangular boxes show various ramp events observed by lidar.....	72

Figure	Page
40. A) One hour averaged stability parameter (power law exponent $-\alpha$) calculated by lidar on June 17, 2007. B) One hour averaged stability parameter (α) calculated based on COAMPS simulations on June 17, 2007.	74
41: A) Hourly averaged diurnal variation of wind speed difference between tower, lidar and COAMPS at 50 m (Lidar – COAMPS). B) Standard deviations of wind speed difference between tower, lidar and COAMPS at 50 m.	75
42: A) Hourly averaged diurnal variation of direction difference between tower, lidar and COAMPS at 50 m. B) Standard deviations of direction difference between tower, lidar and COAMPS at 50 m.	76
43: A) Hourly averaged mean wind speed difference between lidar and COAMPS simulation at different locations (shown in Figure 30) for the period of observation at 50 m (Lidar – COAMPS), B) Hourly standard deviation of wind speed difference for the period of observation at 50 m.	78
44: A) Hourly diurnal variation of average normalized machine power (kW) difference between lidar and COAMPS at 90 m (Lidar – COAMPS), at multiple locations shown in Figure 30. B) Hourly averaged standard deviations of normalized power (kW) difference between lidar and COAMPS for the period of observation at 90 m (normalized by wind turbine rated power).	78
45. Spatial monthly averaged wind speed difference between Lidar and COAMPS bias corrected estimates (Lidar-COMAPS). The contour lines represent terrain height and color bar shows wind speed difference in ms^{-1}	81

Figure	Page
46. Spatial monthly averaged normalized power difference between Lidar and COAMPS Bias corrected estimates (Lidar-COMAPS). The contour lines represent terrain height and color bar shows normalized power difference (normalized by wind turbine rated power).....	82
47. Distribution of 30 minute wind speed difference between Lidar and COAMPS (Lidar – COAMPS) with (no fill) and without bias (filled bars) correction at tower location. Normal distributions of both the distributions are also shown.	83
48. Spatial wind speed RMS difference between Lidar and COAMPS before Bias corrections.....	83
49. Spatial wind speed RMS difference between Lidar and COAMPS Bias corrected estimates.....	84
50: Wind Farm costs breakdown	86
51. Normal Distribution with P50 at 144 GWh/year and a Std. Deviation of 14% in AEP.	87
52. Normal distribution based on different uncertainty estimates from instruments.....	91
53. NREL 5MW Turbine parameters (Jonkman et al. 2009).....	97
54. $C_p (\lambda, \beta)$ versus tip-speed ratio and pitch for NREL 5MW wind turbine.	99
55. NREL 5MW turbine performance properties	100
56: Wind turbine nacelle schematic. All the turbine components shown in the figure are modeled (Picture Courtesy of NREL).....	104
57. C_T versus tip-speed ratio and pitch for NREL 5MW wind turbine.	105

Figure	Page
58. Illustration of regimes of the Frandsen's (2006) model. The wind from south is parallel to the direction of the rows.	108
59. Flow between two wind turbines in a row of wind turbines (Frandsen et al. 2006).	110
60. Frandsen's Model deficit comparison to data extracted from Frandsen et al. 2006	110
61. Wake diameter for 3 turbines downwind as estimated based on Equation 31. For various downwind spacing or Rotor Diameter (RD) and $C_T = 0.8$	111
62: Sample spatial wind field from the Mann Spectral model at hub height wind speed of 10m/s, TI of 12% and IEC standard parameters. The color bar represents wind speed in ms^{-1} and X, Y represents the horizontal & lateral displacement distance.	117
63. Coherent Doppler lidar informed wind farm control structure.	119
64: Ideal power tracking β and λ curves. The black line shows optimal pitch angles for various λ and blue dotted line represents optimal λ for various pitch angles.	121
65. LAWF control comparison to NREL FAST for an average turbulent wind speed of 18m/s, as simulated in TurbSim. The figure above shows a) winds, b) rotor speed, c) pitch angle, d) generator speed, and e) generator torque.	125
66. Power time series comparison between LAWF and FAST for turbulent wind speed at 18ms^{-1}	126
67. Pitch angle variation for various turbine power set points for a turbulent wind speed at 18ms^{-1} . The rated wind speed of NREL 5MW turbine is 12ms^{-1}	126
68. FAST comparison to control at 5ms^{-1} average winds (using TurbSim). The winds, power (P), generator speed (ω_{gen}) and rotor speed (ω_{rot}) are shown above.	127

Figure	Page
69. Forces computed using FAST and LAWF control for an average wind speed of 5ms^{-1} (shown in Figure 68 above). The generator torque (τ_{gen}) and thrust force (F_x) are compared.....	127
70. Tower deflection as estimated by FAST and LAWF.....	128
71. Yaw control results for an upwind turbine.	129
72. Wind Farm Layout Design (10 NREL 5MW wind turbines) used for analysis	130
73. Average scanning Lidar winds and direction upwind of the wind farm.....	131
74. Demand based control. Wind farm power demand curve is shown in red, the power available is shown in dashed blue line, and the power produced is shown as the black line with square boxes.	131
75. Various options for Demand based control. The maximum available power (“greedy control”) is shown in black line (34 MW), while direction based control and equal power distribution options are shown in red and blue respectively.....	133
76. C_p as a function of reference power (P_{ref}) and wind speed (V). The streaks represent the non-linear part of the power curve.	136
77. C_T as a function of reference power (P_{ref}) and wind speed (V). The streaks represent the non-linear part of the power curve.	136
78. Sample array of 10 5MW wind turbines.....	137
79. The increase in velocity, power and reduction of thrust coefficients at downwind turbines compared to “greedy” control, due to reduced power reference at the turbine 1 by 0.5 MW.....	139

80. A) Velocity at each turbine for a linear array of 10 5MW wind turbines at an input wind speed of 11 ms^{-1} . The blue curve represents the optimized power after reducing the first turbine power set-point by 0.5MW and matching other turbines power reference set points to previous maximum power control (“greedy control”). B) Power output for a linear array of turbines at input wind speed of 11 ms^{-1} . C) Coefficient of thrust (C_t) for a linear array of turbines at input wind speed of 11 ms^{-1}	140
81. Power effect of reducing power reference of upwind turbines on downwind turbines at input wind speed of 11 ms^{-1} . Maximum power control (“greedy”) is also shown.	141
82. Thrust effect of reducing power reference of upwind turbines on downwind turbines at input wind speed of 11 ms^{-1}	142
83. Wind farm power output for the winds and direction shown in Figure 73. Lidar wake induced wind farm power 1 km ahead of the wind farm is also shown. The optimized power algorithm was performed, when multiple downwind turbines are affected by upwind turbine performance.	144
84. Coherent Doppler lidar basic operation principle.	164
85. Potential Lidar locations for Dual-Doppler deployment covering a 6 km x 4 km potential wind farm domain. Lidar 1 is located at the crop-duster site and Lidar 2 is located near SRF site. [Assuming a max. lidar range of 10K with 95 m range-gate spacing]	168
86. Terrain of the potential wind farm shown in Figure 1.	169

Figure	Page
87. No. of radial velocity “hits” from both lidars in each 300 m x 300 m x 20 m grid cell box within 4.5 minutes over the wind farm domain shown in Figure 1 at 90 m (hub-height). [This result is for a terrain-following layer centered on 90 m AGL.] The number of samples in each grid might reduce after accounting for terrain-blockages or data filtering.....	170
88. Ratio of “hits” from each lidar covering the wind farm region at 90 m AGL	171
89. Maximal temporal difference (Δt) between hits at each grid cell in a 90 m AGL layer (+/- 10 m in vertical). Colors represent Δt in minutes. Data holes represent data only from one of the lidar’s would be collected at that grid cell.	172

1. MOTIVATION AND BACKGROUND

Wind energy is one of the fastest growing and currently practical forms of renewable energy (AWEA, 2011). In recent years, wind power has exhibited the highest growth rates among all renewable energy sources. It can be considered as the most promising option for replacing a significant part of the electricity produced by conventional sources. Reliable measurement of wind fields is an important foundation of optimal design and operation of wind farms. Since past two decades, the average turbine hub height has increased by 43%, while the average rotor diameter has increased by 76% (Wind Energy Technology Market Report, 2010). Further scaling, especially in rotor diameter, is expected in near future. Current industry standards for wind and turbulence measurements for wind energy applications are to utilize *in-situ* wind instruments, most typically, cup & vane anemometers on tall meteorological masts (Amar et al. 2008, Belu et al. 2009). For the latest large turbine models, conventional mast wind speed measurements are insufficient, and installations of high mast wind speed measurements are problematic, due to cost and safety considerations. There is a growing awareness of the inadequacy of current methods to measure the spatial variability of the winds, both vertically and horizontally, for wind assessment (Sempreviva et al. 2008, Hannon et al. 2008, Mikkelsen et al. 2008). Due to the global growth of wind energy, short-range lidar profilers, sodars are proliferating and are increasingly being used to measure wind profiles (Smith et al. 2006, Barthelmie et al. 2006, Bingol et al. 2010). A larger body of open literature is required to more fully understand the character of these and other remote sensing measurements for wind energy applications. Three-Dimensional (3D) coherent Doppler lidars have been extensively used in meteorological studies for the past

few decades (Gal-chen et al. 1992, Frehlich et al. 1998, Newsom et al. 2005, Retellack et al. 2010, Krishnamurthy et al. 2010, Krishnamurthy et al. 2011). Modern 3D scanning coherent Doppler lidars are well suited for characterizing wind farm airsheds, and may eventually form a new basis for real-time adaptive control of wind turbines (Laks et al. 2009). Lidars can measure the velocity deficit downstream of an individual wind turbine (Kasler et al. 2010), as well as the accumulated wakes from an array of turbines. Typical ranges of the current generation of commercially available coherent Doppler lidar (such as that used in this study, i.e., *WindTracer*, from *Lockheed Martin Coherent Technologies, Inc.*) are 10 ~ 20 km, depending on the atmospheric conditions.

Previous wind energy literature has already emphasized the importance of obtaining and utilizing more complete information from the wind profile. For example, Wagner et al. 2009, suggest more accurate power curves can be obtained by replacing the single wind speed at hub-height with *effective wind speeds* which account for the vertical variability of the wind profile over the rotor plane. In addition, identification of complex flow phenomena such as nocturnal jets (Banta et al. 2002) or periodic shear instabilities (Banta et al. 2008) are critical for normal operation of wind turbines. These flow events can be difficult to adequately capture with tower measurements alone.

1.1 Coherent Doppler lidar for wind energy

In order to understand how wind profiles are obtained by lidar, it is useful to review the difference between the fundamental measured product of the Doppler lidar and secondary retrieved products. Doppler lidars fundamentally measure a Doppler shift along their laser beam propagation path. Therefore, motion of the air orthogonal to the propagation path of the laser beam produces no Doppler shift. Consequently, the basic

Doppler lidar output is the *radial velocity*, or the dot product of the velocity vector with the beam direction unit vector. Interpretation and processing of the radial velocity fields can be complex, requiring the resolution of indeterminacy in the basic data through supplementary assumptions or information. Various wind retrieval techniques have been developed to estimate 2D and 3D vector fields from Doppler lidar data (Newsom et al. 2005, Chan et al. 2007, Xu et al. 2006, Lin et al. 2008, Xia et al. 2008, Kongara et al. 2012, Choukulkar et al. 2011). Algorithms range from computationally intensive 4DVAR (four-dimensional variational data assimilation) techniques to simpler and faster methods based on volume velocity processing (VVP) (Doviak and Zrnic et al. 1993) and 2DVAR (Chan et al. 2007). Current techniques are generally suitable for many applications such as pollution transport studies and vertical profiling for wind farms assuming that the averaged nature of the products and underlying assumptions are understood. Dual Doppler lidar techniques also provide accurate estimates of the 2D wind field (Calhoun et al. 2006, Newsom et al. 2008, Dreschel et al. 2009, Hill et al. 2010).

The flexibility of lidar to perform conical (Plan Position Indicator [PPI]), vertical-slice (Range Height Indicator [RHI]) or fixed-beam measurements, allows investigation of a variety of boundary layer characteristics. The wind-field structure from different points of view can be visualized, for example, mean wind and turbulent profiles, time series, or as images of individual scans – to reveal flow features at hub height and above the range of tower measurements.

Evidence will be presented below that *3D scanning coherent Doppler lidar is also capable of producing wind speed distribution of the wind field as a function of space.*

This can be used to obtain a spatial power density distribution over the entire region.

This research presents the results of a Doppler lidar deployment for a proposed wind energy development. Few of the objectives of this research are:

- i. To characterize the spatial wind field at the hub height over the entire region,
- ii. To calculate (spatially varying) wind speed distribution, and spatial power density distribution over the region of interest,
- iii. To estimate power density using multiple vertical layers within the rotor swept area,
- iv. To demonstrate a simple algorithm for wind farm layout design based on spatial power density distribution and distance limitation,
- v. Since CDLs can view the incoming winds at a distance of *5-15 km* ahead of the turbine, they can be used for wind farm control. An initial framework is shown below.

1.2 Mesoscale model evaluation with CDL

CDLs and modern mesoscale models are capable of measuring/predicting wind speed and direction across the entire wind farm domain. Mesoscale models such as Weather Resource Forecast (WRF) and Coupled Ocean/Atmosphere Mesoscale Prediction System (COAMPS) etc., are generally used to estimate wind energy potential (Archer and Jacobson 2005, Jiang et al. 2008, Dvorak et al. 2010). The skill of mesoscale forecast models has advanced dramatically in the past few years, but variables relevant to wind energy applications, such as near-surface wind speed, vertical wind shear, and low-level turbulence are a source of significant error (Barthelmie et al. 1996,

Darby et al. 2002, Fast et al. 2004, Jimenez et al. 2007, Shaw et al. 2008, Krishnamurthy et al. 2013). Most of the wind turbines reside in the lowest portion of the planetary boundary layer, from the surface to about 200 m above the surface. Incomplete understanding of the energy exchange between the surface and the atmosphere is still a topic of increasing interest (Shaw et al. 2008). In order to understand the shortcomings of model forecasts, spatial and temporal scale comparison with observation is critical. Most of the current comparison between simulations and observations are based on tower or sodar measurements at a single location. As per the author's knowledge, no prior spatial comparison between forecast and observations is provided in the literature.

In this part of study, we compare wind speed, direction and power estimates from COAMPS forecast model, 3D coherent Doppler lidar and tower measurements for a wind energy development. The COAMPS model is developed at the US Naval Research Laboratory (Hodur et al. 1997, Smith et al. 2010). Several studies have been conducted, using COAMPS forecast models, to analyze the marine boundary layer (Pullen 2006, Chin et al. 2010, Allard et al. 2010). Very few studies have been performed for wind energy applications. Chin et al. 2010 found decent comparisons with low-level wind speed observations with COAMPS and Weather Research Forecast (WRF). Previous studies have found less COAMPS forecast errors with higher grid resolution when compared to observations (Chin et al. 2010). Although after a certain grid resolution threshold the reduction in errors is not significant.

The objectives of this research were to compare simulation and lidar:

- i. Spatial wind field and power differences at hub height over the entire region.
- ii. Spatially varying wind speed distribution across the region of interest.

- iii. Effects of diurnal variation on wind speed, direction and power production at hub height.
- iv. Wind speed ramp events and their effect on instantaneous power production at hub height.
- v. Stability variations (power law exponent - α) across the domain.

Bias corrections can be applied to numerical models to account for the wind speed deficit estimated from measurements. Studies have accounted for monthly bias in wind speed forecasts, based on tower measurements at a single location to improve NWP model estimates (Shimada et al. 2011). Advanced bias correction approaches, such as Analog-Based Kalman Filter bias correction algorithms are also being researched (Parks et al. 2011). Accounting for large positive bias would certainly improve the accuracy of mesoscale models at locations closer to the tower. Since most of the recent wind farms span a region greater than 20 km², the bias observed by mesoscale models vary at different locations due to several reasons (for ex. terrain, urbanization, soil composition etc.). Therefore, bias corrections performed at a single location can reduce the accuracy at different domains of the wind farm. The spatial difference observed between COAMPS after a mean bias correction based on tower measurements located at the site and lidar are compared. Hourly averaged variation of wind speed and directions at several locations are also compared, to evaluate time periods where the models perform better and time periods where improvements are required. Hourly power outputs are also estimated and compared to lidar estimates.

1.3 Wind farm control with scanning coherent Doppler lidar

One of the key aspects for attaining wind power output to maintain Renewable Portfolio Standards (RPS) set by many states in United States, is to utilize existing wind farms in a more efficient manner through improved control algorithms and incorporating advanced remote sensing technologies. Most of the existing research on the control of wind turbines focuses on individual turbine optimization (Pao et al. 2011). The control of an array of turbines in a wind farm is more challenging than controlling a single turbine because of the interactions amongst the turbines which render most of these single turbine control algorithms highly inefficient for optimizing power capture in wind farms (Steinbuch et al. 1988, Johnson et al. 2009, Barthelmie et al. 2010). The potential for improving performance, both in terms of increasing power capture as well as mitigating loads across the wind farm, has led to several new research efforts in coordinating the control of arrays of wind turbines (Rawn et al. 2006, Rodriguez-Amendo et al. 2008, Sorensen et al. 2008, Soleimanzadeh et al. 2011, Spudic et al. 2010, Kristalny et al. 2011).

The integration of large scale wind power generation will greatly affect operation of power system and power quality. The supervisory control system at a power utility station is set to coordinate various power generations, including wind, hydro and thermal power. And the wind power plant system is used to predict the near future wind power output (currently based on forecasting) and adjust the generator's output according to the commands sent from the central control operator. Currently, most of the wind turbines in a wind farm are operated at maximum capacity and the additional power is either supplied to out-of-state grid (for free of cost and results in transmission losses) or

discarded. Since wind power is highly unpredictable compared to other renewable energy power sources (shown in Figure 1 below), knowledge of the winds a few minutes ahead of the wind farm would be valuable to the wind farm operator to maximize the wind farm performance and reduce unnecessary loads on wind turbines. Current forecast models are not accurate in predicting hourly or minute-by-minute variations in the wind field and are not useful for control/operation of wind farms. 3D scanning lidars can provide winds and directions ahead of the wind farm, which can be used for scheduling the wind farm load/demand minutes before the winds approach the wind farm. The time-scale of operation, for coordinated power control system by a utility scale operator is shown in Figure 2 below. 3D scanning Doppler lidar can assist the controller in balancing generators, by optimizing wind farm performance and scheduling generators 10-15 minutes ahead, to meet the grid demand.

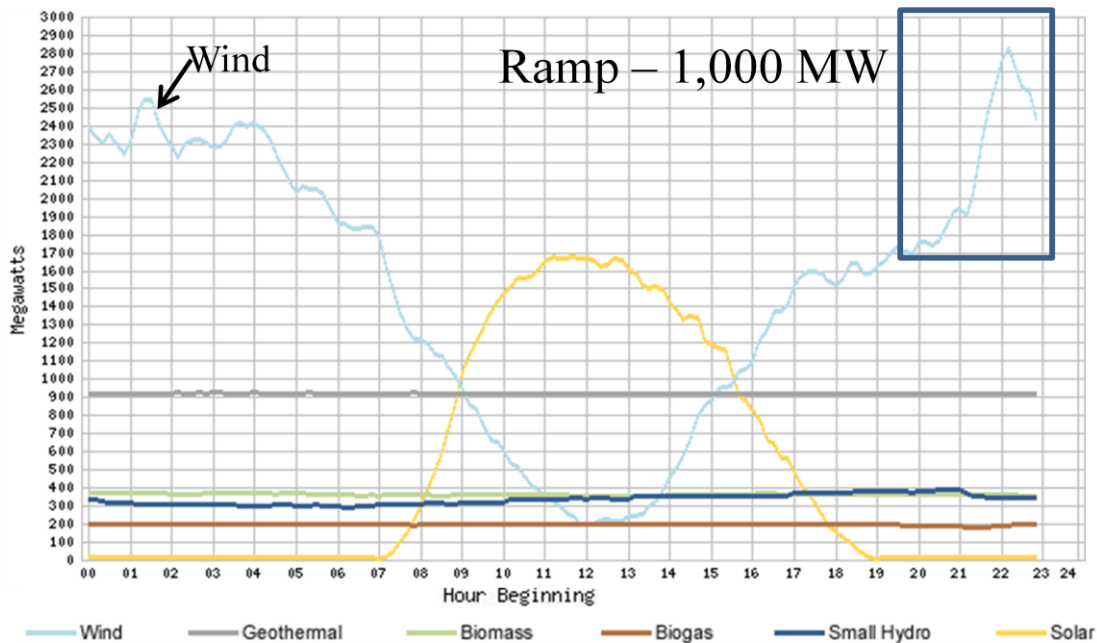


Figure 1. Wind Power variability over 24 hours in California (by California Independent System Operator [CAISO]) on March 19th, 2013. A ramping event is also shown, 1,000 MW increase in power over a period of one hour.

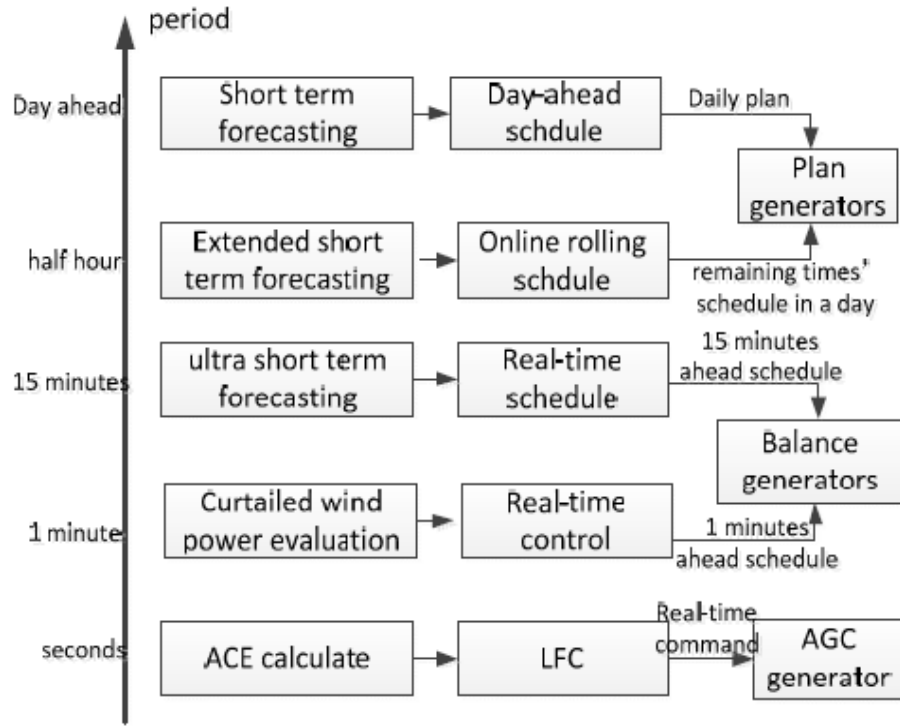


Figure 2. The framework of multiple time-scale coordinated power control system (Wu et al. 2012).

The stochastic nature of wind resources, the high initial capital cost, and the increasing structural flexibility of modern turbines motivate the adoption of advanced instrumentation and measurement technologies. Scanning coherent Doppler lidar (CDL) systems are able to measure real-time wind conditions 5- 15 kilometers in front of wind farm and are therefore suited to providing preview information of flow disturbances before they impact the wind farm. These types of measurements make it possible to employ feed-forward techniques for the wind farm using a preview of actual wind speeds, instead of employing wind estimates obtained from measurements at the turbine nacelle which do not provide any preview. Limited preview information by using a short-range lidar installed on the nacelle or hub of the wind turbine (Laks et al. 2011, Schlipf et al.

2012a, Schlipf et al. 2012b, Mikkelsen et al. 2012, Wang et al. 2012, Scholbrock et al. 2013), are mainly used for minimizing individual turbine loads. Scanning CDLs could be potentially used to test first-order effects of wind farm responses to CDL-informed control algorithms in realistic atmospheric flows, which could improve the farm efficiency and maintain the required grid demand.

This thesis is outlined as follows. Section 2 describes the lidar and simulation experimental setup at the wind farm development sites used for this study. Location of the lidar is confidential for experimental site 1, since it's an ongoing wind energy development for a commercial enterprise. Section 3 outlines the theory behind estimating winds from coherent Doppler lidar and obtaining a wind farm layout. Section 4 provides thorough data validation of lidar results with tower measurements. Detailed explanation of the results is provided in Section 5 and 6. Section 7 describes the value proposition of scanning Doppler lidar for wind energy. Section 8 describes the theory and results behind wind farm & wind turbine control. Finally, a summary and future work is provided in Section 9.

2. DATA COLLECTION AND SIMULATION

2.1 CDL and tower measurements at Colorado study site

The Doppler lidar used in this study was a 2- μm eye safe *WindTracer* lidar manufactured by *Lockheed Martin Coherent Technologies, Inc.* (LMCT) (Henderson et al. 1991, 1992). Further attributes and capabilities of coherent Doppler lidar are provided in Appendix A. The lidar was located at the center of the region of interest. The site provided excellent 360 degree line of sight and clear views to all locations within the wind farm (Figure 3). The initial range observed was from 8 to 12 km depending on averaging and atmospheric conditions. The lidar has an initial blind zone of 436 m (*i.e.* the backscatter from this zone is not detectable by lidar), over which no data is collected (shown as grey region surrounding the lidar). The location of the study is confidential as it's a part of an ongoing wind energy assessment study for a commercial enterprise. The study was conducted during the months of June and July in 2007.

A coherent Doppler lidar estimates the radial velocity of the collection of aerosol particles illuminated by the lidar pulse as it travels through the atmosphere. The performance of Doppler lidars depends on the parameters, atmospheric conditions, and the velocity estimation algorithm (Frehlich et al. 1998, Hill et al. 2010). Table 1 provides the coherent Doppler lidar parameters utilized during this study. The lidar utilizes a Gaussian pulse with a width of 105 m (full width at half maximum) (Frehlich et al. 1998). For this experiment, the range-gate length (distance between two radial measurements) was set at 105 m, and an azimuthal scanning rate of $9.55^\circ \text{ s}^{-1}$ was used. As this type of lidar has a pulse repetition frequency (PRF) of 500 Hz, 100 lidar pulses averaging produced "beams" of data every 0.2 s.

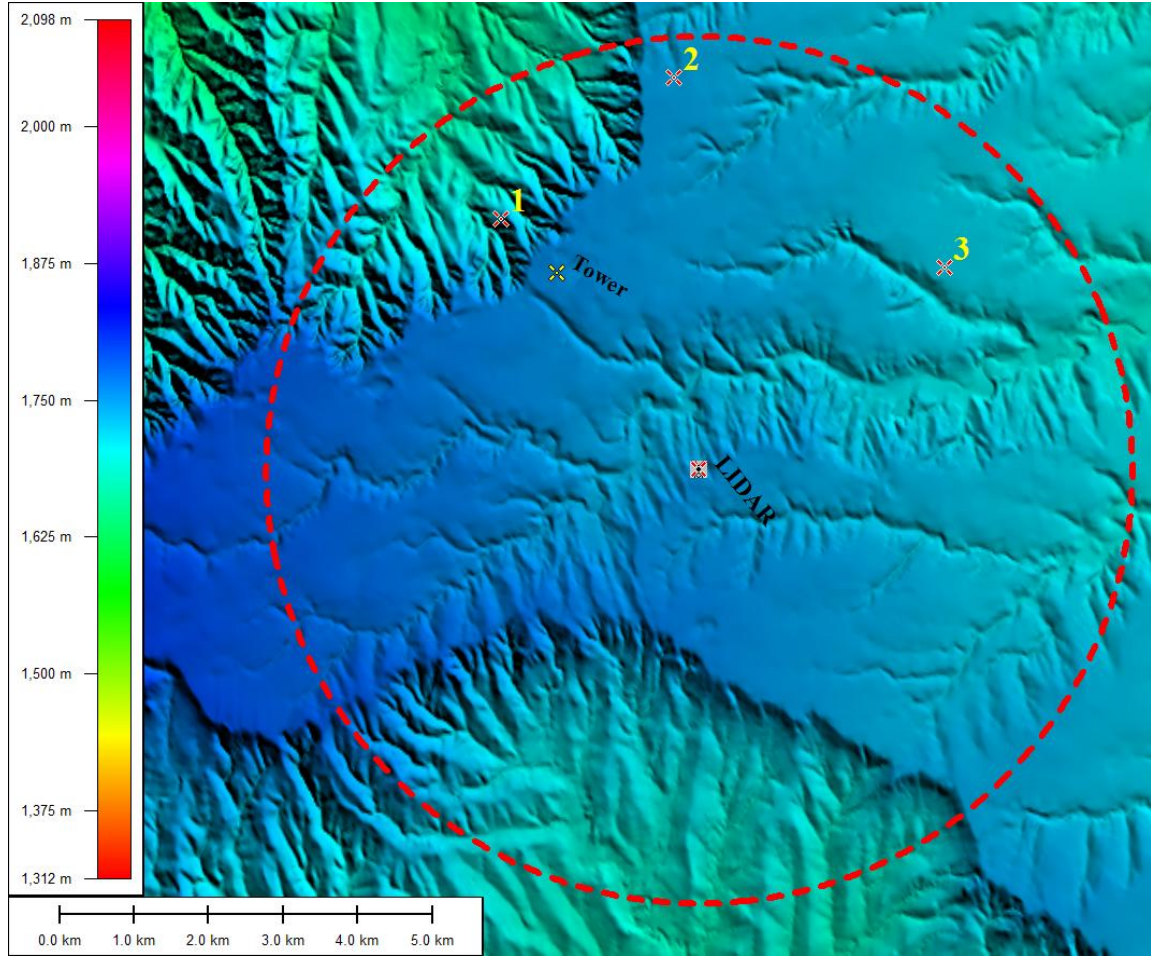


Figure 3: Shows the terrain of the site 2 (oriented facing north). Position of the lidar (center) and tower (north of lidar) shown. The lidar scan radius is shown (dotted red line) and 1, 2 and 3 (cross marks) are locations where different wind speed distributions were observed. Discussed in Sections below.

Therefore, the azimuthal spacing between beam products was $\Delta\phi = 1.96^\circ$. The horizontal resolution between two successive measurements is approximately 17 m, at the first range gate, to ~ 205 m, at farthest range-gate (due to diverging beams). The vertical resolution between successive elevation angles was approximately 18 m (at the farthest range-gate). The accuracy for this type of lidar was expected to be in the range $0.1 - 0.5 \text{ ms}^{-1}$ for the radial velocity product beams (Frehlich et al. 1998). Due to the complex terrain, a set of different simple scans were assembled so that data could be obtained on a

terrain-following surface at hub height. The data was acquired for a period of one month. A stack of 360° PPI's with varying elevation angles (0.05°, 0.24°, 0.43°, 0.62°, 0.81°, 1.0°, 1.19°, 1.45° etc.) were performed to measure data for the majority of the domain. The elevation angles were chosen to acquire radial wind velocity data above and below the hub height across the site. Data from 16 PPI scans (*i.e.*, one stack) were used to produce the terrain-following wind speed maps. Each stack required approximately 10 minutes to complete. Cup anemometers and vanes were placed on a tower within the region of interest (north-west of lidar location, ~ 325°) to evaluate the accuracy of wind speed retrievals.

Table1. Characteristics of the Doppler lidar system

Transmitter	Nd-Yag laser
Operating Wavelength	1.6/2μm
Energy per pulse	2mJ
Pulse repetition frequency	750/500 Hz
Range resolution	48 - 105 m
Min range	436 m
Max range	10,917 m

2.2 Offshore wind farm data at New Jersey site

The Doppler lidar used in this study was a 1.6-μm eye safe *WindTracer* lidar manufactured by *Lockheed Martin Coherent Technologies, Inc.* (LMCT). Figure 4 shows the terrain of the site and the location of lidar. Lidar was placed within an operational

wind farm near Atlantic City, USA. Since lidar was located within a small wind farm (in between 5 wind turbines as shown in Figure 4), lidar beam hard targets restricted the range of measurements in a few directional sectors. Since lidar is located near the shore of Atlantic City, range of $\sim 10\text{-}15\text{ km}$ is observed for most of the time period due to clear line of sight. A stack of 360° PPI's with varying elevation angles were performed to measure data for the majority of the domain. The elevation angles were chosen to acquire radial wind velocity data at various heights within the turbine rotor across the site. Approximately two months of data was obtained, between October 5, 2010 to December 1, 2010, with a few days for maintenance and repair of lidar.

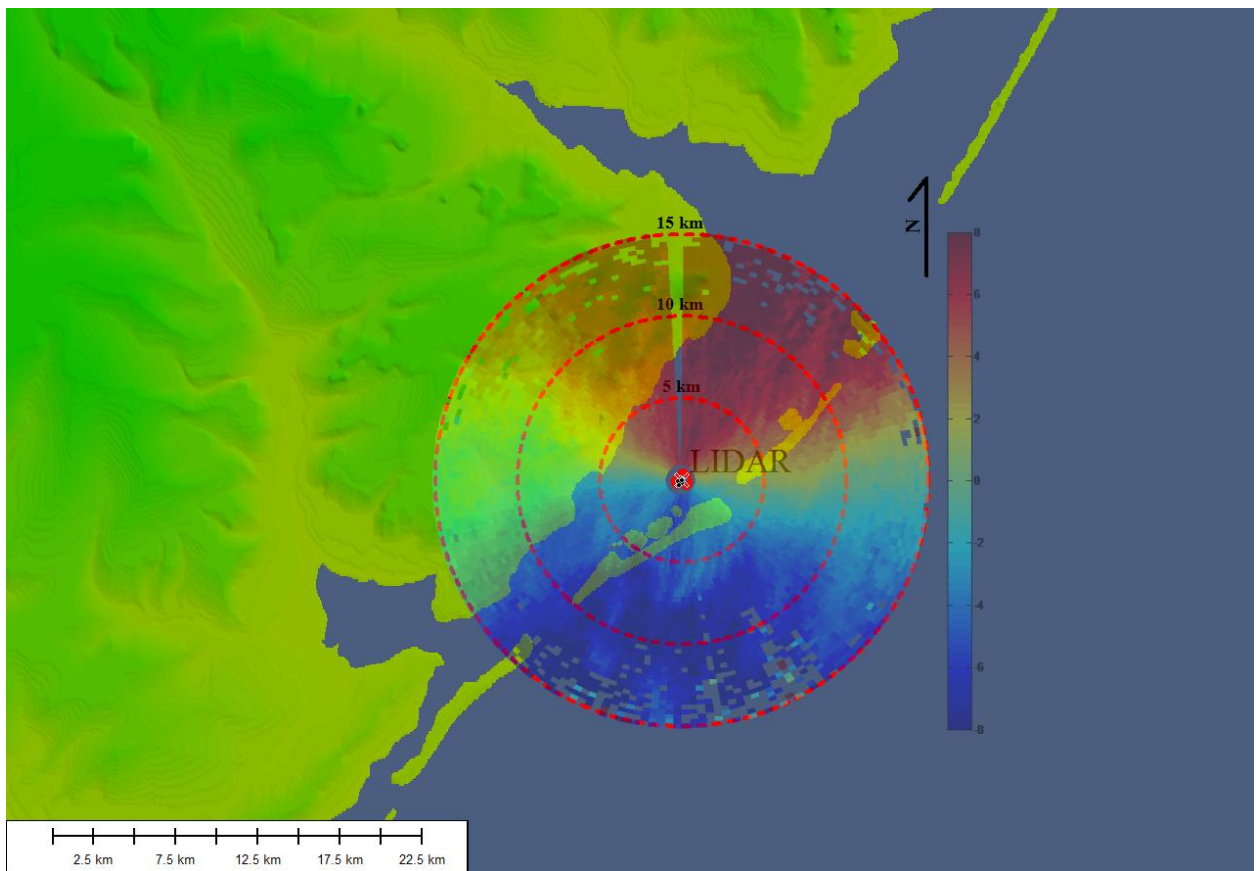


Figure 4. Offshore Terrain and lidar scan extent. Five turbines (dots) are located in the blind zone of lidar measurement, reason for hard targets in data sets. Lidar (x) location is also shown. Color bar indicates radial velocity magnitude in m s^{-1} .

2.3 Wind farm remote sensing campaign – Indiana

A Galion lidar was deployed south of the tower location. The Galion was placed on top of a 4 foot high table to elevate the scanner head above the barb-wired fencing. The lidar had clear line of sight across the entire wind farm. Four turbines were located within 2 km radius from the scanning location. The lidar was oriented to true North by pointing at the turbine located at an azimuth angle of 82 degrees. A bearing of 294 degrees was applied to the Galion. Generally, the instrument operated well with only limited down periods during the campaign. Data was available for 97.4% of the entire time period, with a few time periods lost during scan file updates and other quality checks. Multiple back-ups of the lidar data (~1.61 GB) were copied onto external hard-drives. The data quality was high and the planned scans for supporting the experiment were executed successfully. Acceptable quality was typically obtained for the lidar signal to a range of approximately 2.5 kilometers, though this varied significantly depending on daily aerosol and humidity levels. Several scanning patterns were performed to capture the incoming flow and other features near the wind farm. Table 2 shows all the scan patterns (angles, range and time taken to perform each scan) performed over the period of deployment. Figure 6 shows the percentage of individual scanning patterns performed during the campaign. Few hard-target returns from the turbines were recorded during north-west PPI and wake PPI scanning patterns.

2.3.1 Galion lidar parameters

Table 3 provides the coherent Doppler lidar parameters utilized during this study. For this experiment, the range-gate length (distance between two radial measurements)

was set at 30 m, and azimuthal spacing between beam products was $\Delta\phi = 3^\circ$ or lesser was used. As this type of lidar has a pulse repetition frequency (PRF) of 10,000 Hz, 30,000 lidar pulses averaging produced "beams" of data every 3 s. The horizontal resolution between two successive measurements is approximately 4 m, at the first range gate, to ~105 m, at farthest range-gate used for this analysis (due to diverging beams). The vertical resolution between successive elevation angles was approximately 34 m (at the farthest range-gate). The accuracy for this type of lidar was expected to be in the range $0.1 - 0.5 \text{ ms}^{-1}$ for the radial velocity product beams. A set of different simple scans (as shown above in Table 2) were assembled so that data could be obtained above and below the hub height across the site. Data from 6 PPI scans (*i.e.*, one stack) were used to produce wind speed maps. Each stack required approximately 10 minutes to complete. For more details please refer to Barthelmie et al. 2013.

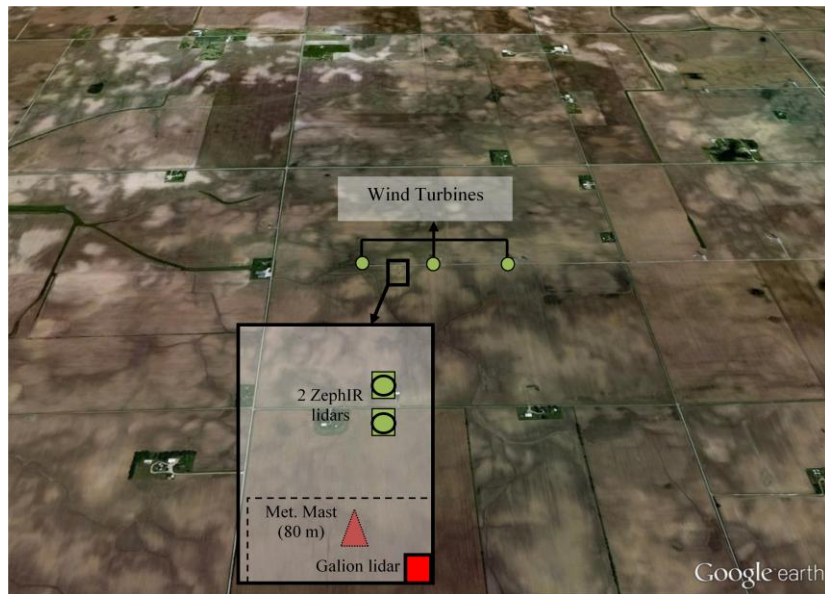


Figure 5. Remote sensing instrument setup in the Indiana wind farm.

Table 2. Scan Pattern Definitions

Scan Patterns	Azimuth Angles (deg)	Elevation Angles (deg)	Beam Separation (deg/beam)	Time Taken per Scan (minutes)	Observed Range ^a (km)
User - defined VAD	0 to 330	56	30	0.75 (45 seconds)	1.5
North West PPI (NNW)	351 to 90	1.5, 2.5, 3.5, 4.5 5.5 & 8.5	3	17.47	2.0
South West PPI (SSW)	160 to 250	1.5, 2.5, 3.5, 4.5 5.5 & 8.5	3	16.10	2.0
Wake PPI	60 to 90	8.0, 8.5 & 9.0	1	6.32	2.0
ZephIR PPI	65 to 80 & 135 to 155	4.5, 6.75, 9.0, 11.25, 13.5, 15.75, 17.5, 19.5 & 21.5	1	9.87 & 12.93	1.0
RHI Scans	83.0, 83.5, 79, 71 & 70	4.5 to 21.5	1	6.12	2.0
Galion VAD	0, 180, 270, 90, 90	70, 110, 110, 70, 90	--	0.18 (11 seconds)	2.0

^a Average range observed during day time was lower compared to night time.

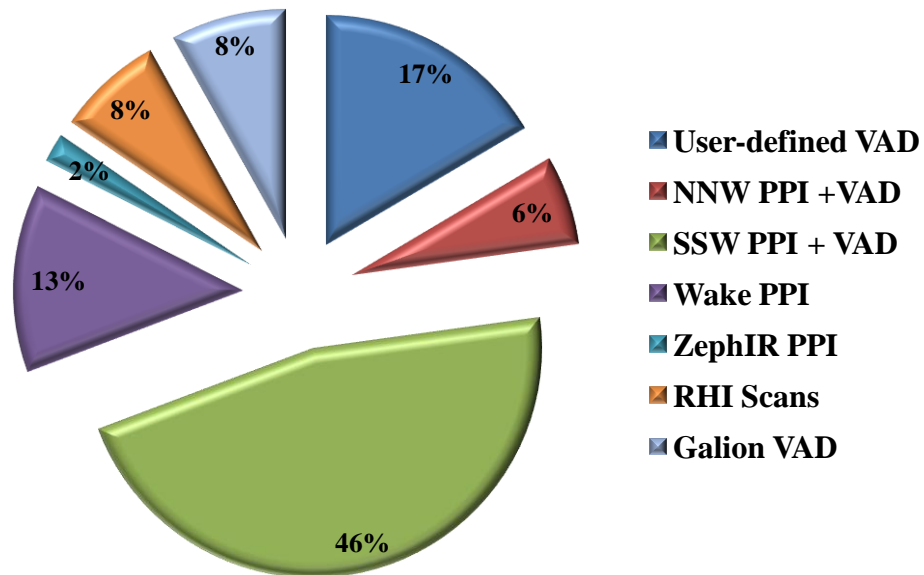


Figure 6. Percentage of scanning performed for the period of campaign (Barthelmie et al. 2012).

Table 3. Characteristics of the Galion Doppler lidar system

Operating Wavelength	1.55 μ m
Pulse repetition	10,000 Hz
Range resolution	30 m
Min range	80 m
Max range	4,000 m

2.4 CDL data filtering

Data filtering is done prior to analysis. Since the accuracy of lidar measurements decreases with increasing range due to decreasing Signal to Noise Ratio (SNR), the first step in the filtering was to remove data with an SNR below -10 dB. The second filtering step is based on the relative jump of the radial velocity value compared to the previous and following data points. If the jump recorded is more than a threshold value (5 ms^{-1}) in any direction, the data point is not considered for analysis. The threshold value is generally set in order to separate the noise from the data and must be subjectively determined because of the individual variations associated with different datasets. Thirdly, hard target returns (i.e., when the laser pulse hits an opaque object such as terrain), were also removed based on the high SNR ($> 20\text{dB}$).

2.5 COAMPS simulation set-up

The Naval Research Laboratory's Coupled Ocean/Atmosphere Mesoscale Prediction System (COAMPS) (Hodur et al. 1997) is a fully compressible, non-hydrostatic model which solves the governing equations using a centered-in-time finite

difference scheme on an Arakawa- C grid and a sigma vertical co-ordinate system. The model uses a full suite of physical parameterizations to include the effects of subgrid-scale turbulence and boundary layers, radiative heating and cooling, cumulus convection and cloud microphysics. The turbulence parameterization uses a 1.5 order, level 2.5 Mellor and Yamada scheme (Mellor et al. 1982, Suselj and Sood 2010) that computes boundary layer depth, turbulent mixing length, Richardson number and eddy coefficients to predict the change in TKE explicitly.

The lateral boundary conditions for the simulations presented herein are taken from the Navy Operational Global Atmospheric Prediction System (NOGAPS), which also provides the first-guess field for the initial conditions. Observations are assimilated into the initial conditions using the NRL Atmospheric Variational Data Assimilation System (NAVDAS). There are four nested domains with horizontal resolutions of 9, 3, 1, and 0.33 km. A total of 65 vertical levels were used in this simulation, with 15 vertical levels in the lowest 1 km. COAMPS simulations were performed for experimental site 1. The simulations was started from the NOGAPS analysis at 0000 UTC 2 June 2007 and iterated for 15 hours. A series of 15 hour simulations are run and observational analysis was performed after every 15 hour forecast. A minimum of three hours after each observational analysis period is required for the model equations to adjust to the flow conditions, therefore overlapping data sets are ignored in our analysis. Due to limited resources available, only U and V components of wind speeds were recorded at three vertical levels (10, 50 and 90 m) for 30 minute data output intervals. This resulted in 1,296 data points at every location on the COAMPS 91x91 rectangular grid. No inherent time or phase shift was observed in COAMPS forecasts, when compared to

measurements. Basic parameterization schemes in COAMPS model were used in this simulation (Hodur et al. 1997). Investigation of additional parameterization schemes, based on site conditions were not studied.

3 WIND FARM CHARACTERIZATION THEORY

Since the basic Doppler lidar output is the *radial velocity*, interpretation, and processing of the radial velocity fields can be complex, requiring the resolution of indeterminacy in the basic data through supplementary assumptions or information. Two advanced velocity retrieval algorithms were applied to the data set. Volume velocity processing (VVP) algorithm was applied to estimate the winds on a terrain-following surface at hub height. The *terrain-following surface at hub-height* is constructed by adding a vertical offset (in our case 45 and 80 m) to the surface which defines ground-level over the domain.

3.1 Volume velocity processing

To estimate the tangential components of the wind for a given radial direction and range, adjacent lidar beam measurements are used. The VVP algorithm estimates the horizontal vector that represents the localized mean wind at the specified range gate location on a conical scan (Waldteufel and Corbin 1979 and Xin et al. 1997). The VVP algorithm first groups the obtained lidar data from the volume of scans into small conical analysis volumes. The basic assumption of the VVP method is that the spatial variation of the wind within the analysis volume $\Delta r \times \Delta \Phi \times \Delta \alpha$ can be approximated by a linear function. Radial velocity data collected in the analysis volume spans from r to $r + \Delta r$, azimuth from Φ to $\Phi + \Delta \Phi$ and elevation angle from α to $\alpha + \Delta \alpha$ (as shown in Figure 7).

The radial velocity (V_r) measured by lidar is

$$V_r = u \cos \theta \cos \phi + v \sin \theta \sin \phi + w \sin \phi \quad (1)$$

where θ and ϕ are the azimuth and elevation angles of the lidar scan and u , v , w are the components of wind in x, y and z directions. For low elevation angles ($\sin \phi \sim 0$) and within the surface layer, the effect of w component on wind speed estimates is negligible. Therefore the effect of w component in our analysis is ignored. The first and second order terms of the radial velocity equation are also ignored, since the objective is only to estimate the mean wind speed.

VVP model formulation:

The VVP retrieval can be formulated as a linear, multivariate least-squares regression:

$$V_m = X_{np} \beta_p + \varepsilon_n \quad (2)$$

Where V_{ri} is the radial velocity observations as a combination of p fitted parameters β_j and independent variables X_{ij} ($i = 1, \dots, n$, and $j = 1, \dots, p$), as well as some model error ε_i .

The independent variables (“basis functions”) are functions of sampling location alone.

A least-squares or a single value decomposition (SVD) can be sought for the model; that

is, the parameters β_j can be chosen such that:

$$\chi = \|\mathbf{X}\beta - V_r\|_2 \quad (3)$$

is minimized (the bars and subscript denote the Euclidean norm). For the regression to be well behaved and robust, the basis functions \mathbf{X} must exhibit sufficient dispersion in the p space of the multivariate regression; when such sampling dispersion is lacking, we do not have enough information to reliably fit p parameters, and one or more basis functions are

collinear, that is nearly linear combinations of each other. This may result either from the definition of the function or its realization in a given sampling configuration.

The basis function parameters decomposition for VAD regressions is shown in Table 4 below:

Table 4: Fourier Series in azimuth angle, holding elevation fixed

<i>No.</i>	<i>Basis function X_j</i>	<i>Parameter β_j</i>
1	I	$(u_x + v_y)(r \cos\phi/2) + w_p \sin\phi$
2	$\sin\theta$	$u_o \cos\phi$
3	$\cos\theta$	$v_o \cos\phi$
4	$\sin 2\theta$	$(u_y + v_x) (R \cos^2 \phi/2)$
5	$\cos 2\theta$	$- (u_x - v_y) (R \cos^2 \phi/2)$
6	$\sin 3\theta$	(higher order terms)
7	$\cos 3\theta$	(higher order terms)
(1)	1	$(u_x + v_y)$
(2)	$2 \sin\phi / (R \cos\phi)$	w_p

The VVP algorithm begins by choosing the desired parameters and then determines the basis functions that will approximately yield the desired parameters in a regression model. This is achieved by specifying the simple flow model as a linearly varying wind field, Taylor series expanded about some reference point (x_o, y_o, z_o) :

$$\begin{bmatrix} u \\ v \\ w \end{bmatrix} = \begin{bmatrix} u_o + u_x (x - x_o) + u_y (y - y_o) + u_z (z - z_o) \\ v_o + v_x (x - x_o) + v_y (y - y_o) + v_z (z - z_o) \\ w_{po} + w_{px} (x - x_o) + w_{py} (y - y_o) + w_{pz} (z - z_o) \end{bmatrix} \quad (4)$$

By converting the sampling locations $(x, y, z)_i$ to functions of azimuth, elevation, and range, these position values become the desired independent variables X_{ij} (Koscienly et al. 1982, Boccippio 1995).

The first three basis functions are used to estimate the 3 wind parameters of interest using a least-squares minimization technique. Two methods are performed to calculate the fitted parameters, the regression variances, covariances, and the residual analysis are provided. The normal solution (textbook equations) will result to round-off errors and is ill-conditioned. An alternative method of solution involving singular value decomposition (SVD) is often recommended (Boccippio 1995). Both the methods are applied to the lidar data sets and it is shown that the SVD algorithm performs better compared to normal equations.

a) Normal equations or least-squares approach

Linear multivariate regressions are conventionally solved via the so-called normal equations (Browning & Wexler 1968, Koscienly et al. 1982, Doviak and Zrinc 1984, Boccippio 1995). The best linear unbiased estimate of the fitted parameters β_j :

$$\beta = (\mathbf{X}^T \mathbf{X})^{-1} \mathbf{X}^T \mathbf{V}_r \quad (5)$$

If the observations V_{ri} and model errors are normally distributed, the β_j are also the maximum-likelihood estimators (Rawlings 1998). Their variances can be calculated from the diagonal elements of the co-variances matrix \mathbf{C} :

$$C_{pp} = (\mathbf{X}^T \mathbf{X})^{-1} \frac{\mathbf{e}^T \mathbf{e}}{n - p} \quad (6)$$

$$e_n = (\mathbf{V}_r - \mathbf{X}\beta) \quad (7)$$

As noted above, computation of the cross-product matrix $(\mathbf{X}^T \mathbf{X})$ is highly susceptible to round-off errors, as is its inversion, particularly when the matrix is very poorly conditioned (*i.e.*, rank deficient). Therefore, an alternative approach based on the singular value decomposition (SVD), which is more stable and more numerically tractable problem (Belsley et al. 1980).

b) Single Value Decomposition (SVD)

SVD is best performed on the basis function matrix, \mathbf{X} , scaled to have equal column lengths (referred to as \mathbf{Z}) and results in an orthogonal decomposition of the form:

$$\mathbf{Z}_{np} = \mathbf{U}_{np} \mathbf{D}_{pp} \mathbf{V}_{pp}^T \quad (8)$$

that is, $\mathbf{U}^T \mathbf{U} = \mathbf{V}_T \mathbf{V} = \mathbf{I}_{pp}$, and the diagonal elements of \mathbf{D} are the singular values λ_p of \mathbf{Z} .

It can be easily shown that the squares of these singular values are also the eigen values of the cross-product matrix $\mathbf{Z}^T \mathbf{Z}$ and the columns of the matrix \mathbf{V} the eigenvectors. In the framework of this decomposition, the fitted parameters β_j and the covariance matrix \mathbf{C} can be expressed as:

$$\beta = \sum_{j=1}^p \left[\frac{U_{(j)} \bullet V_r}{\lambda_j} \right] V_{(j)} \quad (9)$$

$$C_{kl} = \left[\sum_{j=1}^p \left(\frac{V_{kj} V_{lj}}{\lambda_j^2} \right) \right] \frac{e^T e}{n-p} \quad (10)$$

where $U_{(j)}$ denotes the j^{th} column of \mathbf{U} . The computation can be 2-4 times expensive as the LU-Cholesky solution of the normal equations. In addition to incorporating the numerical stability of the QR decomposition, the SVD offers the added benefit of an eigen-value analysis of the system. This analysis will be extremely useful in

determining whether there is sufficient dispersion in the basis functions, as sampled; to reliably fit the p desired parameters. Insufficient dispersion in one component will be manifest if one (or more) of the singular values λ_j is small relative to the others.

Although velocities may be manually corrected prior to analysis, the current VVP uses a computationally efficient unfolding algorithm of Siggia and Holmes (1991), which is evaluated during the regression (in both the normal and SVD solution techniques).

An iterative regression is performed, by minimizing the residual errors, analyzing the covariances and projection matrix calculation. The regression proceeds by once calculating the independent variable matrix \mathbf{X} . A number of regression passes are then performed, each pass masking out data points that influence the regression (due to their position in its \mathbf{X} space) or appear to be outliers. The various outlier analysis used in this VVP computation are the Cooks D and DFFITS. Suitable threshold criteria for these statistics are often taken as $4/n$ and $2(p/n)^{0.5}$, respectively. The condition number (CN) analysis is also performed, where CN greater than 9 and less than 2 are used for data rejection. The CN helps in reducing the collinearity in the regression parameters. For more effects of CN on the regression parameters, please refer to Boccippio 1995. In the iterative regression used here, such points are flagged out of the dataset after each pass and compose about 10% of the total sample. The current regression also uses a fixed number of passes rather than error-convergence criterion. This procedure seems reasonable as successive rejection of data points will both homogenize the cluster of points in the \mathbf{X} space and degrade the model's conditioning. As shown in Boccippio (1995), conservative fixed number of passes (two or three) is recommended, which reduces the model error by 10% - 80% with relatively little damage to the conditioning.

Each of these volumes uses 30 to 40 radial velocity data points, depending on the size of the conical analysis volume. The VVP estimates are dependent on the size of the analysis volume. The number of radial velocity data points in each analysis volume needs to be carefully considered for converged solution. Large analysis volumes contain more radial velocity data points, but the wind field estimates becomes questionable due to violation of the linear wind assumption (Waldteufel and Corbin 1979). On the other hand, with too few radial velocity points, the solution can become unstable, which increases the relative error in wind speed estimates (Boccippio 1995). The bias in wind speed for different sector sizes for similar radar analysis is estimated to be approximately between $0.5 - 1 \text{ ms}^{-1}$ (Boccippio 1995). Therefore, through trial and error, the size of the analysis volume for this case was chosen as: $\Delta r = 210 \text{ m}$, $\Delta\Phi = 20^\circ$ and $\Delta\alpha = 0.2^\circ$. For the given unit analysis volume, the algorithm automatically loops through all analysis volumes, applying a least squares minimization scheme to obtain the solutions. Once the wind speeds are obtained for the volume of scans, they are placed in the center of the analysis volume. Wind speeds above the maximum velocity threshold ($> 25 \text{ ms}^{-1}$) of the lidar are ignored.

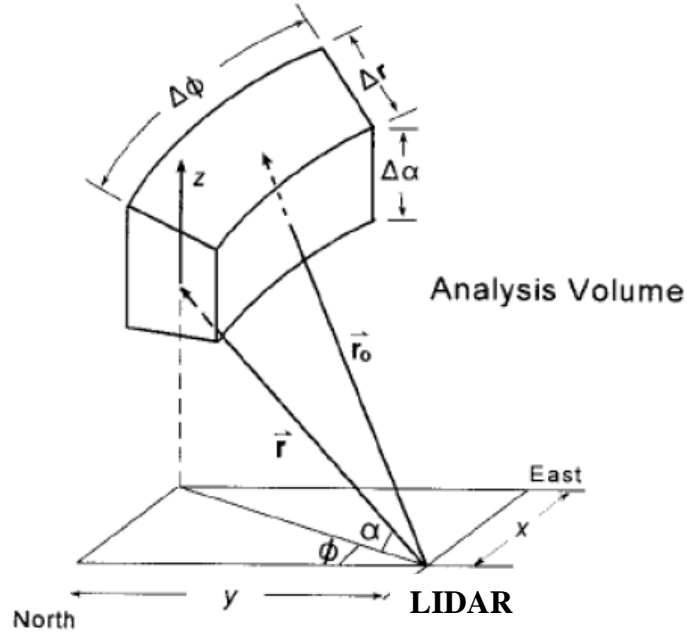


Figure 7. Volume velocity processing algorithm analysis volume (Xin et al. 1997).

3.1.1 Interpolation of winds to hub height

Winds obtained from the VVP algorithm at different heights are used to generate a terrain-following wind map at hub height. At each grid point, there are normally 13 velocity values at different heights which can be used to interpolate speeds to the appropriate level. However, due to the terrain-blocking at lower levels of the lidar scans, and noise caused by atmospheric conditions, the required scan levels were not always available. To overcome this problem, three different techniques were used to complete the interpolation:

- i. At grid points where there are at least two available data points at different heights, and the interpolating level is in-between these data, a linear interpolation is used to obtain the wind speed.

- ii. At grid points where there are at least two available data points at different heights, but the interpolating level is below these data, wind speed at that level is obtained using the theoretical wind power law (Peterson and Hennessey 1978), with locally adjusted exponent value. The exponent value is calculated based on the velocity measurements available at the higher level scans. The power law equation is given below.

$$\left(\frac{U_1}{U_2}\right) = \left(\frac{Z_1}{Z_2}\right)^\alpha \quad (11)$$

Where, U_1 and U_2 are wind speeds at heights Z_1 and Z_2 , and α is the Hellman coefficient or sometimes called as the power law exponent. The power law exponent is an empirically derived coefficient that varies dependent upon the stability of the atmosphere. Measurements from higher elevation angles (within 150 m AGL), are chosen to estimate the exponent value for each grid cell.

- iii. At grid points where there is only one available data point in the vertical direction, the interpolating level is obtained by using the wind power law, where the power law exponent from the previous time period is used, assuming no change in atmospheric conditions. The time period between instances where wind speed data was available only at one vertical level was short (≤ 20 minutes). The stability conditions are not expected to change within the short period.

This procedure is applied for the entire period of observation and the results are provided below. Figure 8 shows the percentage of power law used at various locations during the

entire period of study. Note that for 90 % of the data set, the power law is not required to estimate winds on the terrain-following surface. For locations, at the north-west and south-west ridges, where the terrain ‘dips’ below the horizon, extrapolation of winds onto the terrain-following surface is performed using power law. The maximum extrapolation distance used in power law calculations is approximately 20 m (as shown in Figure 9). The errors associated from the usage of power law should be a subject of further research. The use of power law can be assumed viable for this case, since the extrapolation distance used is small and local stability conditions are used in calculating the winds at the interpolating level.

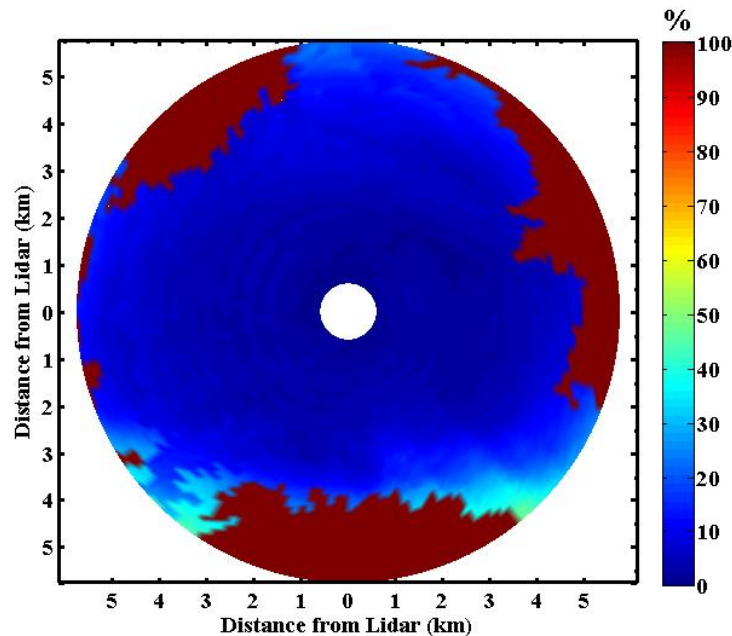


Figure 8. Percentage of power law used to obtain an 80 m terrain following surface from lidar measurements. The color bar represents the percentage of power law used over the entire period of study. A total of 3,459 observations were included for this analysis.

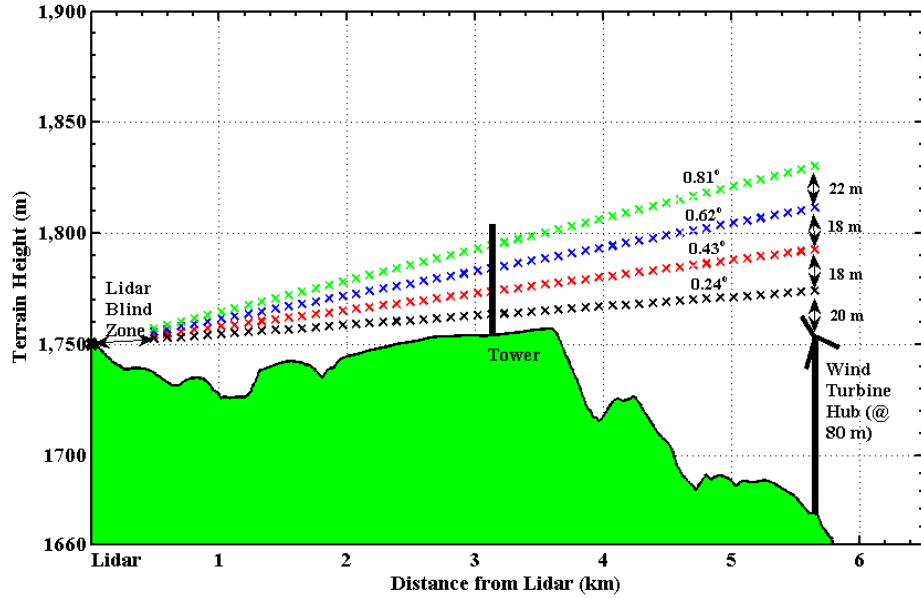


Figure 9. Terrain cross-section from lidar location, through the tower, till the end of scan radius is shown above. Lidar (x) and tower location are shown. Scans at various elevation angles are displayed. The power law ‘dip’ height used to estimate wind speed at terrain-following surface (80 m hub height) is approximately 20 m.

3.2 Wind farm layout design

Even though the length of the deployment reported here was much too short to be considered climatological, a simple model for turbine placement and wind farm design was explored for demonstration purposes. This section is based on lidar-derived total machine power output. The turbine locations are roughly placed based on maximum machine power output estimated from lidar and a constant $10D$ (where, D is the diameter of the turbine) turbine spacing. These results are based purely on lidar measurement and different layout designs can be evaluated based on the various constraints applied.

The assumptions used for wind farm layout design are presented below.

Assumption 1: Two dimensional Cartesian grids (x, y) of size 90 m x 90 m is overlain over the polar grid cells (measured by the lidar). This assumption implies that there is negligible variation of the surface roughness within a polar coordinate grid cell. The

solution estimated in this paper is represented by N Cartesian coordinates (x_i, y_i) , $i = 1 \dots N$, where N is the number of wind turbines for the given project.

Assumption 2: All wind turbines are assumed to have the same power curve function.

The total yield can be estimated based on the distribution of wind speed at every location (on the grid at hub height) and the assumed power curve. The period of observation is assumed to be representative of longer periods, for the purposes of this demonstration.

Also, the wind turbine is assumed to be oriented perpendicular to the mean wind direction at any given period of time.

Assumption 3: Any two turbines in a wind farm are separated from each other by at least ten rotor diameters. This constraint attempts to ensure that wind profiles have recovered sufficient energy before interaction with another turbine. Therefore, given the rotor diameter D, the distance between two adjacent turbines (x_i, y_i) and (x_j, y_j) should satisfy the inequality $(x_i - x_j)^2 + (y_i - y_j)^2 \geq 100 D^2$. This assumption is based on rules of thumb from the industry (Manwell et al. 2001). Additional constraints could be placed on the distance between each turbines based on the wind direction, but are not in this demonstration design process.

3.2.1 Global optimization

Global optimization algorithms (such as Genetic Algorithms) were explored for layout optimization. Turbine wake interaction effects are also included in the model for optimized layout. Details about the wind farm wake interaction effects are explained in section below. The methodology from Kusiak et al. 2010 is implemented. Please refer to Kusiak et al. 2010 for further details about the optimization procedure. Genetic

algorithm toolbox from MATLAB[®] is used for the results below. Since global optimization algorithms (including genetic algorithms) involve several parameters to be altered, different wind farm layout can be obtained for different parameters chosen. Therefore, future investigation is needed for evaluating the optimal parameters for wind farm layout. Sample layouts are provided in sections below.

3.2.2 Wind farm layout wake interaction effects

Wake loss is an important factor in considering wind park layout design. When a uniform incoming wind encounters a wind turbine, an expanding wake behind the turbine occurs (Kusiak et al. 2010). A portion of the free stream wind speed will be reduced from its original speed. The velocity deficit is defined as the fractional decrease of free stream wind speed due to the wake of a turbine. Several wake expansion models are provided in the literature (Jensen 1983, Ainslie 1988, etc.). A simple industry standard park model is used for analysis below.

As an initial analysis, wind farm wake's measured by lidar near site 2 is compared to industry standard models. In this analysis, a simple park model (shown below) is compared to estimates from lidar measurement. Wind velocity deficit, δV is estimated by:

$$\delta V = 1 - \left(\frac{v_{down}}{v_{up}} \right) = \left(1 - \sqrt{1 - C_t} \right) / (1 + kd/R)^2 \quad (12)$$

where C_t is the thrust coefficient of the turbine, k is the wake spreading constant, and d is the distance behind the upstream turbine following wind direction. For simplicity, k and C_t are assumed constant in this analysis. This is reasonable since for

most of the wind turbine operating region, the values do not vary by significantly. In this analysis, C_t is considered as 0.8 and wake effects based on several decay constants (k) are analyzed.

For multiple turbine wake interaction effects, the total velocity deficit from each turbine is computed by:

$$\left. \begin{aligned} \delta V_i &= \sqrt{\sum_{j=1, j \neq i}^N \delta V_{ij}^2} \\ \text{and} \\ \delta V_{ij} &= \left(1 - \sqrt{1 - C_t}\right) / \left(1 + k d_{ij} / R\right)^2, \\ d_{ij} &= \left| (x_i - x_j) \cos \theta + (y_i - y_j) \sin \theta \right| \end{aligned} \right\} \quad (13)$$

where for any two turbines located at (x_i, y_i) and (x_j, y_j) in a wind farm, δV_i is the total velocity deficit at turbine i from all the other turbines ($j = N-1$), N is the total number of turbines, δV_{ij} is the velocity deficit at turbine i in the wake of turbine j and d_{ij} is the distance between turbine i and j , projected on the wind direction θ . However, for a given wind direction, not all turbines generate the wake effects at turbine location i .

4 LIDAR DATA VALIDATION

Since tower (cup and vane) measurements were available only at site 1, accuracy of lidar wind speed estimates at site 1 were validated to tower measurements. Near continuous wind measurements were collected over a period of one month at experimental site 1. Two cup anemometers and vanes were positioned at 50 m, 50.2 m and 48 m, respectively, on a meteorological tower (location shown in Figure 3). An analysis of the measurements was performed to check their value in comparison with lidar measurements. A detailed error analysis other than the given validation with tower data of the VVP retrieval algorithm is a subject of further study.

Tower Comparison at Site 1:

The lidar measurements are interpolated to 50 m above ground level (AGL) and are compared to tower measurements for the entire period of observation. The 10 min integrated mean wind speeds/directions and standard deviations for both the tower and lidar measurements are presented in Table 5 and Table 6, respectively. The time series plots of wind speed and direction for tower and lidar is shown in Figure 10. It can be seen that the lidar and tower measurements are in close agreement with the mean wind differences equal to 0.06 ms^{-1} . The 10 min root mean square (RMS) error between the lidar and tower is estimated to be approximately 1.18 ms^{-1} . Because of the inherent differences in the data acquisition method, particularly the sampling frequency (over 10 minute period: 1200 tower measurements -- versus 1 lidar measurement), the RMS differences are dependent on the averaging time period. That is, increasing averaging times would yield reduced RMS differences (see Table 7). In the limiting case, where the

time average was over the entire data acquisition period, the RMS difference reduces to 0.06 ms^{-1} (*i.e.*, $9.67 \text{ ms}^{-1} - 9.61 \text{ ms}^{-1}$).

Table 5. Tower – Lidar wind speed statistics over the period of observation at Site 1

Instrument	Mean (ms^{-1})	Standard Deviation (ms^{-1})	10 minute RMS Difference (ms^{-1})
Tower @ 50 m	9.67	3.60	1.18
Lidar @ 50 m	9.61	3.61	

Table 6. Tower – Lidar direction statistics over the period of observation at Site 1

Instrument	Mean (deg) ^a	Standard Deviation (deg) ^a	10 minute RMS Difference (deg) ^a
Tower @ 50 m	168.24	36.94	19.40
Lidar @ 50 m	170.34	37.01	

^aData utilized between 60-300 deg

Table 7. Wind Speed RMS difference statistics for various time averaging periods at Site 1

Wind speed RMS difference	10 minute RMS difference (ms^{-1})	1 Hour RMS difference (ms^{-1})	24 hour RMS difference (ms^{-1})
@ 50 m	1.18	0.72	0.46

Very good agreement is seen between the lidar and tower direction as shown

Figure 10. The mean difference in direction is approximately 2° . The lidar follows the

abrupt changes in direction accurately with a 10 minute RMS difference of approximately 19° . Similarly, longer averaging times would yield lower RMS differences. The reason for the discrepancy in measurement is most likely to be due to the spatial averaging performed by the lidar measurements and the differences in temporal averaging for the ten minute period. That is, the lidar obtains one stack of PPI's during this period, while the wind vanes collect data continuously at 2 Hz for each ten minute period. Scatter plots of lidar versus tower wind speed and direction are shown in Figure 11. Standard regression analyses resulted in a fit with 94 % correlation. It was sometimes the case that the wind direction caused the lidar “look-direction” towards the tower to be nearly perpendicular with respect to the mean flow direction. This created a more stringent test for the retrieval algorithm than if the tower had been more directly and consistently along the mean wind direction from the lidar. The scatter plot of lidar versus tower wind speed orthogonal to the lidar mean wind direction (170°) is shown in Figure 12. Correlation between the tower and lidar measurements is 89 %. U-component (N-S) and V-component (E-W) scatter plots between lidar and tower for the period of observation are shown in Figure 13. The correlation coefficient of the U component is approximately 95%, while the correlation coefficient for the V- component is calculated to be 88%. Spatially averaged lidar observations are a likely reason for the differences between tower and lidar. Figure 14 shows tower and lidar wind roses for the entire observation period. Each wind rose was divided into 12 directional sectors (30° per sector) with 5 ms^{-1} wind speed bins. Some effect of spatial averaging by lidar measurements can be observed in Figure 14, though generally the estimates from both lidar and the tower data are in relatively close agreement. This provides evidence of the accuracy of the retrieval

algorithm applied to lidar data. Since only one tower was placed in the observation site, further validation could not be performed.

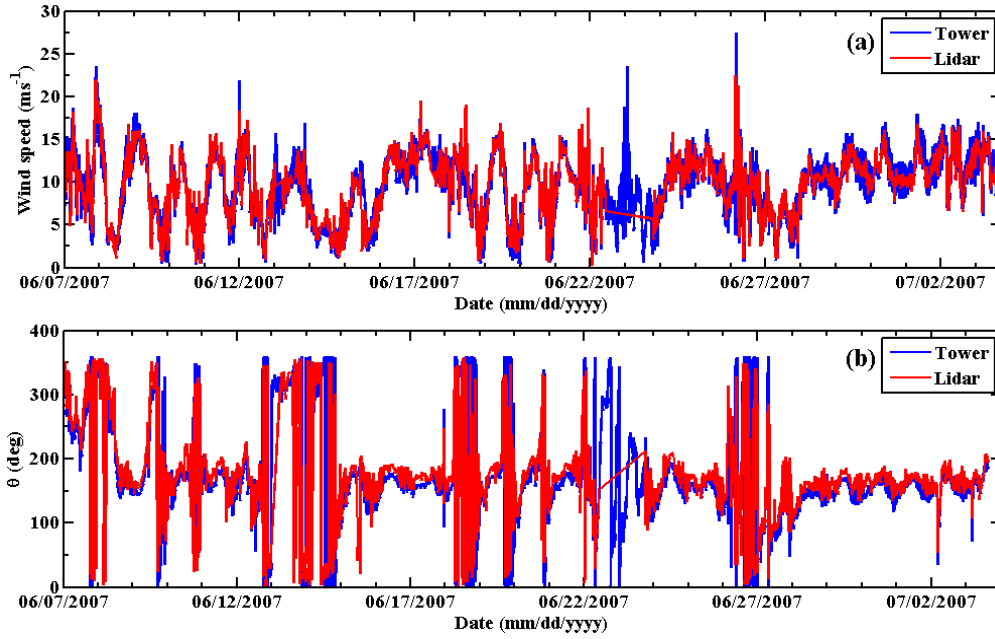


Figure 10. (a) Comparison between one minute averaged tower and ten minute interpolated lidar wind speed at 50m. (b) Comparison between one minute averaged tower and ten minute interpolated lidar direction at 50 m. A total of 3,459 ten minute periods are chosen for both figures. Gaps in the series correspond to bad signal-to-noise ratio at those time periods, hence was neglected.

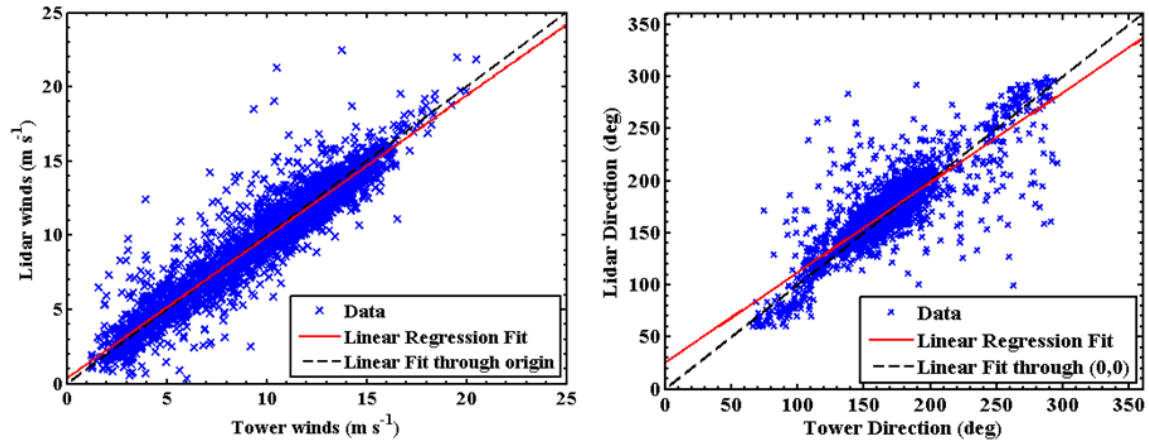


Figure 11. (a) Scatter plot of tower versus lidar wind speed at 50 m. Standard regression analyses produced the best fit line ($y = 0.95x + 0.4$), showing 94 % correlation (solid line) and the linear fit through origin is also shown (dotted line), (b) Scatter plot of tower versus lidar wind direction at 50 m. Data analyzed between directions 60-300 deg.

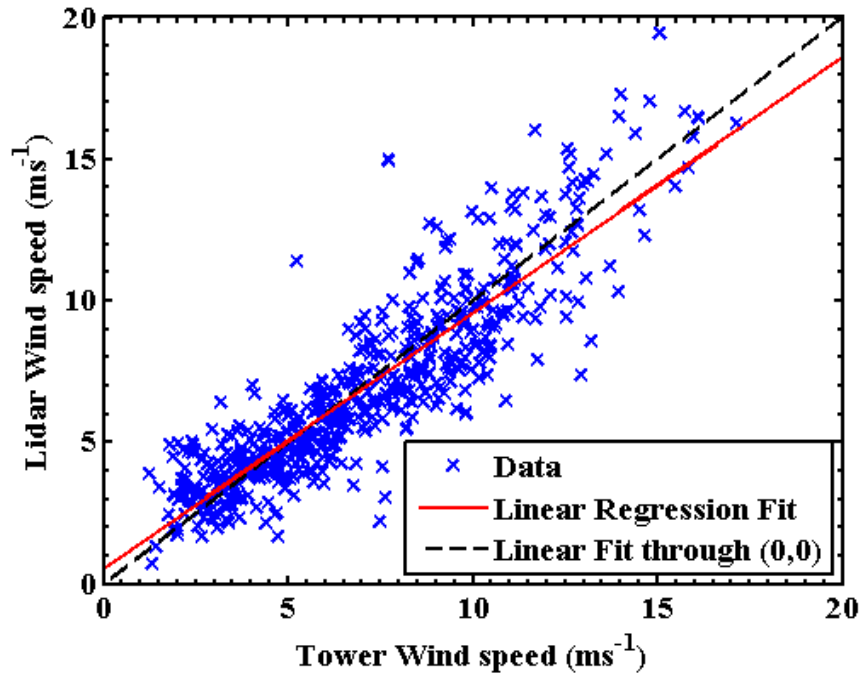


Figure 12. Scatter plot of tower versus lidar wind speed at orthogonal directions to mean wind direction ($170^\circ \pm 45^\circ$) at 50 m. A linear regression fit ($y = 0.9x + 0.56$) showing 89 % correlation (solid line) and the linear fit through origin is also shown (dotted line).

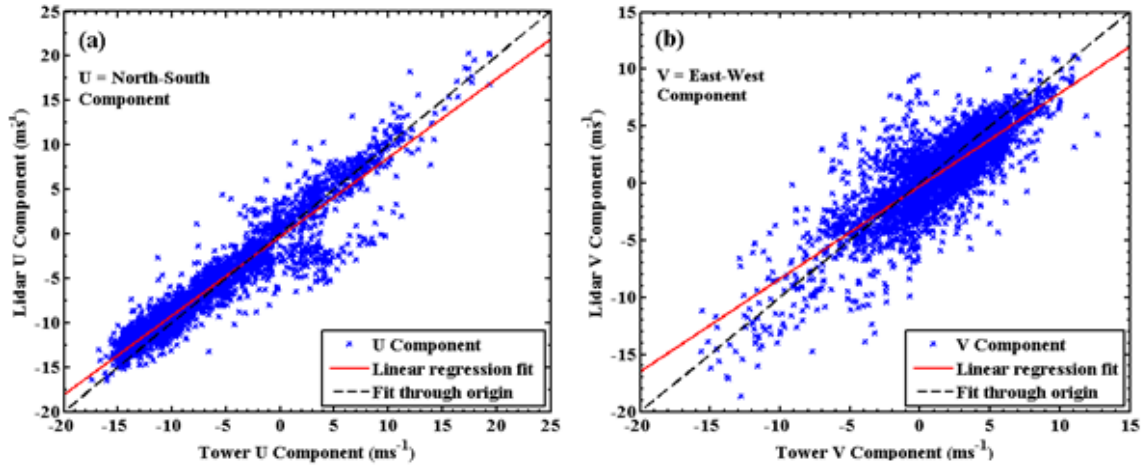


Figure 13. (a) U –component scatter plot of tower versus lidar at 50 m. A linear regression fit ($y=0.89x - 0.27$) showing 96% correlation (solid line) and the linear fit through origin is also shown (dotted line). (b) V –component scatter plot of tower versus lidar at 50 m. A linear regression fit ($y=0.81x - 0.2$) showing 88% correlation (solid line) and the linear fit through origin is also shown (dotted line).

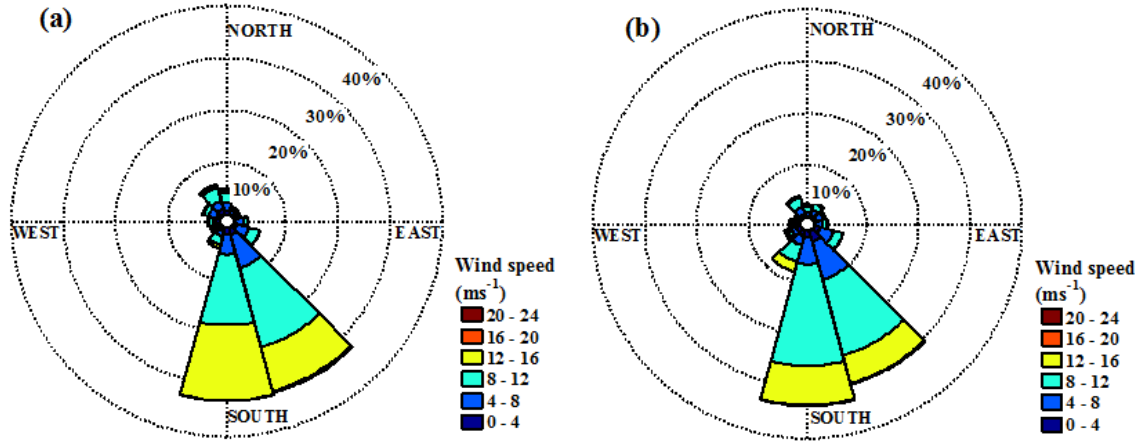


Figure 14. (a) Tower wind rose for the period of observation at 50 m (b) Lidar wind rose for the period of observation at 50 m. Wind speeds (6 bins of 4 ms^{-1}) were divided into twelve directional sectors. Percentage circles (10, 20, 30 and 40%) are also shown.

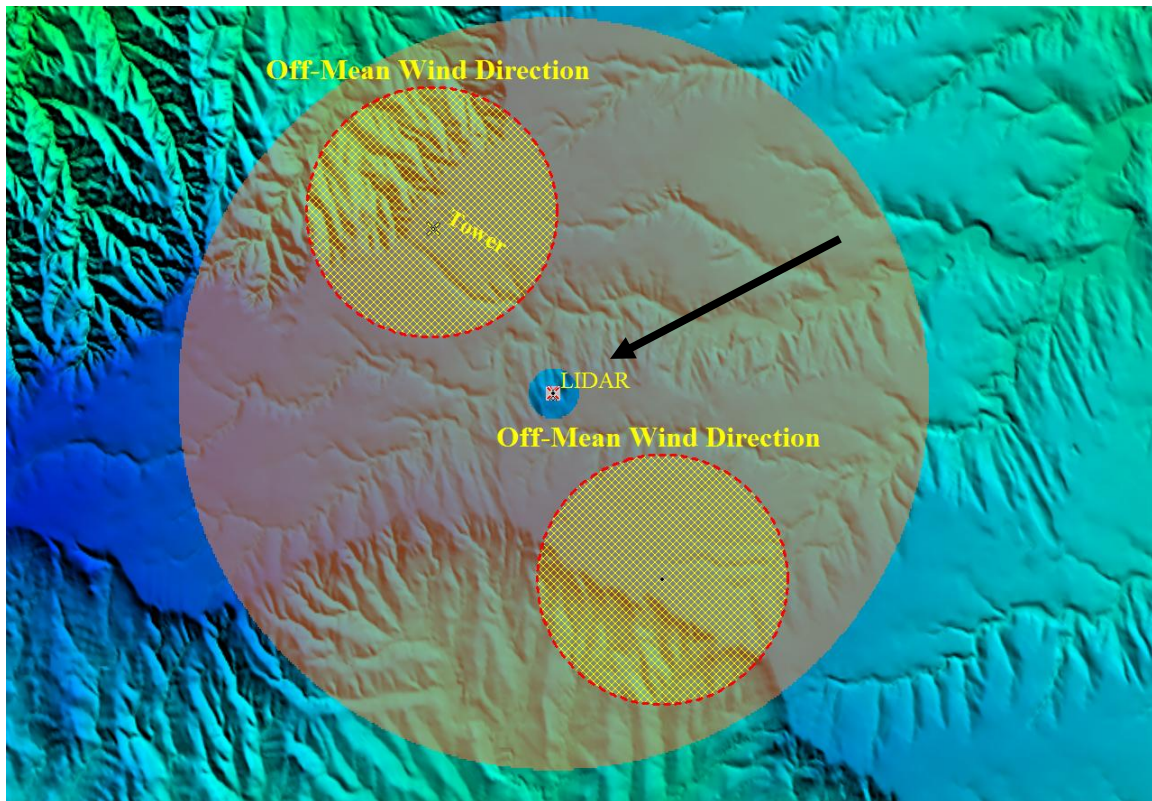


Figure 15: Off-mean wind directions at tower locations. Lidar measurements perpendicular to the tower direction were collected for correlations.

Tower comparison at Site 3 – Indiana wind farm:

Several days of Galion lidar scans were analyzed to capture the incoming wind flow at the Indiana wind farm. Different retrieval algorithms were applied to the lidar data and were compared to tower measurements at the site. Figure 16 below shows time-series of winds and direction comparison between two retrieval algorithms a) modified volume velocity processing (Krishnamurthy et al. 2012) and b) SVD based VVP algorithm as explained in section 2 of this article, and tower measurements at hub height (80 m). In Figure 16 and Figure 17, lidar wind speed and direction measurements 1 km away from the tower are shown. The wind evolution is not significant during night time, while during day time due to high turbulence, wind speed differences of greater than 1m/s is observed. Wind directions vary from N-NE during night time to West during day-time. Measurements during night-time are effected by wake of the wind turbines in the vicinity of the campaign.

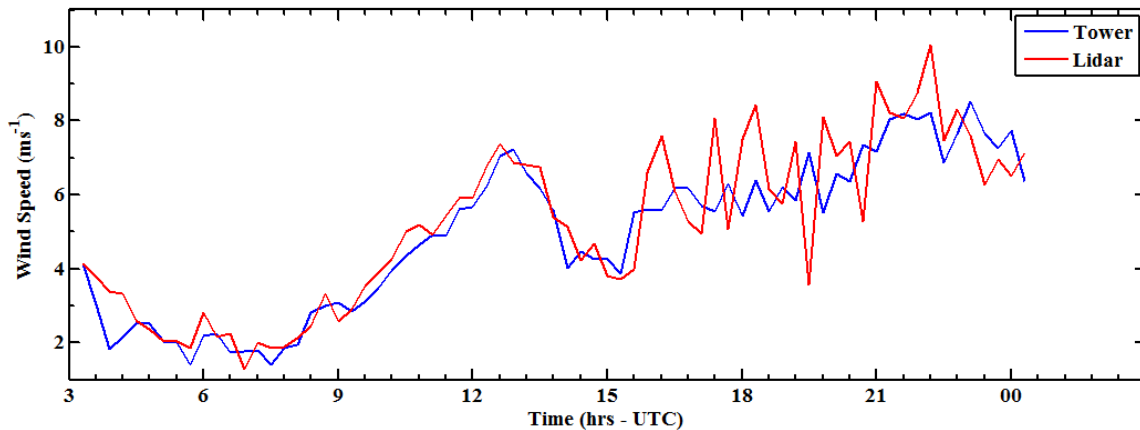


Figure 16. Tower and lidar wind speed comparison at the Indiana wind farm from PPI scans.

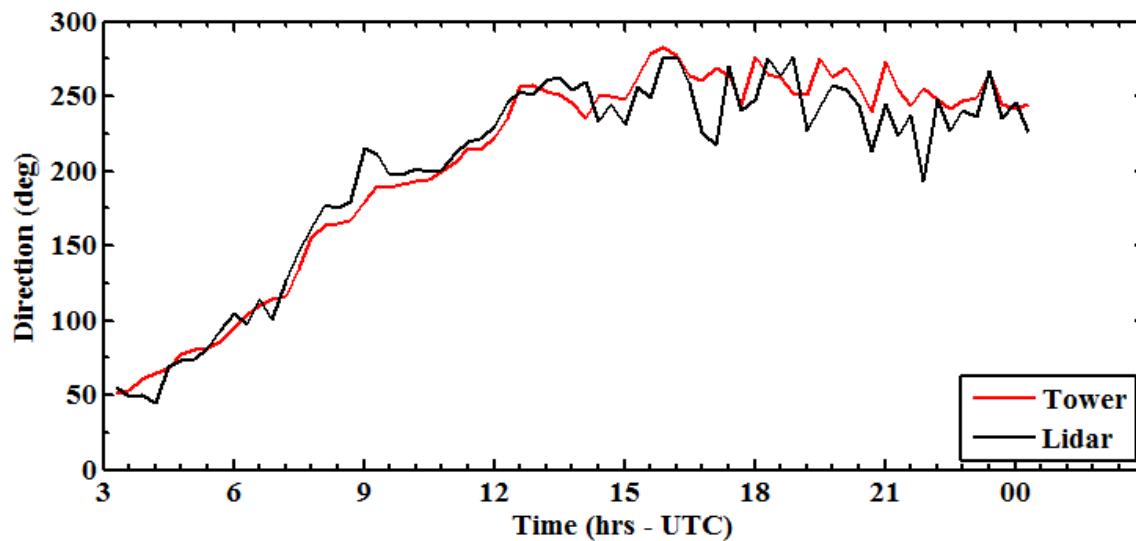


Figure 17. Tower and lidar direction comparison at the Indiana wind farm from PPI scans.

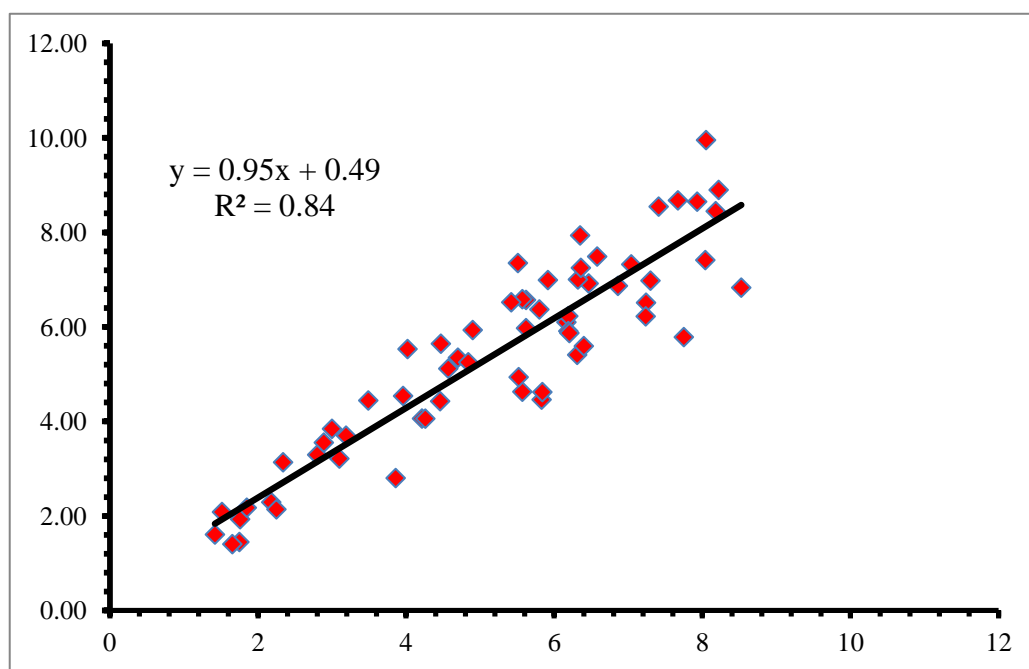


Figure 18. Wind speed comparison between tower and lidar (VVP algorithm) at a wind farm in Indiana. The lidar measurements were picked one (1) km ahead of the tower measurements. Correlation of wind speed is 84%.

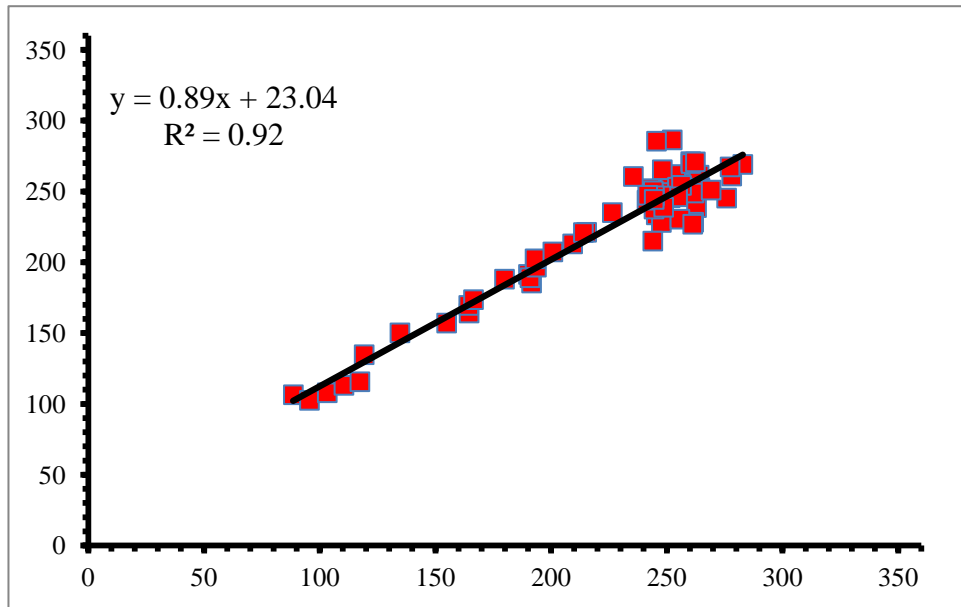


Figure 19. Direction comparison between tower and lidar (VVP algorithm) at a wind farm in Indiana. The lidar measurements were picked one (1) km ahead of the tower measurements. The correlation of wind direction is 94%.

5 WIND FARM CHARACTERIZATION ANALYSIS

5.1 Terrain-following wind maps

One of the key advantages of 3D scanning coherent Doppler lidar is to generate wind maps on a terrain-following layer at hub height for the region of interest. The wind speed data was placed on a 12 km x 12 km grid domain and overlaid on a digital terrain model. The resultant map covers a geographic area of 144 square kilometers and is comprised of approximately 9,150 data points on the terrain-following plane. Figure 20 shows the three dimensional image of the terrain-following wind field at 80 m hub height. Such spatially resolved wind maps (on terrain-following surfaces at hub-height) may aid developers to gain more complete understanding of the spatial variation of winds within a prospective wind farm. Based on visual inspection of the wind map, it is straightforward to locate the area with maximum winds. It can be observed from Figure 20 that for the period of observation, maximum mean wind speeds of greater than 12 ms^{-1} are observed near the north-western ridges and minimum winds up to 5 ms^{-1} are observed near the south-western section of the domain. For this site, locations near the northern ridge and on the western side of the plateau would result in maximum wind power production. Analyzing many days of lidar data, it was found that the winds in this region tend to channel across the northern ridge. Although the mean wind direction at hub height is approximately from the south, rapid changes in wind direction and wind shear are observed for many days and could be of interest for wind farm developers.

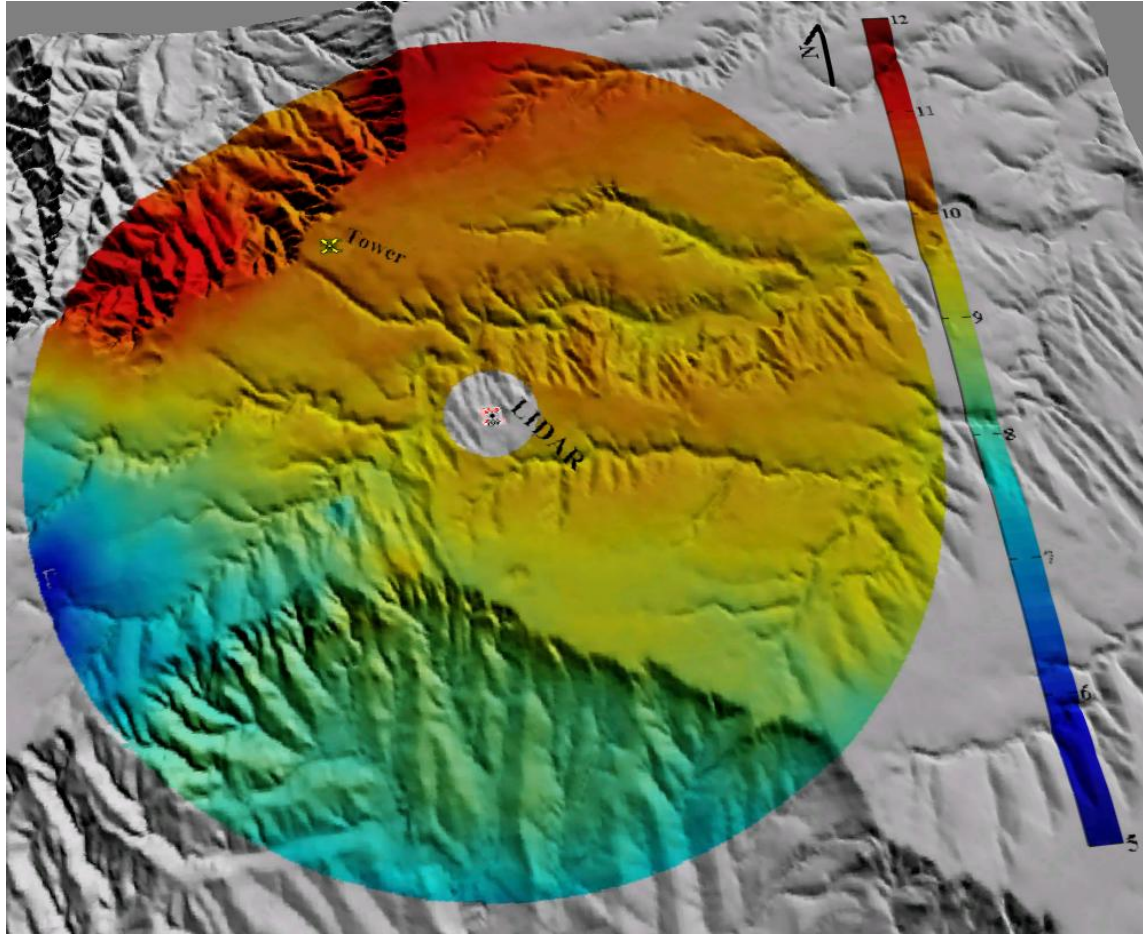


Figure 20. Lidar terrain-following averaged wind speed measurement at 80 m hub height. The colour bar represents wind speed from 5 to 12 ms^{-1} . The lidar is at the centre and the tower is located 3.42 km north-west of the lidar. The radius of the scan is 5.75 km.

5.2 Wind distributions

Of course, the energy content of the wind depends not only on the mean wind speed but also on wind speed distribution. Lidar is capable of providing wind speed distributions at every point over the entire spatial domain. Evidence is provided for two hypotheses:

1) Modern 3D-scanning lidar can measure accurate wind speed distributions over large areas from one central location, and

2) The wind speed distribution can be strong functions of spatial position, especially for wind farms in or near complex terrain.

The distribution of the winds from the tower is compared to those estimated from the lidar at the tower location. Since the cup anemometers on the tower are located at a height of 50 m (AGL), the lidar data was interpolated to this height, as given in Section 4, and the distributions are compared. The winds measured on a terrain-following surface at 50 m are binned into 30 wind speed categories, allowing estimation of the wind speed distribution. As observed in Figure 21A, tower and lidar distributions compare reasonably well. Radial and transverse wind speed distributions between lidar and tower are compared in Figure 21B and Figure 21C, respectively. To calculate the wind speed distributions in radial and transverse directions, wind speeds were binned into four 90° sectors based on the wind speed directions. Two sectors along the radial direction, *i.e.*, $170 \pm 45^\circ$ and $350 \pm 45^\circ$, and two sectors along the transverse direction, *i.e.*, $80 \pm 45^\circ$ and $260 \pm 45^\circ$. The distributions in the transverse directions are less converged, due to insufficient data points observed in the two sectors. The lidar wind speed distributions in radial and transverse direction compare reasonably well with tower distributions.

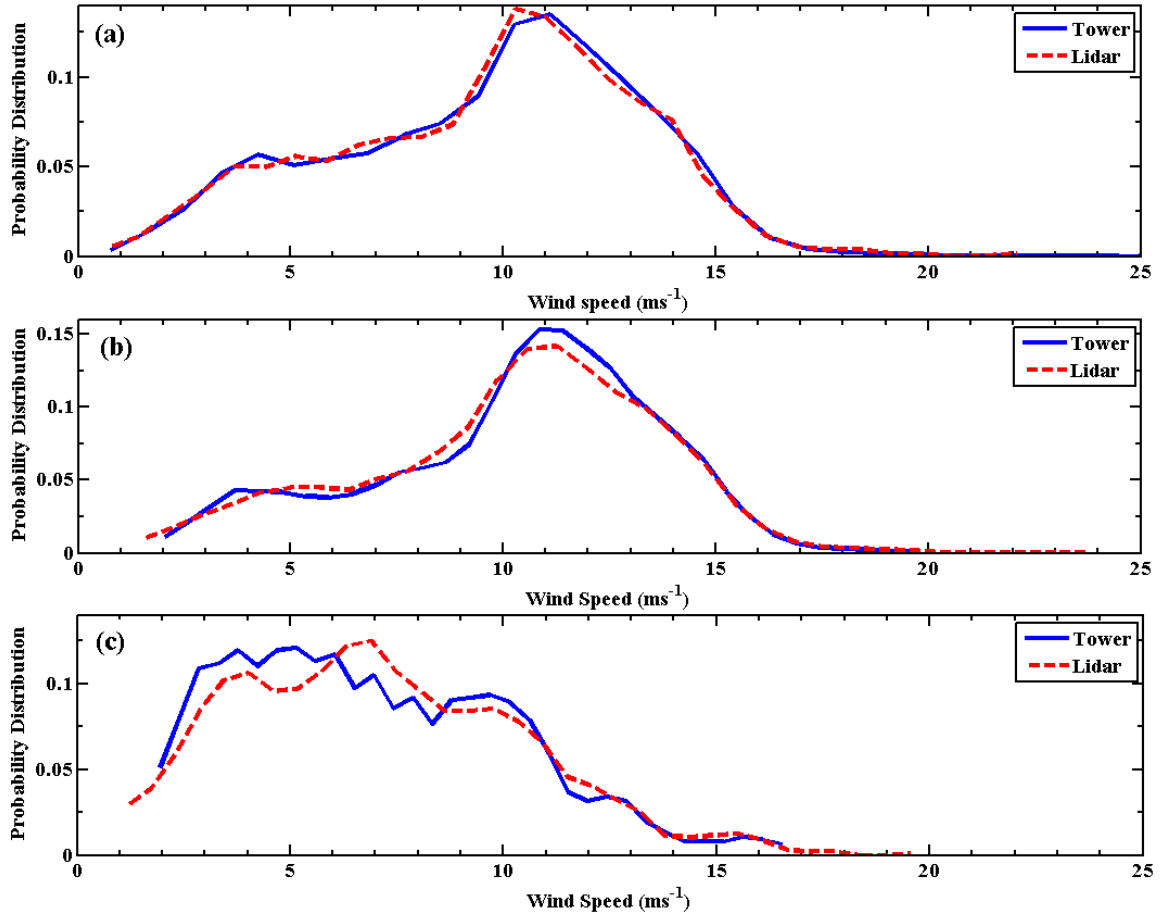


Figure 21. (a) Distribution of wind speed comparison between tower and lidar measurements at 50 m (from all directions). (b) Wind speed distribution between the tower and lidar in the radial direction at 50 m. Wind speed data selected from directions $170 \pm 45^\circ$ and $350 \pm 45^\circ$ were chosen for this distribution (mean wind direction is 170°). (c) Wind speed distribution between the tower and the lidar in the transverse direction at 50 m. Wind speed data selected from directions $80 \pm 45^\circ$ and $260 \pm 45^\circ$ were chosen for the distribution (mean wind direction is 170°). The distribution is less well defined due to reduced amount of data perpendicular to the mean wind direction.

In order to understand the variation of winds with height, the distributions at various vertical levels within the rotor swept area have also been analyzed. In Figure 22, the distributions from lidar at 50 m, 80 m and 110 m (AGL) are compared. A more apparent bi-modal distribution is observed at higher elevations. The lower mode is at approximately $4\text{--}7\text{ ms}^{-1}$ and the upper mode is approximately at 10 ms^{-1} .

Based on lidar estimates, it can be observed that different distributions are obtained at various locations (three) within the region (Figure 23). The locations shown as cross-marks (x) in Figure 3 observed different wind speed distributions. The energy estimated by each of these distributions varies significantly. These measurements could be used to estimate the error from current mesoscale, computational fluid dynamics (CFD) and linear wind resource prediction models (such as WAsP etc.,).

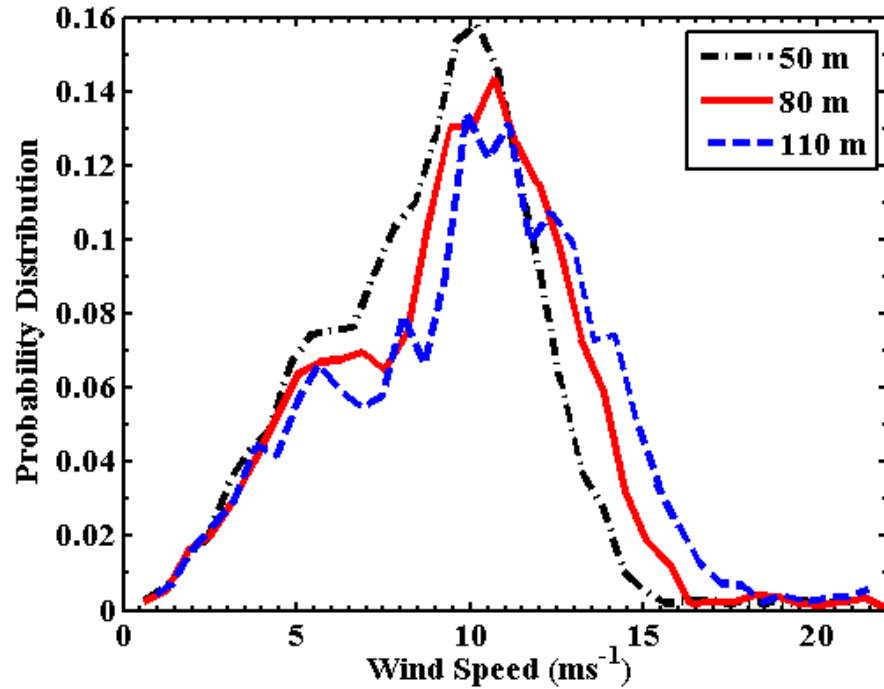


Figure 22. Distribution of wind speed from lidar at three vertical levels within the turbine rotor region from lidar measurements, showing bimodal distribution (i.e., one peak near $5-7 \text{ ms}^{-1}$ and another at 10 ms^{-1}) at 50 m, 80 m and 110 m heights (from all directions)

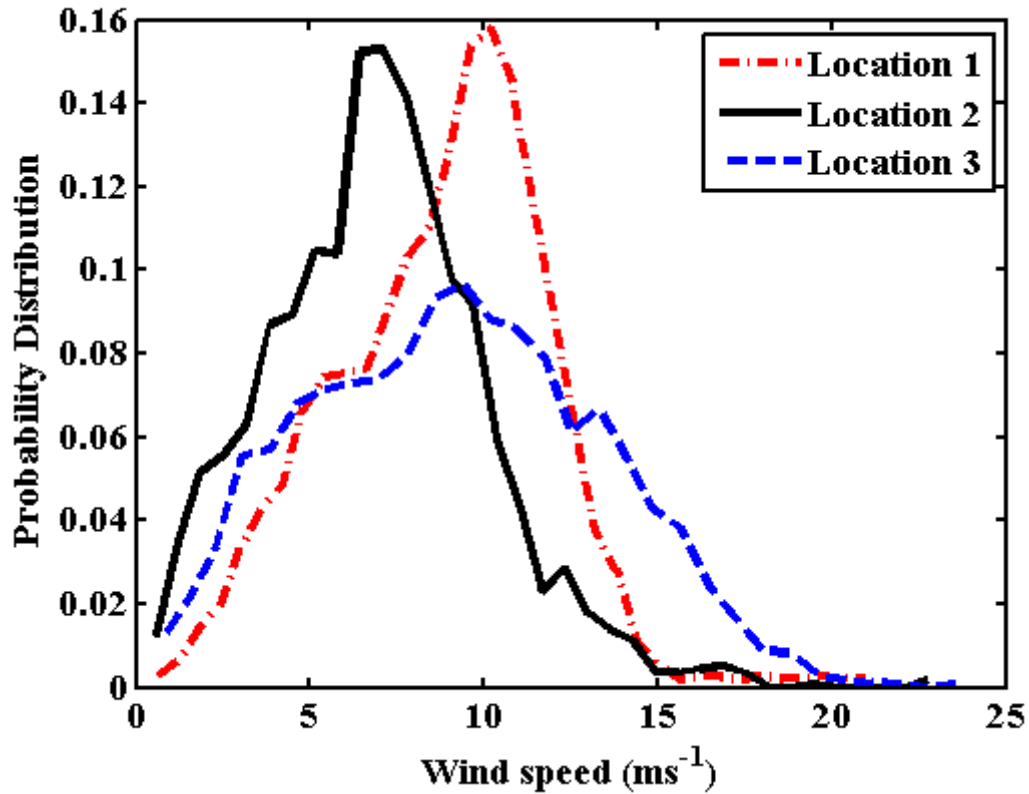


Figure 23. Different distribution of wind speed observed at various locations from lidar measurements, 50 m above ground level (from all directions). Locations 1, 2 and 3 are shown in Figure 1.

5.3 Diurnal variation of wind speed

Two-hour averaged vertical profiles of wind speeds for the entire period of observation is shown in Figure 24. As it can be observed from Figure 24, diurnal variations are prominent at this site (during the observation period). Higher gradients of wind speed are observed during night time and more neutral conditions are observed in the middle of the day. During day-time, the average wind speed increase, for 60 m height difference, is less than 0.5 ms^{-1} . While during night-time, average wind speeds are observed to change from 10 ms^{-1} to 12.5 ms^{-1} for the same height difference. Figure 24

shows that a small change in turbine hub height at the site could result in significant net increase or decrease of power production.

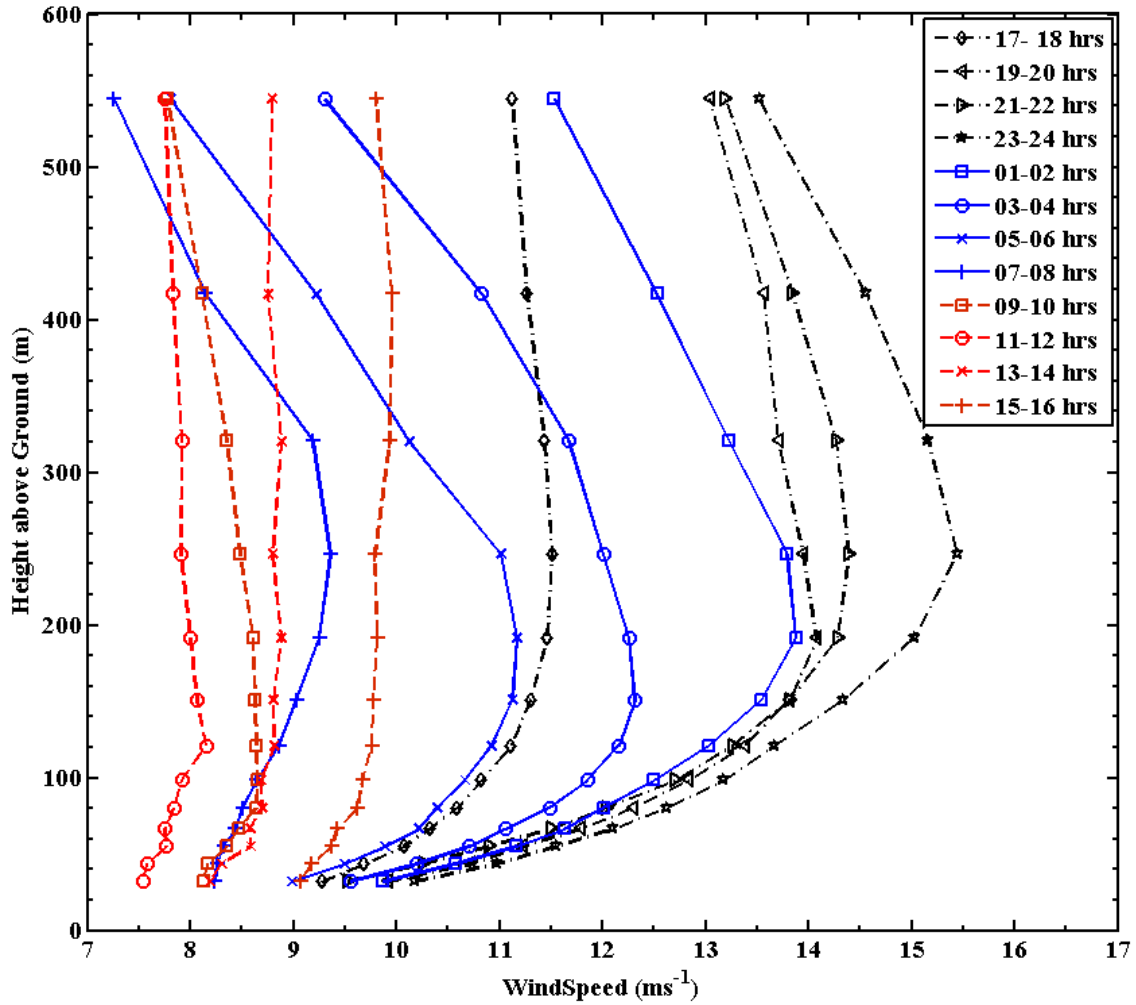


Figure 24. Monthly two-hour averaged vertical profiles of wind speed for 24-hours (data collected 3km north of the site) showing strong diurnal variations from lidar measurements. The legend displays local times.

5.4 Wind power production

The wind resource or wind power production for a particular site can be estimated based on wind speed distribution for the given area. As shown in the previous section,

the distribution of winds over the entire site has been measured. The wind power production for a specific turbine site can be calculated using the *average wind machine power*, given by Equation 14 below (Manwell et al. 2009).

$$\bar{P}_w = \frac{1}{N} \sum_{j=1}^{N_B} P_w(m_j) f_j \quad (14)$$

where,

N_B – No. of bins used in the distribution,

m_j – Midpoints of each of those bins,

f_i – Number of occurrences in each bin or frequency, such that

$$N = \sum_{j=1}^{N_B} f_j$$

$P_w(U)$ – The power output defined by the particular wind machine power curve at velocity U .

The total energy output is calculated at every location at hub height based on the distribution of wind speed and the power curve (assuming a standard 80 m hub 2.1 MW wind turbine power curve). Figure 25 shows the average machine power on a terrain-following surface at hub height. It should be noted that the errors normally associated with scaling the wind speed distribution from the meteorological tower by a linear factor calculated by a wind flow model (such as WAsP), or using Weibull, Rayleigh distribution etc., are avoided, therefore providing an estimate of the wind power density based purely on measurements (Manwell et al. 2009).

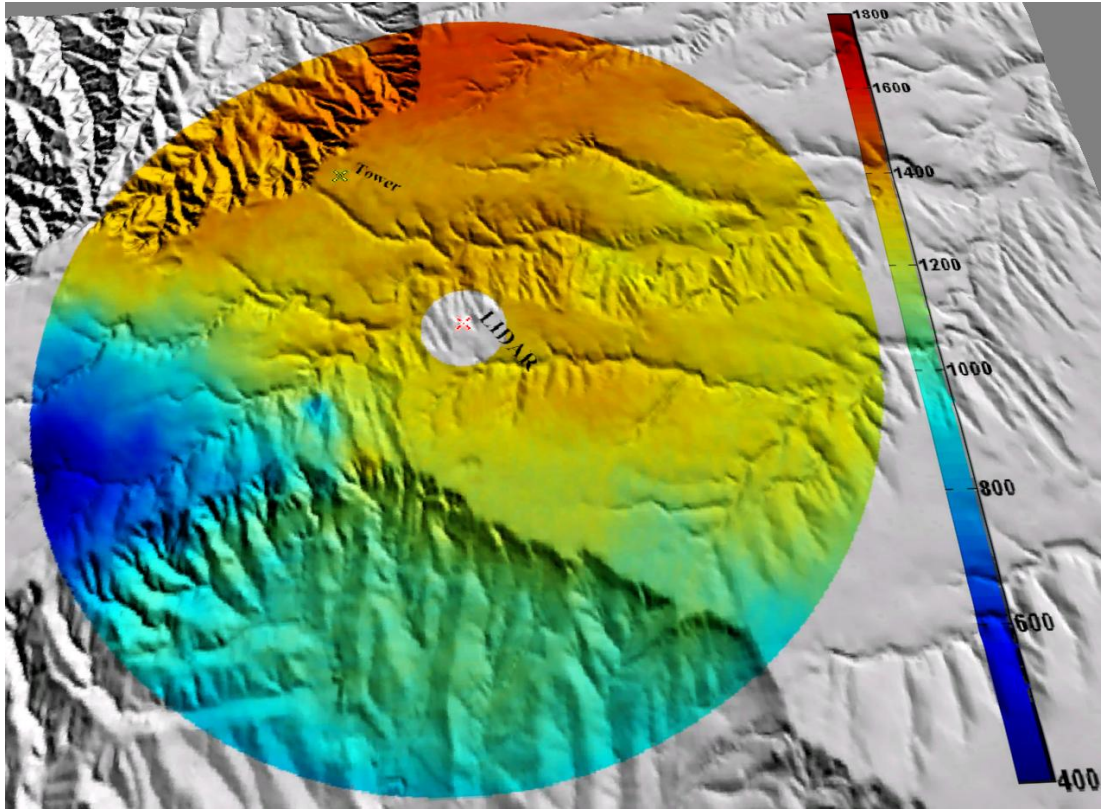


Figure 25. Lidar terrain-following machine power production at 80 m hub height. The colour bar represents the power in kW.

5.5 Wind farm layout design

An example placement of wind turbines based on machine power density subject to the distance constraints (for 75 wind turbines) is shown in Figure 26. Once the turbines locations were found, a simple topology gradient algorithm was run to pick the highest terrain location within 200 m of each turbine. The turbines are shifted to the new location, approximately maintaining the distance constraint. Such a product could provide an initial estimate for total yield produced by the wind farm or an input to global optimization algorithms, if the observational time were made suitably long, or long term meteorological adjustments were made based on a correlation with a reference station.

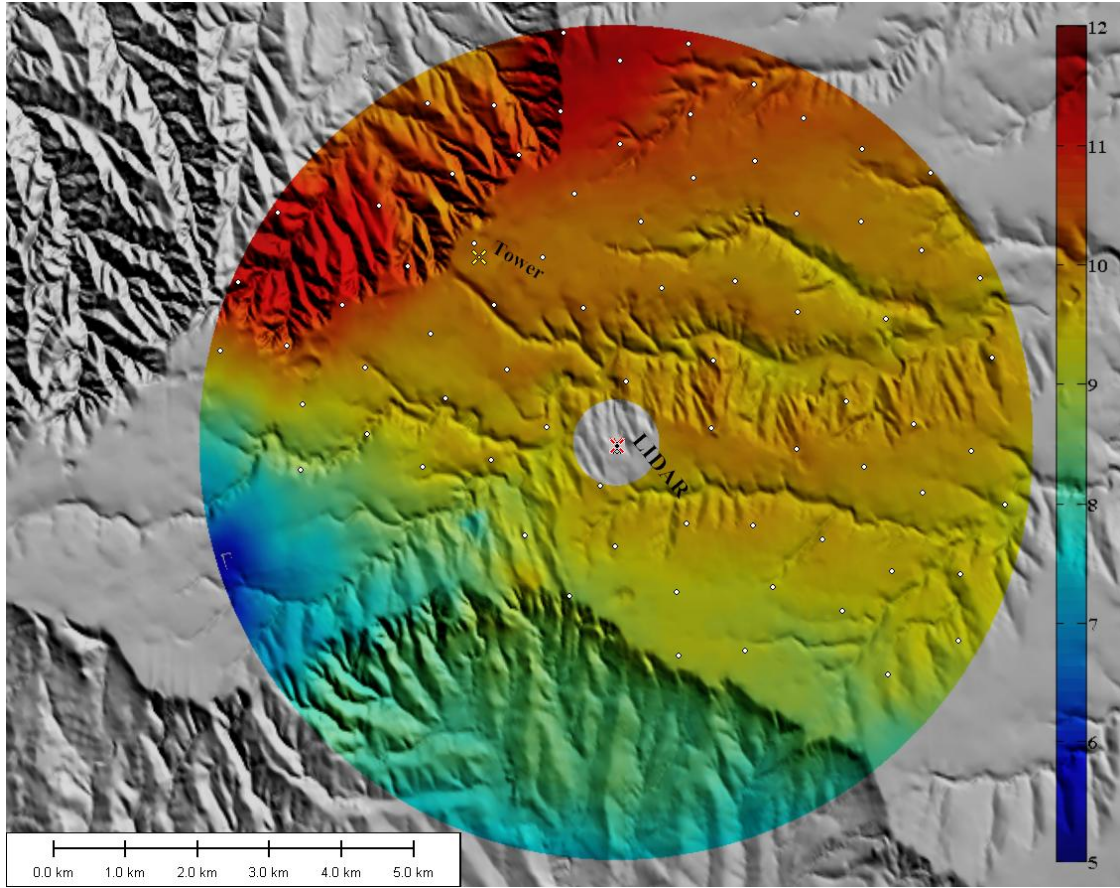


Figure 26. Locations of wind turbines (75), based on simple algorithm, overlaid over averaged wind map. The white circular dots represent locations of wind turbines based on the algorithm. The color bar shows wind speed in ms^{-1} at 80 m hub height.

Figure 27 provides optimized wind farm layout (25 wind turbines) based on genetic algorithms. Several constraints are applied to the optimized layout. A minimum turbine spacing of 7D (i.e. 7 times the rotor diameter), wind turbine wake interaction effects are included (a simple park model), measurement domain of approximately 12 km is used, lidar wind speed estimates are transformed into a rectangular grid. The objective function is to maximize energy capture. A 2MW wind turbine at 80m hub height is used in this optimization process. For the mathematical approach, please refer to Kusiak et al. 2010.

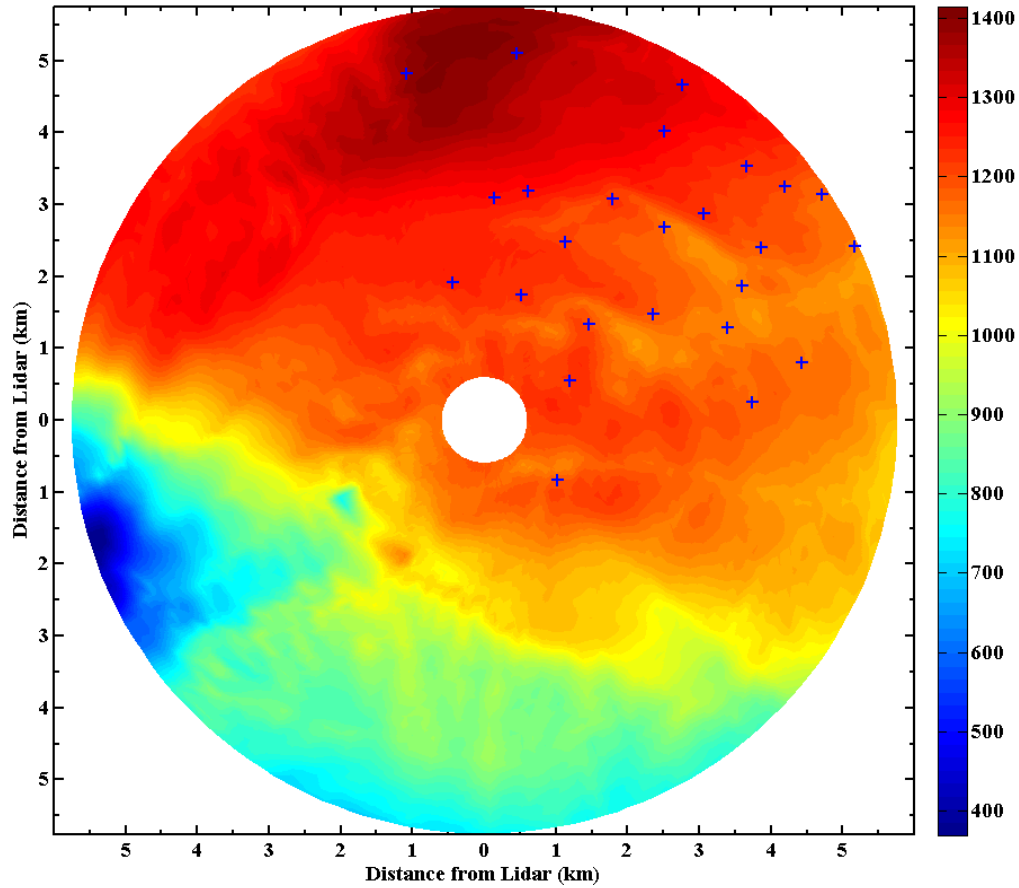


Figure 27. Optimized layout (25 turbines) based on Genetic Algorithms overlaid over power production map. The + symbols represent optimized turbine locations. A minimum separation of 7D was used in this analysis. Wind turbine wake interaction effects (Kusiak et al. 2010) were also included for optimal energy and cost output.

5.6 Wind farm wake analysis

Wake interaction effects of the 5 wind turbines at site 2 were analyzed using a simple park model. Wake deficits from all the 5 turbines and their interactions were estimated and compared to lidar estimates. Figure 28 shows lidar wind speed measurements near site 2 along the mean wind direction and park model estimates based on initial wind speed inputs from lidar. Wake deficits estimates from several decay constants (k) were compared with lidar data. A decay constant of 0.09 approximates the

wake velocities reasonably well up to 2 km downwind of the wind farm. Further comparison of different wake models, based on different times of the day, needs to be analyzed and is a scope of future work.

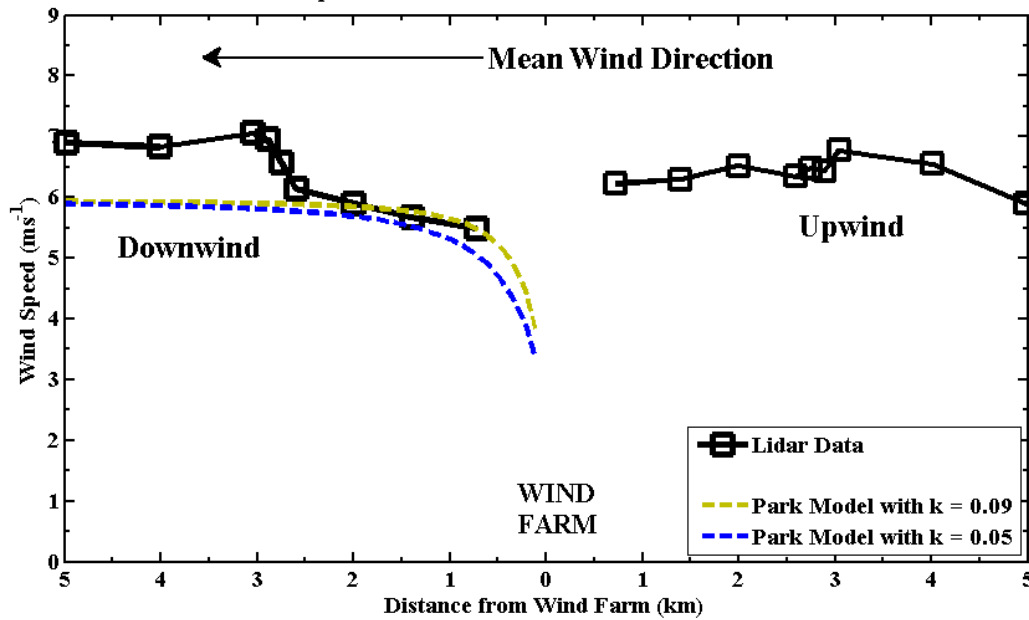


Figure 28. Cumulative wind farm wake deficit measured by lidar at site 2. Park model with turbine wake interaction effects for several decay constants is also shown. A decay constant of 0.09, seems to approximate the wind speeds reasonably well.

5.7 Layered approach

To estimate the power output from a turbine, it is a general practice to assume that the mean wind speed at hub height is representative of the wind over the whole swept area. Since greater wind speeds and shear are often observed at the higher elevations associated with the largest wind turbines, there may be significant differences in wind speed within the rotor-swept area. If these variations in the wind profile (and their associated extractable energy) are not well represented by a single measured value at

hub-height, significant errors could be introduced into estimates of power production. Therefore, since the measured lidar data presents the opportunity to analyze winds at a variety of vertical levels within the rotor swept area, an analysis using multiple vertical layers is explored below. The approach of Wagner *et al.* 2009 is followed, where terrain-following average wind power is estimated using Equation 15 at various vertical levels within the swept rotor area. The combined wind power from all the layers is estimated by Equation 16:

$$\bar{P}_{wl} = \frac{1}{2} \rho \bar{U}^3 \quad (15)$$

$$\bar{P}_{wc} = \frac{1}{2} \rho \sum_i \bar{U}_i^3 \frac{A_i}{A} \quad (16)$$

where,

\bar{P}_{wl} = wind power density at each layer,

\bar{P}_{wc} = combined wind power density from all layers,

ρ = density of air (1.225 kg/m³),

A = total area of the rotor,

A_i = area of winds covered by each layer ($i = 1, 2$ and 3) = $A/3$,

\bar{U} = average 10 min wind speed estimates at different vertical levels.

In this study, three layers (50, 80 and 110 m AGL) were chosen and the area covered by each layer was equally divided. Figure 29 shows the available wind power density estimated at the three individual layers and combined wind power density (all three layers together.) As observed in Figure 29, the power density changes significantly among the layers as well as the combined approach. Table 8 below shows the ratio of the

mean wind power density estimated at different layers (50 m, 110 m and combined) by the wind power density at hub height. The mean wind power for the entire layer (terrain-following wind map) estimated at hub height (80 m) is under-predicted by 0.05 % compared to the combined layer wind power. Although the wind power difference between the layers is small in this case, the potential to measure the expected energy through the entire layer has been demonstrated. However, the wind power which would be extracted at the chosen turbine locations (from Section above) at hub height is underestimated by 0.49 % compared to the estimated combined layer wind power at the turbine locations. Therefore, predicting the wind power based solely on the mean winds at hub height for a wind farm may include a degree of error associated with insufficient representation of wind profile variations in the vertical. Increasing the number of layers would most likely provide a more realistic estimate of the total wind power potential of this site. Although, larger vertical interpolation is performed at farther range-gates, due to diverging lidar beams.

Table 8. Percent change in wind power density estimates at various layers with respect to hub height at Site 2

Layer Height AGL (m)	Change in mean power density with respect to 80 m hub height (%) ^a
50	-16.42 (↓)
110	16.59 (↑)
Combined ^b	0.054 (↑)

^a Based on wind power density at 80 m hub height

^b Combined – Total wind power estimated based on all three layers together

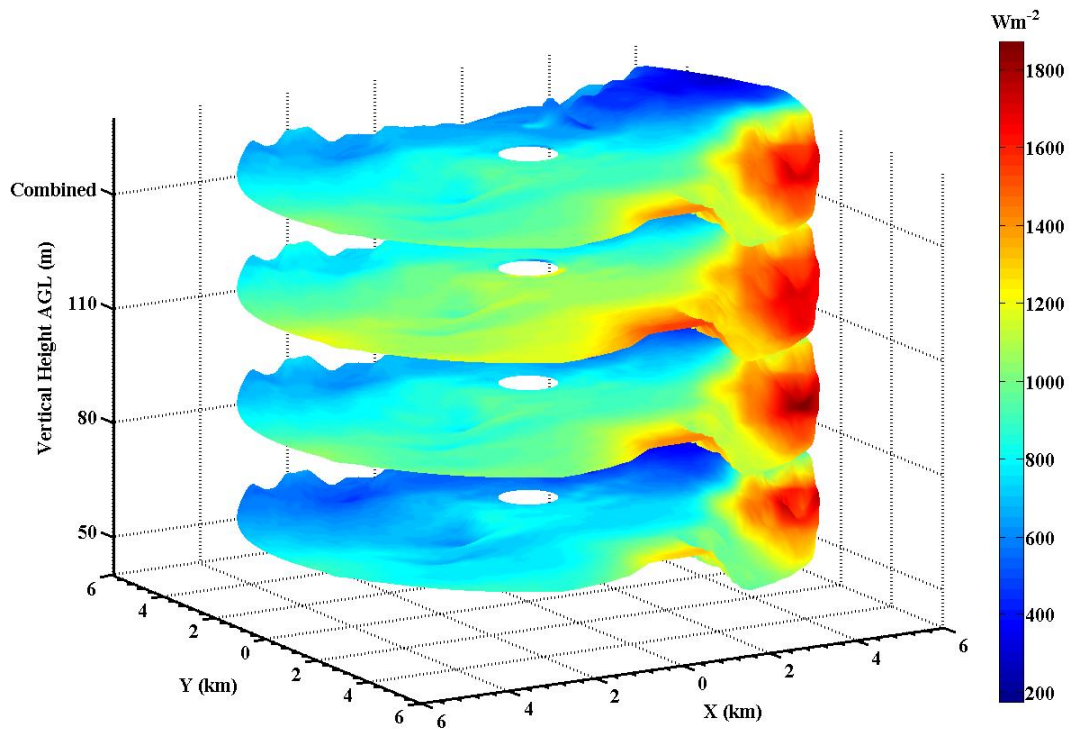


Figure 29. Terrain-following wind power density estimates at various heights of the rotor swept area. The “combined” wind power density estimated from all the three layers is also shown. Where X (km) and Y (km) is the distance from lidar in the respective directions.

6 MESOSCALE MODEL FORECAST COMPARISON

Wind speed, direction and power estimates from both measurement (lidar and tower) were compared to COAMPS estimates. Since detailed spatial comparison between measurement and COAMPS estimate would be tedious, certain locations were picked as shown in Figure 30 and analysis is provided. The mean wind field estimated by COAMPS for the period of observation is shown in Figure 31.

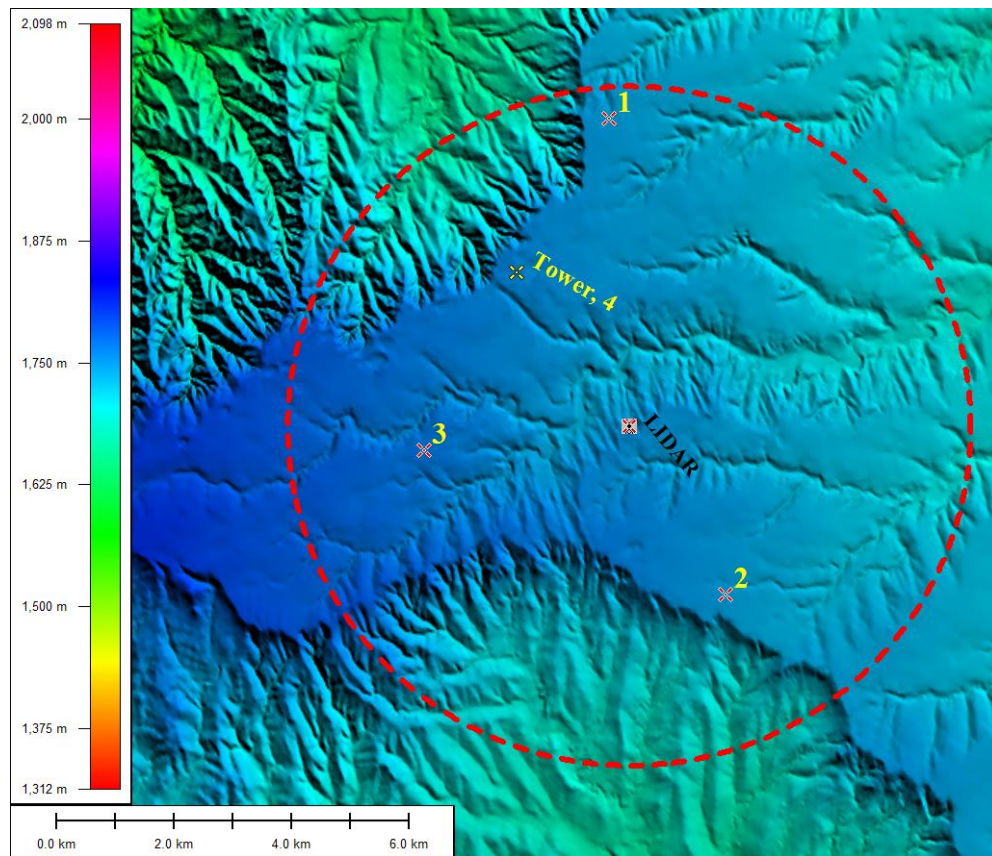


Figure 30. Terrain of the site with lidar scan overlaid. Four locations (x) shown were used to compare distributions between lidar and COAMPS. Tower is located at location 4. Color bar represents terrain height.

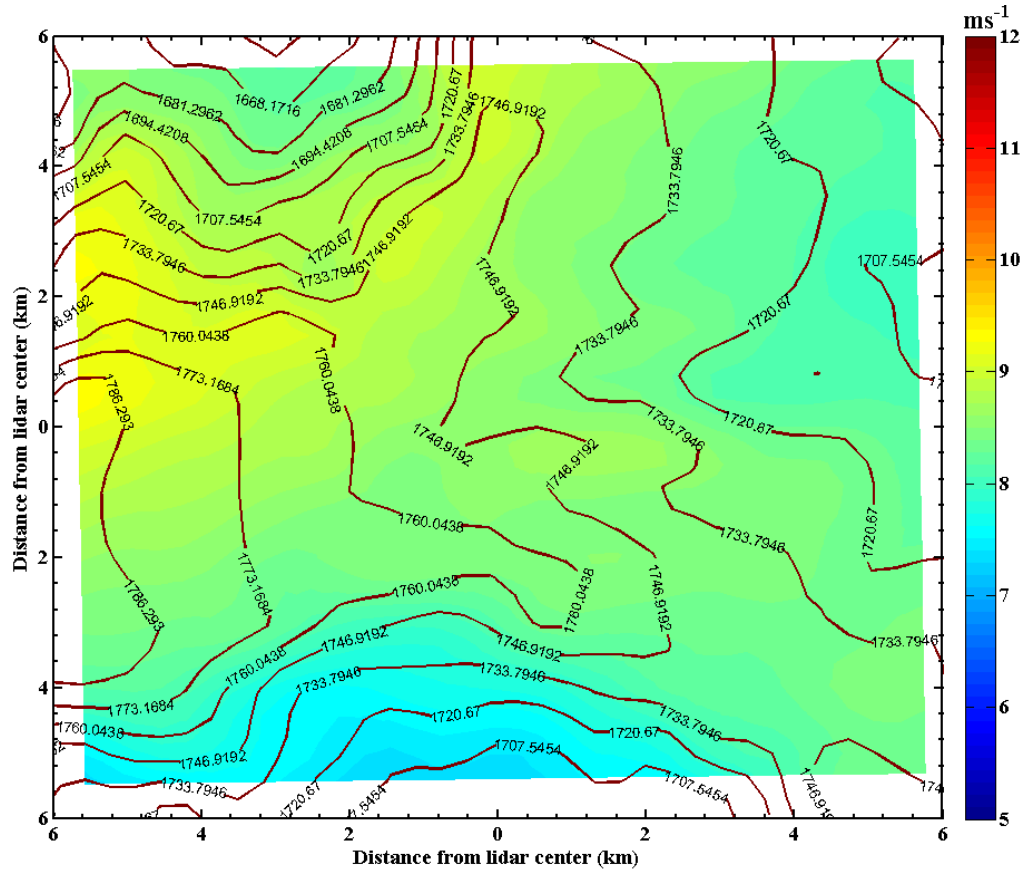


Figure 31. COAMPS estimated wind speed for the period of observation at Site 2.

6.1 Tower, CDL and COAMPS inter-comparison

Lidar wind speed and direction on a terrain-following surface at 50 m have been compared to mast measurements and COAMPS simulation at 50 m for the period of observation (approximately one month). Lidar and tower measurements were averaged over 30 minutes for appropriate comparison with COAMPS simulation. Also lidar data points, within the COAMPS 333 m horizontal grid, are spatially averaged as shown in Figure 32. The 30 minute integrated mean wind speed and directions, standard deviations and root mean square (RMS) difference between tower, lidar and COAMPS forecasts are presented in Table 9 and Table 10, respectively. These statistics were

estimated at the location of the tower. Time periods when lidar data was unavailable (due to lower aerosol content in the atmosphere, rain etc.,) are not included in the analysis. The 30 minute RMS wind speed between the tower/lidar and COAMPS forecasts was approximately 3.2 ms^{-1} . With increasing averaging time the RMS difference does not reduce considerably, as observed between tower and lidar (Krishnamurthy et al. 2012). The time series plots comparing wind speed and direction from lidar, tower and COAMPS are shown in Figure 33. Reasonable agreement was observed between observations and COAMPS forecasted direction. Wind rose comparison between lidar and simulation near the tower location is shown in Figure 34. Although the mean wind direction is forecasted reasonably well (as seen in Figure 34), wind intensities within each directional sector showed large discrepancies. Lidar and COAMPS wind speed and direction scatter plots are shown in Figure 35. Wind speed correlation of 40% and direction correlation of 22% is observed. Simulations consistently under-predicted wind speed estimates and did not capture abrupt wind direction changes, this is evident from Figure 34 and Figure 35B. This discrepancy can be due to several reasons for example, improper surface and soil-layer physics models, boundary layer turbulence parameterization schemes, sensitivity of horizontal grid resolution (333 m) on low-level winds etc. Therefore, this again provides evidence that every mesoscale models needs to be adjusted to site conditions and a standard mesoscale model does not provide accurate forecasts for wind farm assessment.

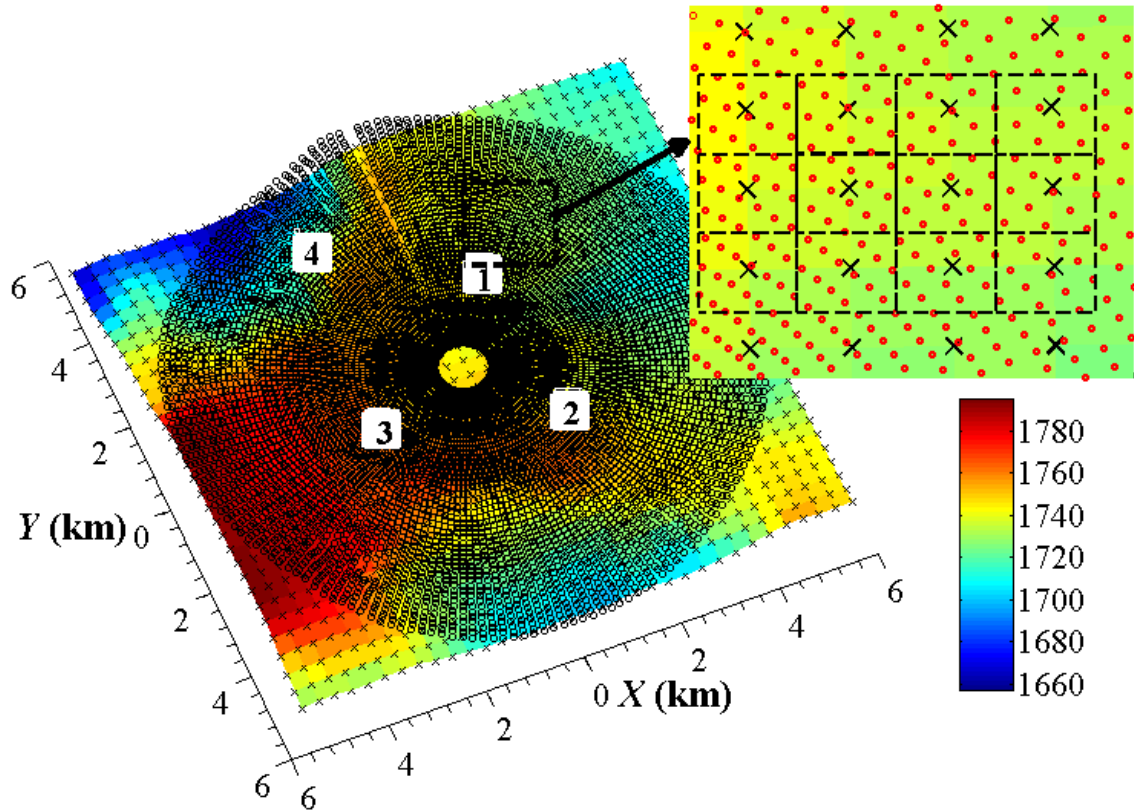


Figure 32. COAMPS rectangular grid (x) and Lidar Polar grid (o) overlaid over terrain. The sub-figure shows the points averaged from lidar estimate for appropriate comparison with COAMPS data. Each dotted box shown in the sub-figure represents COAMPS grid cell of 333 m. Four locations (square boxes with white background) on the terrain were chosen for further analysis. The color bar represents the terrain height in meters. X and Y represent distances from lidar location.

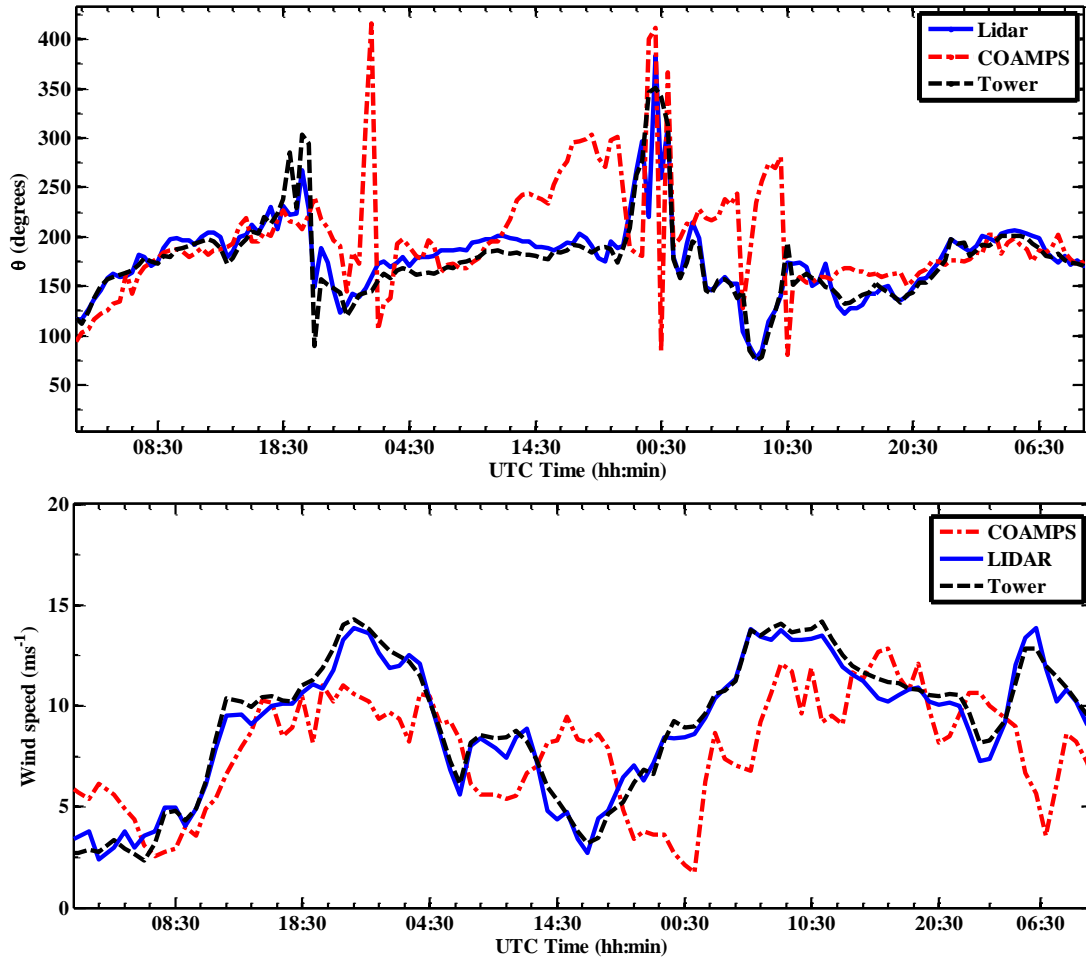


Figure 33. A) Lidar versus COAMPS direction comparison at 50 m for the period of observation. The gaps in lidar series show time periods when measurement with very low signal-to-noise ratio was observed. B) Wind speed comparison between COAMPS, lidar and tower simulation at 50 m. The gaps in lidar series show time periods when measurement with very low signal-to-noise ratio was observed.

Table 9. Tower, Lidar and COAMPS wind speed statistics over the period of observation at 50 m (AGL) at Site 2

Instrument/ Simulation	Mean (ms ⁻¹)	Standard Deviation (ms ⁻¹)	30 minute RMS Difference between COAMPS (ms ⁻¹)
Tower	9.67	3.60	3.27
Lidar	9.61	3.61	3.23
COAMPS	7.78	3.20	--

Table 10. Tower, Lidar and COAMPS direction statistics over the period of observation at 50 m (AGL) at Site 2

Instrument/ Simulation	Mean (deg) ^a	Standard Deviation (deg) ^a	30 minute RMS Difference between COAMPS (deg) ^a
Tower	168.24	36.94	17.14
Lidar	170.34	37.01	16.99
COAMPS	180.51	46.71	--

^a Data utilized between 60-300 deg

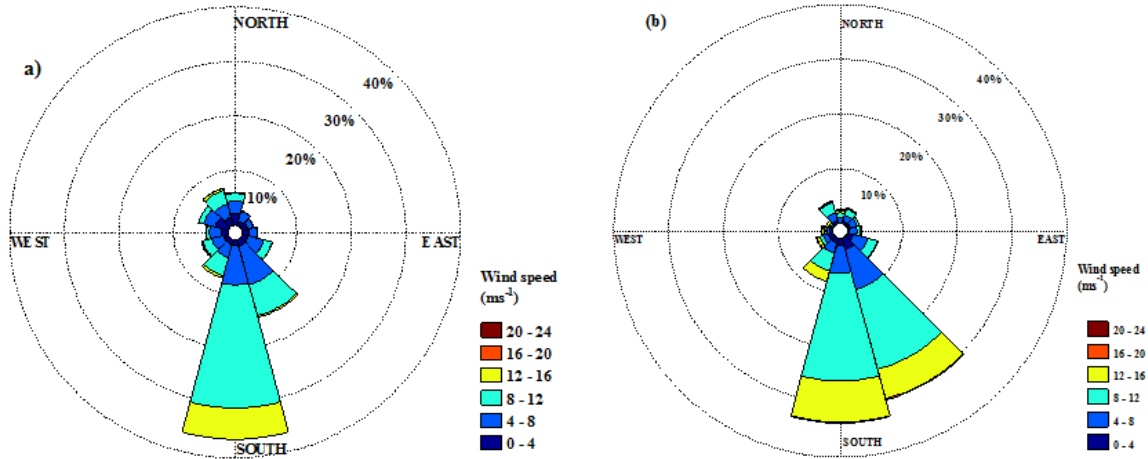


Figure 34. (a) COAMPS and (b) Lidar wind rose at 50 m. The color bar represents wind speeds in 4 ms^{-1} intervals and percentage of wind speed in each direction sector is provided on the dotted circles.

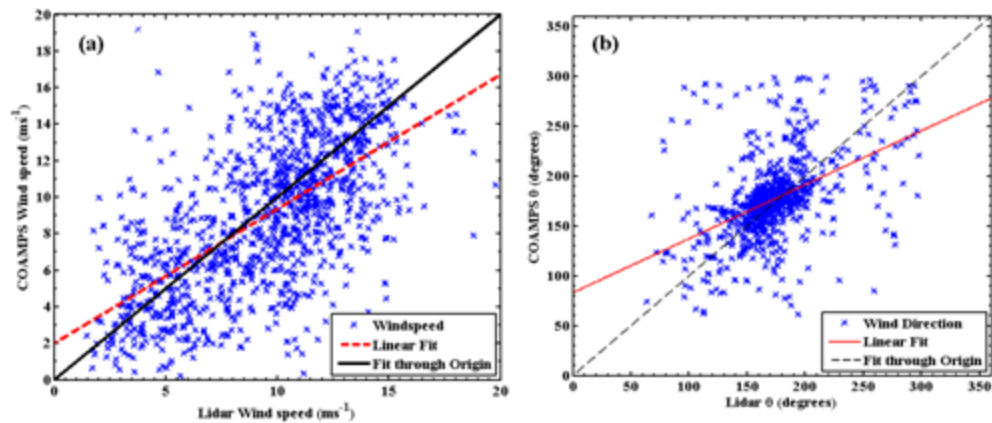


Figure 35. A) Wind speed scatter plot Lidar and COAMPS wind speed (30 minutes). Wind speed correlation of $\sim 40\%$ ($y = 0.74x + 2$) is observed between lidar measurements and COAMPS forecasts. Similar correlations are observed between tower and COAMPS forecasts. A total of 1296 values were used in the above plot. B) Direction scatter plot Lidar and COAMPS wind speed (30 minutes). Direction correlation of $\sim 22\%$ ($y = 0.54x + 83$) is observed between lidar measurements and COAMPS forecasts. Similar correlations are observed between tower and COAMPS forecasts. Data analyzed between 60 and 300 degrees. A total of 1,270 data points were used in this analysis.

6.2 Spatial wind speed and power production deviations

Understanding the spatial variability of wind speed across the domain of a wind farm is essential for wind farm developers. Terrain-following wind maps at hub height (say 90 m) can be generated by both COAMPS and lidar measurements. In this section, the difference in wind speed magnitudes between lidar and COAMPS is analyzed. A 2 MW wind turbine (90 m hub height) power curve was used for power calculations. Figure 36 and Figure 37 show monthly averaged spatial wind speed and normalized machine power difference between lidar and COAMPS over the period of observation, respectively. Machine power difference estimates are normalized by rated wind turbine power. Contour lines in Figure 36 and Figure 37 represent the orography over the wind farm area. Most of the wind farm domain exhibits a wind speed deficit (*i.e.*, Lidar – COAMPS) of $1\text{--}2\text{ ms}^{-1}$, therefore average COAMPS wind forecasts are reasonably in good agreement with lidar measurements. Maximum wind speed deficits of $\sim 3\text{ ms}^{-1}$ was observed near the north and north-west regions of the domain. As higher wind speeds are observed near the north western ridges, greater power fluctuations are also observed. Power deviations of greater than 30 %, at a single grid location, are estimated by COAMPS simulations. While near the western plateau, since lower wind speeds are observed (Figure 20), power differences are lesser. Therefore, spatial variations in wind speed and power estimates needs to be carefully evaluated for wind farm assessment. Scanning Doppler lidar can be used to estimate spatial variations in wind speeds and adjustments to mesoscale model predictions for that site can be suggested. Lidar would provide an ideal tool for analyzing the accuracy of various parameterization schemes within the boundary layer.

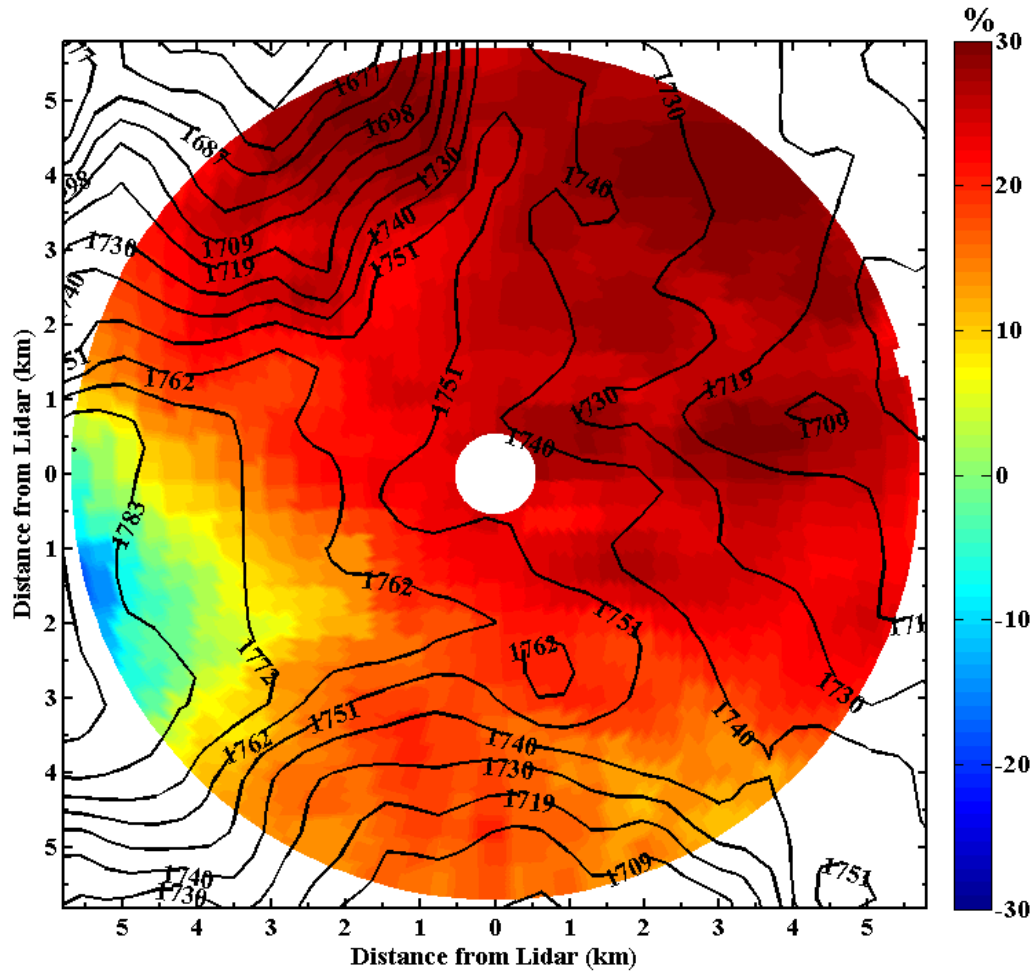


Figure 37. Normalized spatial map of mean machine power difference between lidar and COAMPS simulation for the period of observation (Lidar - COAMPS). The contour lines represent terrain height. (Normalized by turbine rated power)

6.3 Spatial wind distribution variations

The energy content of the wind depends not only on the mean wind speed but also on wind speed distribution. Wind speed distribution is a strong function of spatial position, especially for wind farms in or near complex terrain. Lidar and COAMPS are capable of providing wind speed distributions at every grid point over the entire spatial domain. The distribution of winds from COAMPS is compared to those measured from the tower and lidar. Since cup anemometers on the tower are located at a height of 50 m

(AGL), COAMPS and interpolated lidar data at 50 m were used for appropriate comparison. For time periods when lidar data was unavailable (due to low aerosol content), COAMPS and tower wind speed estimates were ignored. Figure 38 shows spatial wind distribution (for four spread out locations as shown in Figure 30, with location 4 being same as the tower) comparison between lidar, tower and COAMPS. Winds are binned into 30 sections, allowing estimation of a wind speed distribution. As observed in Figure 38, tower and lidar distributions compare reasonably well, while distributions from COAMPS, although follow the trend, are offset by approximately $1\text{-}2\text{ ms}^{-1}$ compared to lidar and tower observations. COAMPS under-predicts wind speeds in most areas of the wind farm and also over predicts the probability of low intensity winds. The bi-modal distribution observed in lidar data (Figure 38A) is not observed in COAMPS estimates. The power/energy estimated by each of these distributions would vary significantly. Since COAMPS forecasts only at two levels were available (50 and 90 m), the variation of distribution with height could not be analyzed.

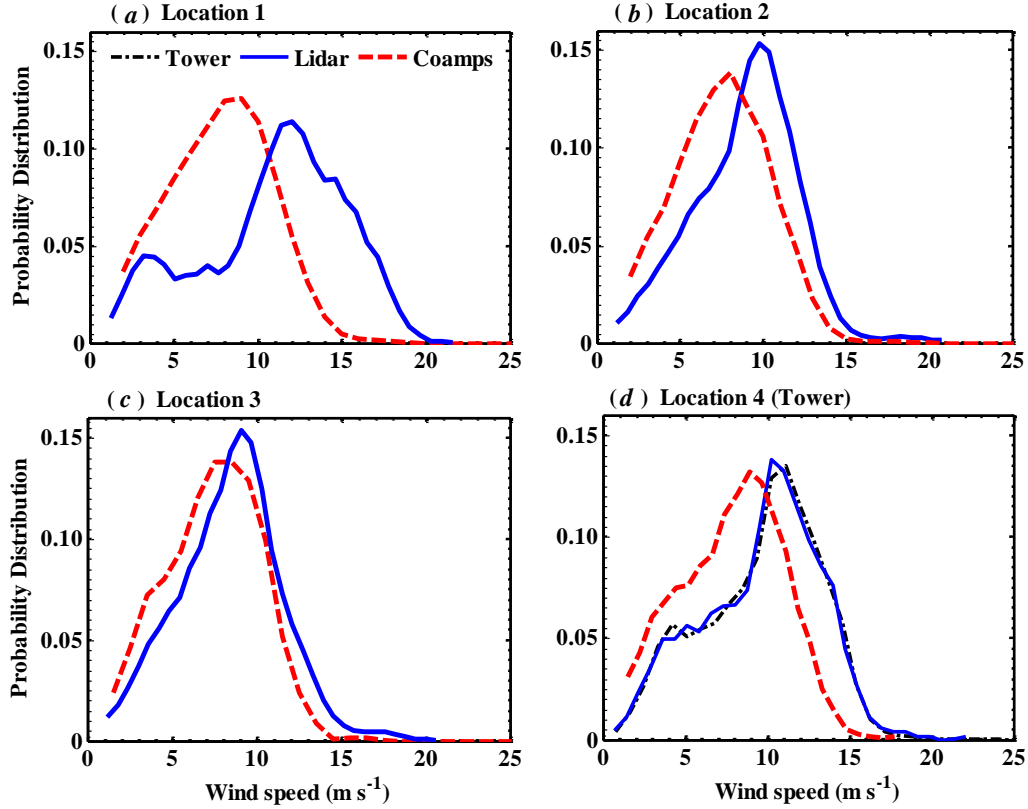


Figure 38. Wind speed distribution comparison between lidar and COAMPS simulation at all four locations shown in Figure 30. A) location 1, b) location 2, c) location 3 and d) location 4 on Figure 30.

6.4 Ramp events

It is critical that wind forecasts are accurate, especially during ramp events, when energy from a regional aggregate of wind farms can change by more than several MW in an hour. The need for accurate alerts for these type of events is increasing as more wind energy flows onto the power grid. Ultimately, anticipating these events an hour or two ahead will allow adding larger amounts of wind power to the grid. This arrangement can be challenging for grid operators. In many countries, wind farm operators bid power on the energy market for the day ahead, and have the possibility to correct their forecast up

to an hour before delivery. Consequently, bidders of wind power are interested in getting a reliable wind forecast. Improving wind forecasts is therefore important for both economic and technical reasons.

Ramps are defined as large increase or decrease of power within a short time period. Various definitions for ramps are provided in the literature (Kamath et al. 2009). In this paper, a ramp is defined as power fluctuation greater than 30 MW (increase or decrease of power) over a period of 1 hour for a hypothetical wind farm (75 wind turbines of 2MW each). The power fluctuation is chosen to be approximately 20% of the wind farm capacity (i.e. 20% of 150 MW wind farm). Table 11 shows total, daytime and nighttime ramp events estimated by lidar and COAMPS individually. As shown in Table 11, COAMPS forecasts almost 50% of total ramp events, 61% of daytime and 42% of night time ramp events. Although COAMPS predicted 50% of ramp events, only 12% of ramp events coincide at the same time as observed by lidar. Therefore, further care needs to be taken while evaluating ramp events from forecasted estimates. This could drastically affect the power forecast and could lead to grid imbalance or loss of energy. Figure 39 shows 4 wind farm power ramps as estimated by lidar and COAMPS, dotted boxes are placed around the time period of observed events. One out of the four ramp events shown is predicted very well by COAMPS (ramp event 1), while in most cases COAMPS does not forecast ramp events successfully. COAMPS predicts daytime events better compared to night time ramp events, this provides further validation that modern mesoscale models need improvements on stable boundary layer parameterization schemes. Although a few ramp events were forecasted by COAMPS, the magnitudes of power forecasted during these events deviated significantly from those measured by lidar

(not shown). Results of such analysis will be different depending on the location of the wind farm and possibly the amount of wind generation, improved forecasting or having a lidar near the wind site can none-the-less provide grid operators additional information they can use in balancing the load. Further detailed analysis is required to accurately quantify the loss due to ramp events.

Table 11. Ramp Statistics comparison between Lidar and COAMPS at Site 2

Ramp Events ^a	Total Events	Daytime Events ^b	Nighttime Events ^b	Common Ramp Events ^c
Lidar	113	62	51	14
COAMPS	57	26	31	

^a Power fluctuations of greater than 30MW in one hour is considered a ramp

^b Daytime events occur between 6AM to 6PM, while night time events occurs otherwise.

^c Ramp events observed within an hour of each other between lidar and COAMPS. Eight (8) out of 14 of the common ramp events were observed during day time. Magnitudes of ramp events not evaluated.

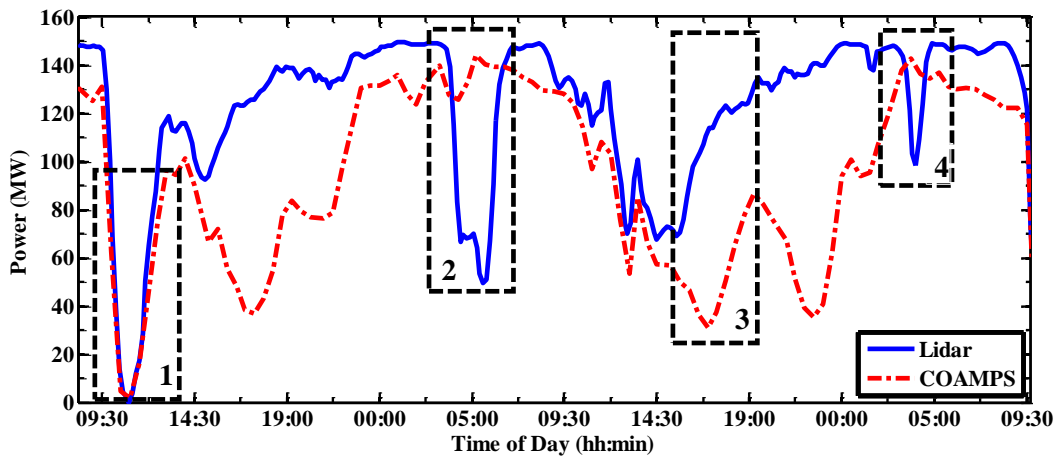


Figure 39. Cumulative wind farm power (MW) comparison between lidar measured and COAMPS forecasts. The dotted rectangular boxes show various ramp events observed by lidar.

6.5 Stability (α) variation across the domain

The stability of a field is measured based on shear exponent (α) from power law. Since lidar can measure winds at various vertical levels over the entire domain, shear exponents can be calculated at every grid point as shown in Equation 17 below.

$$\alpha_{ij} = \frac{\ln \frac{U_{ij1}}{U_{ij2}}}{\ln \frac{Z_{ij1}}{Z_{ij2}}} \quad (17)$$

Where i and j symbolize the grid location, while 1 and 2 represent the two vertical levels (50 and 90 m).

Shear exponent is a local stability parameter and cannot be assumed identical over the entire area of observation (Krishnamurthy *et al.* 2012). Both lidar and mesoscale models can measure winds at various vertical levels across the entire wind farm. Therefore, shear exponents from both lidar and COAMPS for the entire field of study were compared. Figure 40 shows one hour averaged shear exponents from both lidar and COAMPS forecasts for a stable boundary layer (i.e. positive shear exponent). One hour averaged shear exponents from both lidar and COAMPS compare reasonably well in most locations for this case, but the local stability variations is prominent in lidar observations. COAMPS almost provides a single shear exponent over the entire field, while lidar preserves local information. For example in Figure 40, lidar shows neutral to stable conditions north of the lidar location, while COAMPS estimates stable wind conditions throughout the domain. Further research is warranted for analyzing different stability classes and analyzing reasons for variations across the domain.

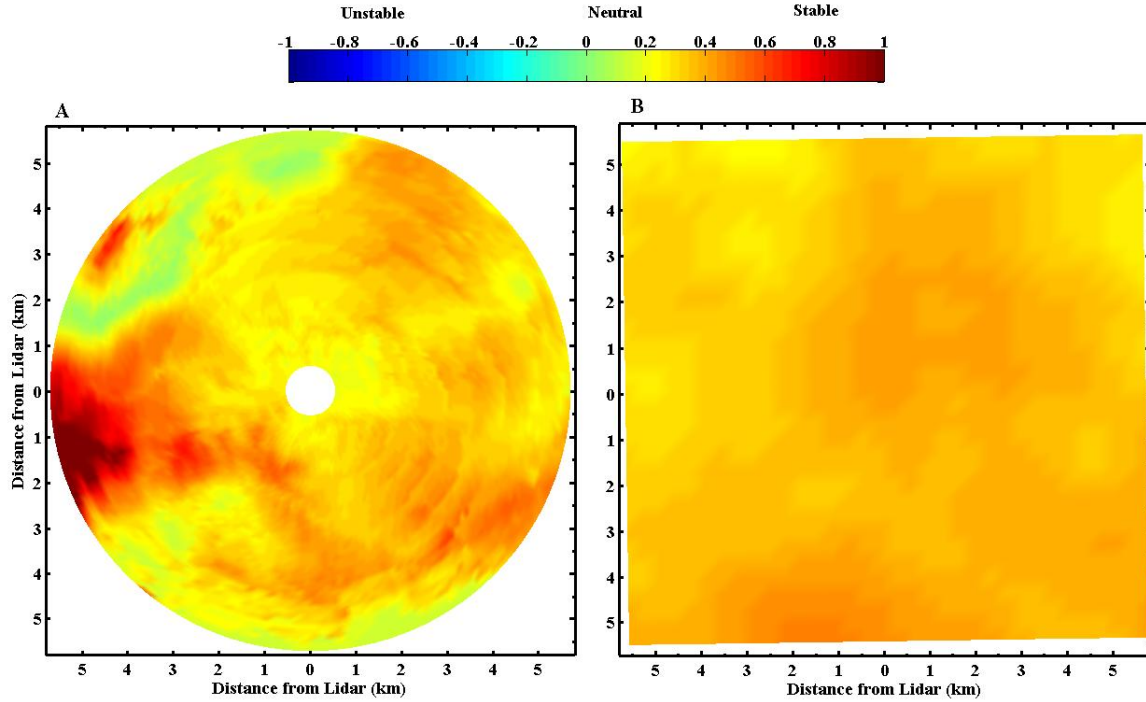


Figure 40. A) One hour averaged stability parameter (power law exponent $-\alpha$) calculated by lidar on June 17, 2007. B) One hour averaged stability parameter (α) calculated based on COAMPS simulations on June 17, 2007.

6.6 Diurnal variation effects on wind, direction and power estimates

Previous studies have indicated that mesoscale models under- perform during stable boundary layer conditions (Zhang et al. 2004, Shaw et al. 2008). Therefore, in this study the spatial difference in diurnal wind speed, direction and power between tower, lidar and COAMPS were analyzed. Figure 41 shows hourly averaged wind speed difference (observation wind speed minus COAMPS wind speed) between tower, lidar and COAMPS forecasts at location 4 on Figure 30 (tower location) at 50 m. It can be observed that an average wind speed difference of ~ 0.5 to 3 ms^{-1} is observed across various periods of the day. Smallest wind speed difference of $\sim 0.5 \text{ ms}^{-1}$ occurs during early morning periods. A slight increase in wind speed difference is observed after

sunrise. This effect could be due to a lot of factors affecting the model cycle, for ex. a) the radiation model not being updated regularly, b) soil-layer physics not accounting for the land surface heating, c) improper turbulence parameterization schemes and d) cumulative effect from other physics parameterizations in the model. This needs further research by applying different physics models to COAMPS simulations and comparing them to lidar data. No distinct phase lag or time lag was observed in the COAMPS data sets. The standard deviation of wind speed difference is almost constant at about 2.5 ms^{-1} . Similarly, the direction diurnal difference is shown in Figure 42. Although abrupt changes in wind direction were not captured well by COAMPS, mean directions were generally within $\pm 15^\circ$ of the true wind directions. High standard deviations of approximately $30\text{-}40^\circ$ is observed throughout the day. The large deviations could be a result of spatial averaging of COAMPS estimates.

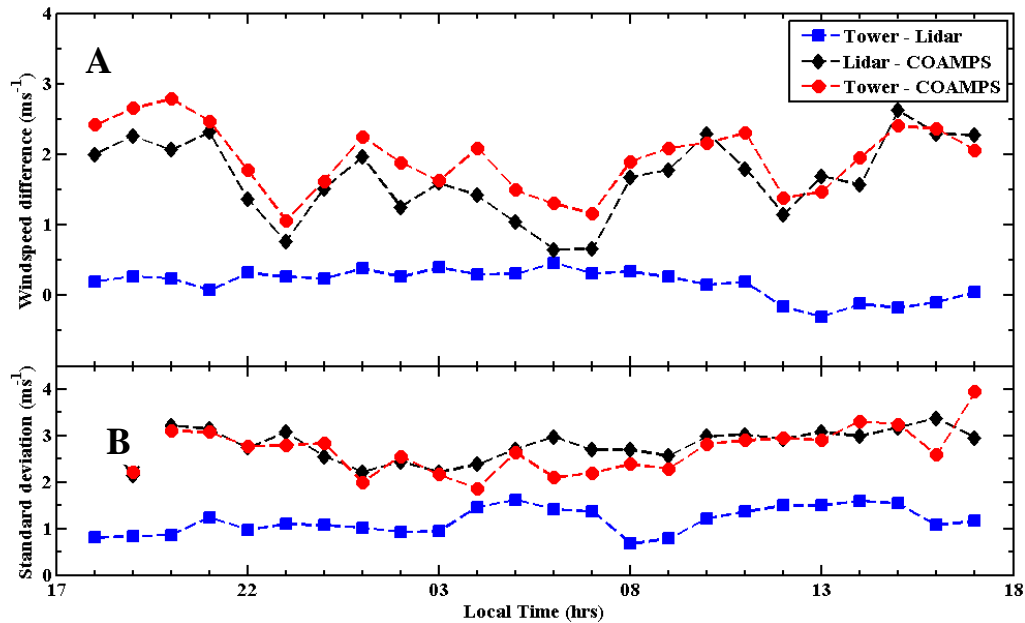


Figure 41: A) Hourly averaged diurnal variation of wind speed difference between tower, lidar and COAMPS at 50 m (Lidar – COAMPS). B) Standard deviations of wind speed difference between tower, lidar and COAMPS at 50 m.

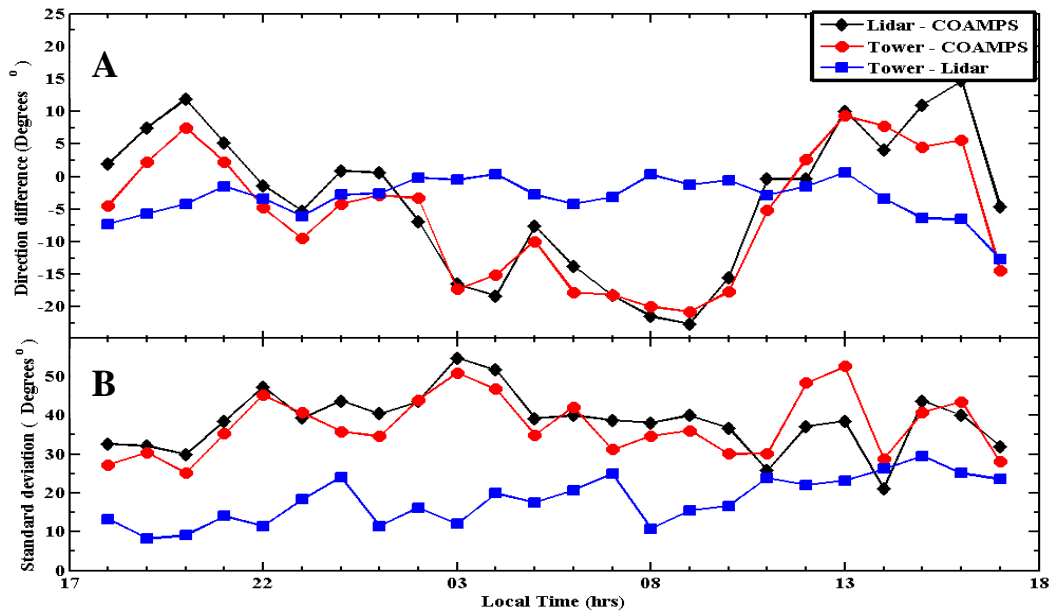


Figure 42: A) Hourly averaged diurnal variation of direction difference between tower, lidar and COAMPS at 50 m. B) Standard deviations of direction difference between tower, lidar and COAMPS at 50 m.

Since lidar can measure winds on a spatial domain, hourly averaged diurnal COAMPS forecasted winds and power at various locations on the site were compared to lidar measurements. Four locations were chosen, based on terrain variations in the region and also locations where power law was not used for estimating lidar winds on a terrain following surface. Figure 43A shows hourly averaged wind speed difference (Lidar - COAMPS wind speed) between lidar and COAMPS at all four locations for the period of observation. COAMPS under-predicts wind speed at most of the locations, while over-predicts wind speed west of the lidar location (*i.e.*, location 3). Maximum wind speed differences of $\sim 4 \text{ ms}^{-1}$ is observed during night time, while a constant wind speed difference of ~ 1.5 to 2 ms^{-1} is observed during day time. Wind speed differences at all locations converge to $\sim 1\text{-}2 \text{ ms}^{-1}$ during day time (*i.e.*, 0800 hrs to 1700 hrs), which

shows COAMPS predicts well during day time compared to night time flows. Another reason for improvement could be due to observation updates performed at 0800 hrs (based on optimal interpolation technique). Therefore, COAMPS shows reasonable accuracy during unstable daytime conditions, while during stable conditions (night time) the forecasts deviate significantly at certain locations from measurements. A constant standard deviation (~ 2 to 3 ms^{-1}) of wind speed difference is observed at all locations throughout the observation period (Figure 43B). As indicated previously, since high wind speeds are observed in this site during night time, a deviation of $2\text{-}3 \text{ ms}^{-1}$ in wind speed would result in substantial error in power forecast calculations. Figure 44 shows the hourly averaged normalized power difference between lidar and COAMPS forecasts at all four locations. Although large wind speed differences were observed during night time conditions, less power fluctuations are observed. The reason for the discrepancy is due to higher than rated wind speeds observed on this site. The rated wind speed of a typical wind turbine with hub height of 90 m is $\sim 13 - 14 \text{ ms}^{-1}$. Average night time wind speeds observed at 90 m on this site is greater $14 - 15 \text{ ms}^{-1}$ (refer Figure 24 above). Therefore a difference of 3 ms^{-1} in average wind speed would result in smaller power fluctuations compared to 2 ms^{-1} wind speed difference during day time (specific for the type of turbine used and site). During day time the wind speeds are most likely in the medium operating range (i.e., region 2 of the power curve) and therefore result in higher power deviations from measurements. Figure 44B shows hourly averaged standard deviation of power difference for the entire period of observation. Higher standard deviations in power are observed at location 3 (west of lidar), due to low average wind

speeds observed in this location. Further studies on effect of diurnal variations of wind velocity for power output estimation of a turbine are provided in Weisser et al. 2003.

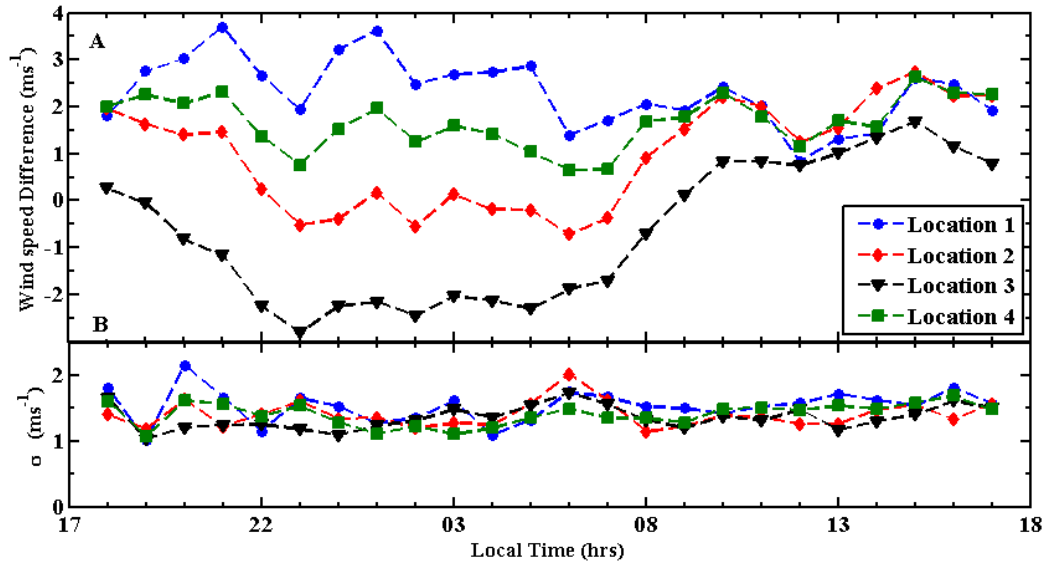


Figure 43: A) Hourly averaged mean wind speed difference between lidar and COAMPS simulation at different locations (shown in Figure 30) for the period of observation at 50 m (Lidar – COAMPS), B) Hourly standard deviation of wind speed difference for the period of observation at 50 m.

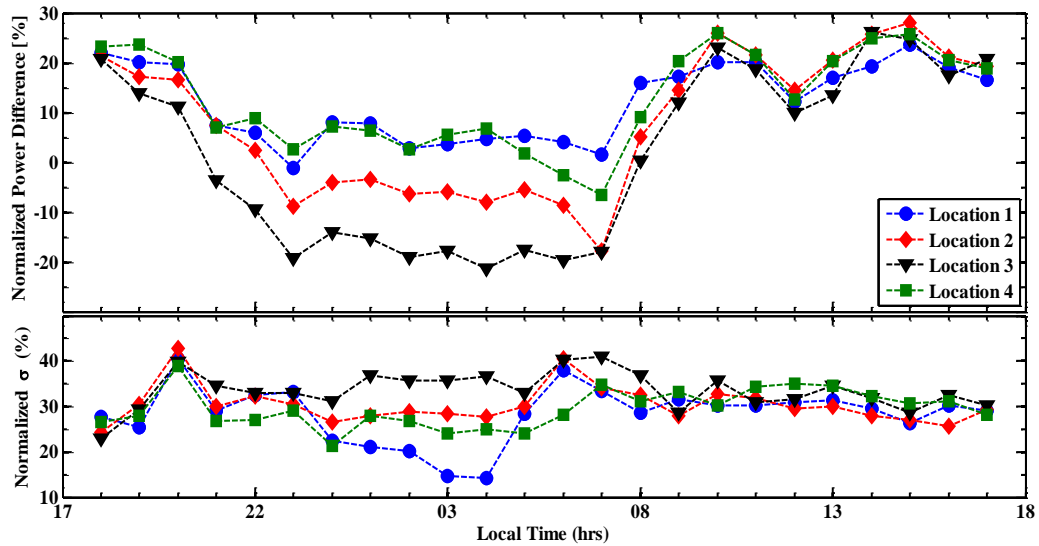


Figure 44: A) Hourly diurnal variation of average normalized machine power (kW) difference between lidar and COAMPS at 90 m (Lidar – COAMPS), at multiple locations shown in Figure 30. B) Hourly averaged standard deviations of normalized power (kW) difference between lidar and COAMPS for the period of observation at 90 m (normalized by wind turbine rated power).

6.7 Wind speed bias corrections

Since a constant bias ($1\text{-}2\text{ms}^{-1}$) was observed between measurements and simulation, a mean offset could be used to correct simulation results. Therefore, a bias, of 1.89ms^{-1} , estimated from tower measurements is added to COAMPS wind speed forecasts. COAMPS estimates after accounting for monthly biases are compared to lidar measurements. Table 12 shows RMS differences between tower, lidar and COAMPS estimates after bias corrections. The 30 minute RMS difference between tower/lidar and COAMPS estimates are reduced approximately by 0.4 ms^{-1} . Although the mean wind speed difference is reduced, the RMS difference is still significant (2.86 ms^{-1}). Figure 45 shows monthly averaged wind speed differences at hub height between COAMPS after bias correction and lidar measurements over the entire spatial domain. A significant improvement in COAMPS wind speed estimates was observed for most of the domain. At the tower location, wind speed differences between lidar and COAMPS estimates reduced by 70%, while machine power difference were reduced by 77%. The reason for the small discrepancy between lidar and COAMPS simulation, after bias removal, is due to spatial averaging of lidar measurements in comparison to tower measurements. Figure 46 shows monthly averaged machine power difference estimates between COAMPS (after bias removal) and lidar at hub height, normalized by wind turbine rated power. Reasonable improvement is observed for most of the wind farm domain. However, wind speed and machine power differences increased by the same near the western plateau (as seen in Figure 46). Since higher winds were estimated by COAMPS, compared to lidar measurements, near the western plateau (as shown in Figure 36), a positive bias correction increased the wind speed difference at these locations. Therefore, accounting

for bias at a single location would definitely improve the statistics if similar bias is observed throughout the domain (*i.e.*, in case of a flat terrain). In case of a complex terrain, several factors affect the wind speed estimates and assuming constant bias could worsen estimates at several other locations. Further research is required in accounting for spatial variation in wind field for bias corrections. Periodic mesoscale model observational updates with spatial information, such as assimilation with lidar data would improve wind farm assessment forecasts.

Table 12. Tower, Lidar and COAMPS (after bias correction) wind speed statistics over the period of observation at 50 m (AGL)

Instrument/ Simulation	Mean (m s ⁻¹)	Standard Deviation (m s ⁻¹)	30 minute RMS difference between COAMPS and tower/lidar (m s ⁻¹)
Tower	9.67	3.60	2.93
Lidar	9.61	3.61	2.86
COAMPS	9.67 ¹	3.20	--

¹ Mean wind speed same as tower, after bias correction (1.89 ms⁻¹)

mesoscale model updates with spatial information, such as lidar, for effective assessment of wind energy.

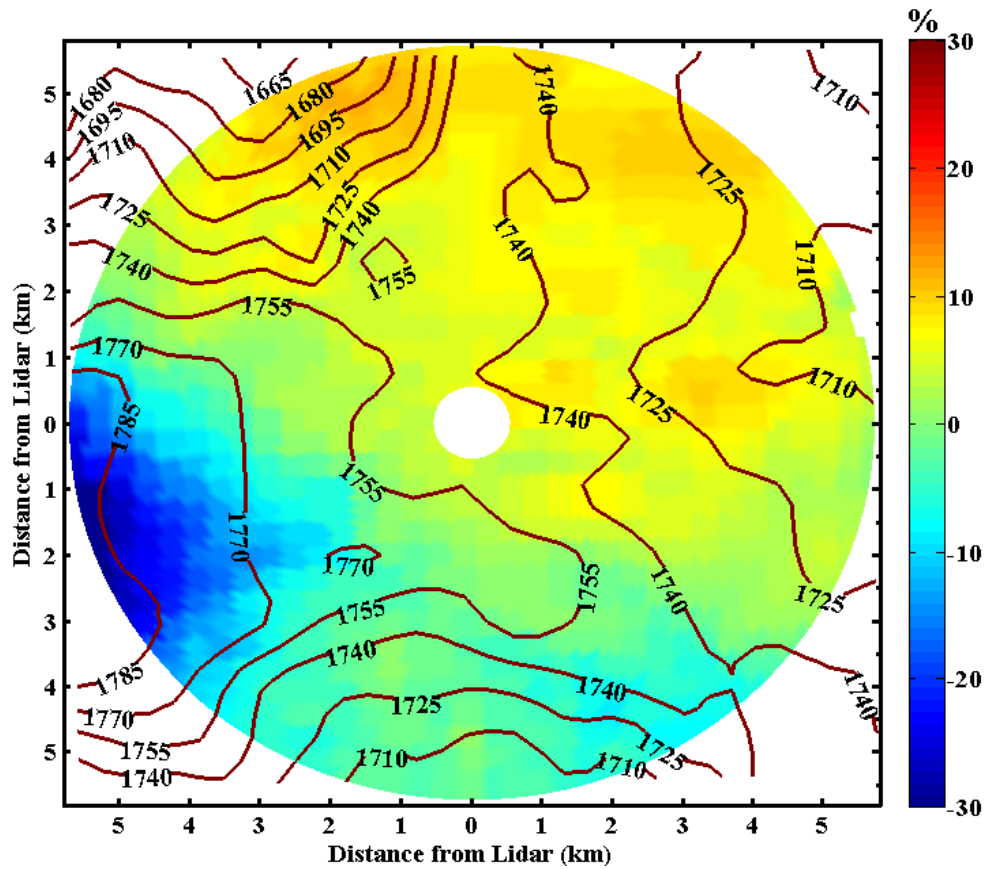


Figure 46. Spatial monthly averaged normalized power difference between Lidar and COAMPS Bias corrected estimates (Lidar-COMAPS). The contour lines represent terrain height and color bar shows normalized power difference (normalized by wind turbine rated power).

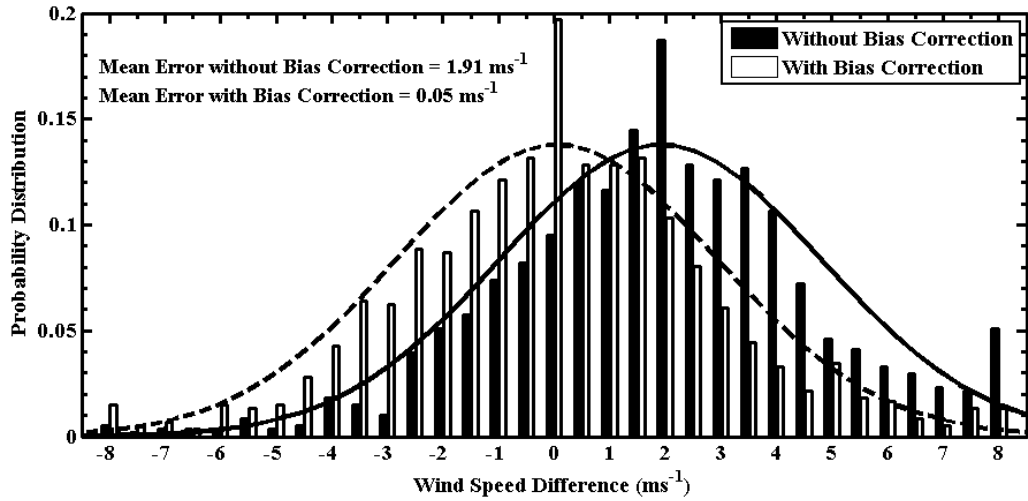


Figure 47. Distribution of 30 minute wind speed difference between Lidar and COAMPS (Lidar – COAMPS) with (no fill) and without bias (filled bars) correction at tower location. Normal distributions of both the distributions are also shown.

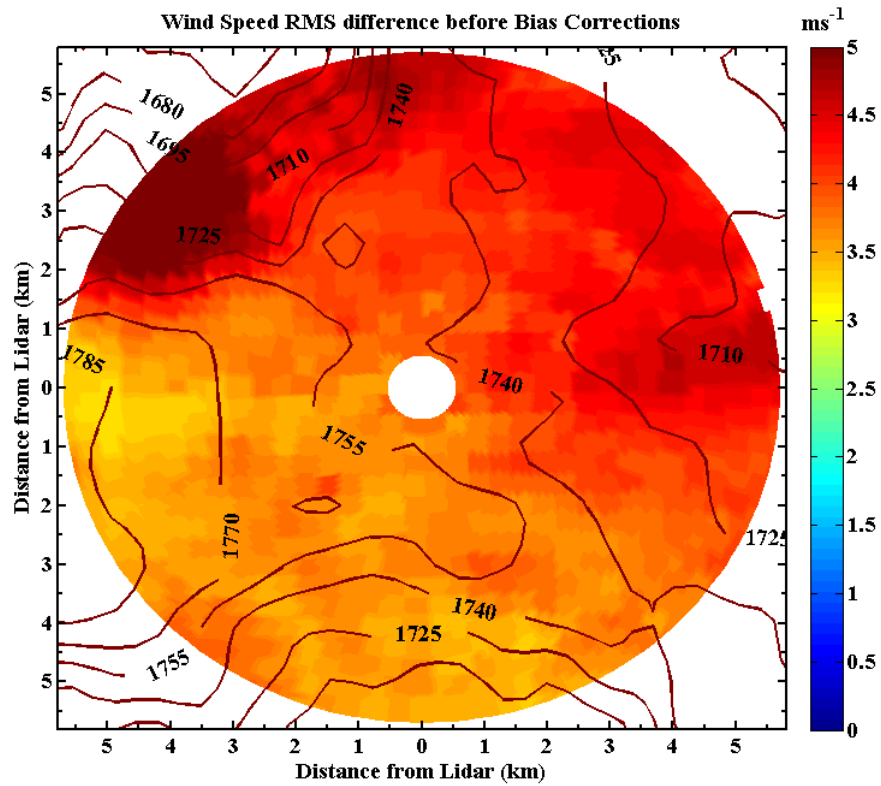


Figure 48. Spatial wind speed RMS difference between Lidar and COAMPS before Bias corrections.

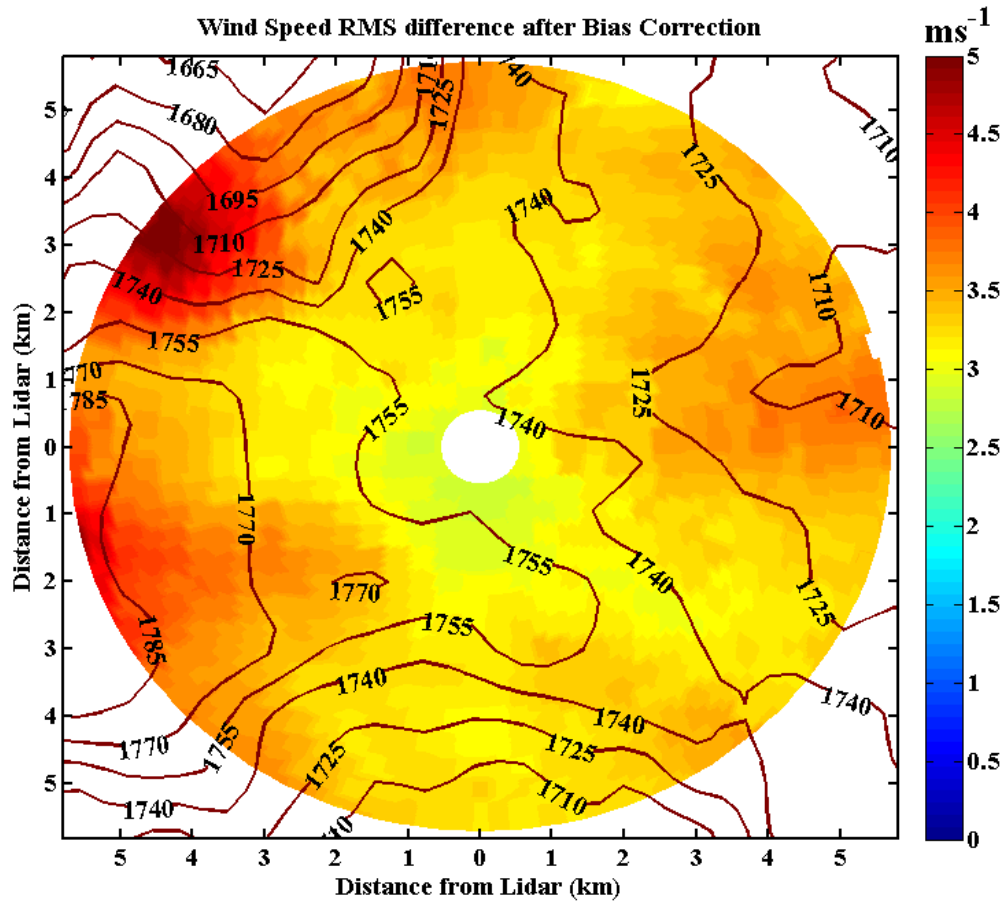


Figure 49. Spatial wind speed RMS difference between Lidar and COAMPS Bias corrected estimates.

7. VALUE PROPOSITION OF CDL FOR WIND FARM DEVELOPMENT

Since a single lidar measures radial winds, the data from two CDLs viewing from different directions can be combined to produce accurate horizontal velocity vectors over a wind farm domain. Dual-Doppler lidar scanning strategies are explored for wind resource assessment. Financial implications of conducting a climatological single and dual-Doppler study for a wind farm development are explored in this section.

The Annual Energy Production (AEP) is the quantity of energy delivered per year by a wind farm. A Wind Resource Assessment Program (WRAP) is designed to estimate the mean expected AEP (P50) and the uncertainty on the AEP (σ_{AEP}). These two decisive numbers drive the financing of the project. Since the initial investment for a wind farm is high, small deviations in uncertainty calculations can result in significant effect on project financing. Although the wind resource assessment constitutes to about 3% of the total project financing, it affects almost all the components of a wind farm development (see Figure 50 below). Several uncertainties are taken into account while financing a wind farm, for ex., climate variability, turbine control losses, turbine availability, wind profile, hub-height wind speeds, spatial variability, power curve, air density etc.. The WRAP enumerates a quantity of independent uncertainties which can strongly influence the global AEP of a wind farm. These uncertainties can be reduced by using commercially available remote sensing instruments (such as lidars and sodars) which can measure a larger section of the atmosphere to provide a better understanding of the atmospheric boundary layer. Remote sensing instruments can reduce several of these uncertainties, in providing an improved estimate of the AEP.

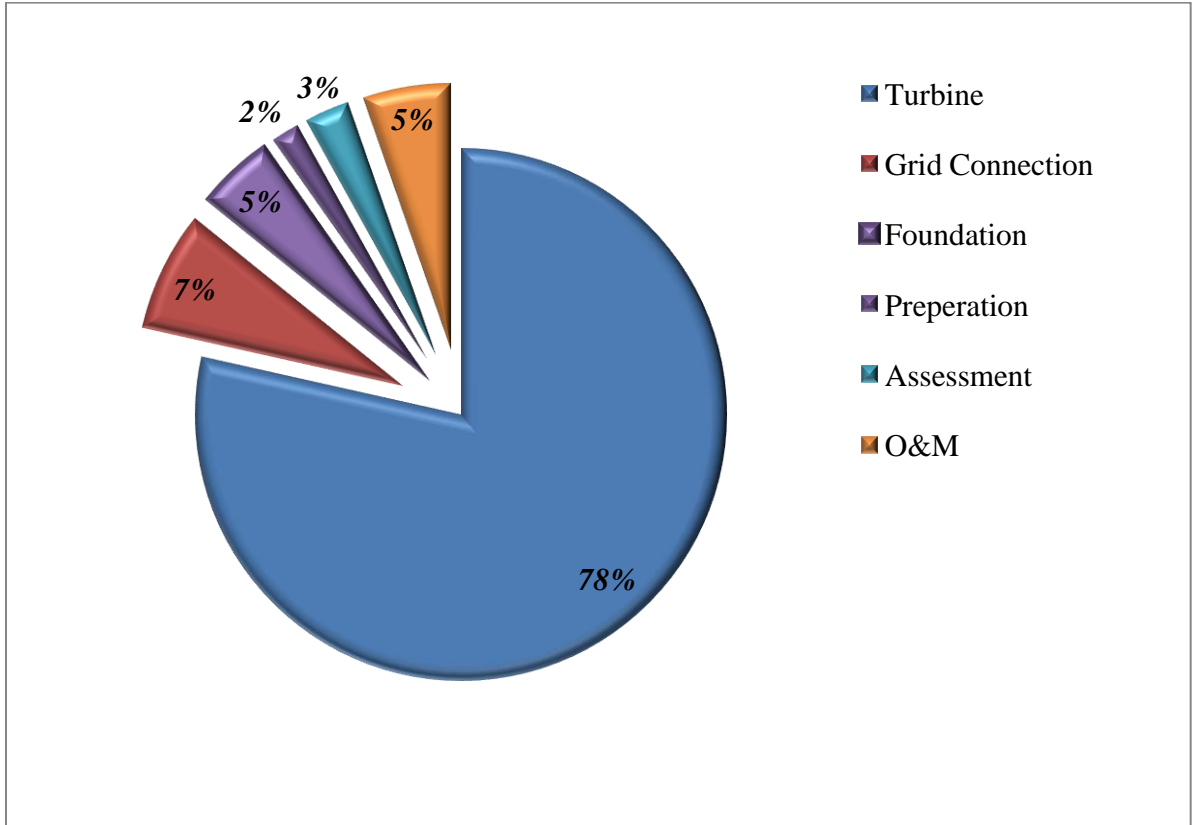


Figure 50: Wind Farm costs breakdown

In this study, we calculate the reduction in AEP uncertainty by using lidars in comparison to traditional met mast measurements. This would result in optimized financing of a wind farm project by reducing the equity investment and increasing the return on equity. Since the modern generation long range scanning Doppler lidars (such as the *WindTracer*) are expensive, the return of investment (ROI) of a lidar system needs to be calculated. The ROI of a lidar system is eventually shown to be extremely positive through the financial gain of uncertainty reduction in WRAP.

7.1 Uncertainty on the future energy production

The AEP is a combination of the wind resource available on site and the power curves of the specific wind turbines selected for that site. The AEP production is usually considered as a Gaussian statistic with a mean value P50 and an uncertainty on the value σ_{AEP} which directly drives the exceedance probability. For example, P90 of 100 GWhr per year means there is 90% chance that the wind farm will produce at least 100 GWh yearly. A sample AEP at P50 of 144 GWh/year as mean and with a σ_{AEP} of 14% is shown in Figure 51 below.

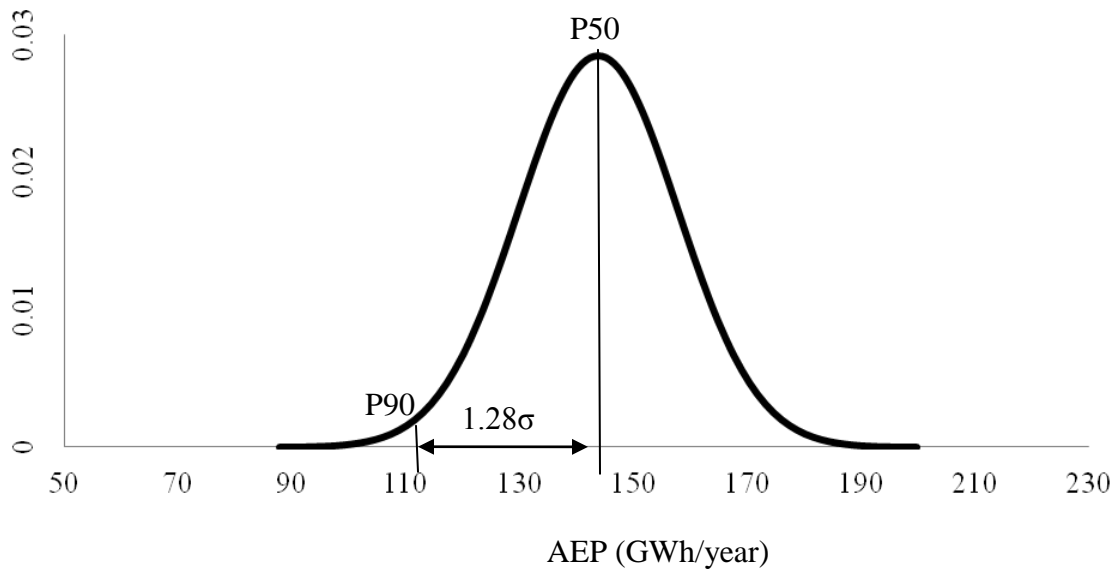


Figure 51. Normal Distribution with P50 at 144 GWh/year and a Std. Deviation of 14% in AEP.

7.2 Sources of uncertainties

Several sources of uncertainties are accounted for wind farm financing. A list of uncertainties used in the below calculations are as follows (Lackner et al. 2007):

1. Wind Speed measurement uncertainty
 - i. Anemometer
 - ii. Calibration
 - iii. Dynamic Over speeding
 - iv. Vertical Flow Effects
 - v. Vertical Turbulence Effects
 - vi. Tower Effects
 - vii. Boom and Mounting effects
 - viii. Data Reduction Accuracy
2. Vertical Extrapolation
3. Long-term resource estimation uncertainty
 - i. MCP Correlation Uncertainty
 - ii. Weibull Parameter Estimation
 - iii. Changes in Long-term average
4. Wind resource variability uncertainty
 - i. Inter-Annual Variability
 - ii. Uncertainty over Turbine Life-time
5. Modeling uncertainty
6. Turbine control losses
7. Power curve uncertainty
8. Climate variability
9. Turbine availability
10. Air density

11. Energy Loss Factors

- i. Availability losses
- ii. Fouling and Icing losses
- iii. Array losses

12. Energy production

- i. Capacity factor estimation
- ii. Capacity factor uncertainty estimation

The total uncertainty varies from site to site. And for a wind farm development with a two to three towers installed for a period of 2 years, the total uncertainty in AEP is ~27% for a year. While for a period of 20 years (i.e., lifetime of the turbine or wind farm) the total uncertainty reduces to 17.5%. Therefore, wind measurement devices capable of measuring at hub-height or a larger spatial region (like the scanning coherent Doppler lidar) can significantly reduce the wind resource assessment uncertainty. The various uncertainties are provided in Table 13. The uncertainty measurements, which would be improved using a scanning Doppler lidar, are highlighted in Table 13. Using a scanning Doppler lidar, the total uncertainty in AEP reduces to 14% (for 20 years) and 24.5% (for a year). The total uncertainty is the square root to sum of squares of individual uncertainties listed above, as shown below:

$$\chi_{Tot} = \sqrt{\chi_1^2 + \chi_2^2 + \chi_3^2 + \chi_4^2 + \dots + \chi_{12}^2}$$

where χ_1^2 is the uncertainty from wind speed measurement, χ_2^2 uncertainties due to vertical extrapolation, so on and χ_1^2 are the total uncertainties from loss of energy production.

Table 13. Uncertainties in wind farm resource assessment

<u>Uncertainties</u>	Baseline	Single Lidar + Baseline	Dual Lidar + Baseline
Wind Speed Measurement Uncertainty	2	2	2
Vertical Extrapolation	2	1	0.25
Long-term Resource Estimation Uncertainty (MCP)	3	3	3
Wind Resource Variability Uncertainty	4	4	4
Modeling Uncertainty/Spatial Variability	6	5	2
Energy Losses	5	5	5
Turbine Control Technique Losses	4	4	4
Power Curve	3	3	3
Climate Variability	4	4	4
Air Density	1	1	1
Turbine Availability	2	2	2
Energy Production	3	3	3
<i>Total Uncertainty</i>	17.64	16.37	14.81

The P-values differs significantly for each of the above uncertainties. Table 14 shows P-values calculated for a 250 MW wind farm.

Table 14. P-Values for various uncertainty estimates from lidar and tower (blah)

Case	Uncertainty (%)	P50 Value	P90 Value	P95 Value	P99 Value
Tower	17.64	613	474	435	361
Single Lidar + Tower	16.37	613	485	448	379
Dual Lidar + Tower	14.81	613	497	464	401

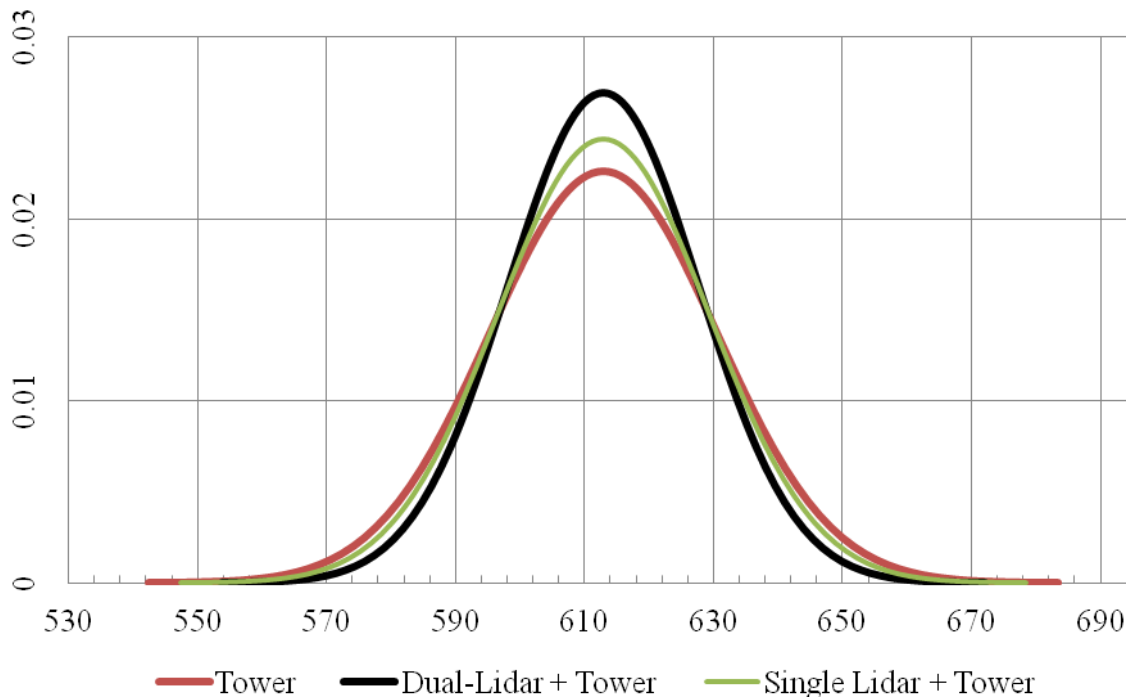


Figure 52. Normal distribution based on different uncertainty estimates from instruments.

7.3 Net present value and return of investment

A detailed discount cash flow analysis was performed to calculate the net present value (NPV) and return of investment (ROI) of a wind farm with and without Doppler lidar deployment at the site for a year. The cost of electricity in wind power generation includes the following components:

1. Economic depreciation of the capital equipment (linear or MACR)
2. Interest paid on the borrowed capital,
3. The operation and maintenance costs,
4. Taxes paid to local and federal authorities,
5. Government incentives and tax credits,
6. Royalties paid to land owners,
7. Payment for electricity used on a standby mode,
8. Energy storage components if used,
9. The cost of wind as fuel is zero

Important definition of terms:

- a. Discount rate:* The discount rate is chosen depending on the cost and the source of the available capital, considering a balance between equity and debt financing and an estimate of the financial risks entailed in the project. Effect of inflation is accounted in the discounted rate. In this analysis, a discount rate of 9% is used for analysis.
- b. Net Present Value:* The net present value (NPV) of a project is the value of all payments, discounted back to the beginning of the investment. If the NPV is positive, the project has a real rate of return which is larger than the real rate of

interest (i.e., discount rate + inflation rate). If the NPV is negative, the project has a lower rate of return.

- c. *Depreciation Cost*: Depreciation is the reduction in the value of an asset due to usage, passage of time, wear and tear, technological outdating, depletion, rust, decay or other such factors. Depreciation is defined as the decline in the capital value of the investment using the internal rate of return as the discounting factor. If the income from the investment is not known, the rate of return is not determined, thus one cannot calculate economic depreciation. Tax depreciation is different compared to economic depreciation. Tax depreciation is a government subsidy (such as the Production Tax Credit (PTC)). A straight line depreciation of turbine equipment costs is used in the analysis below. A linear depreciation of 2.5 percent per year over a 20 year lifetime of the turbine is used in calculations below.

The 20 year NPV was calculated based on a discount rate of 9% for various resource assessment configurations. Table 15 shows the return of investment (ROI) for using a single Doppler versus a Dual-Doppler lidar for wind farm resource assessment. It is assumed that a year-long deployment of the lidar would reduce the shear and micro-siting uncertainty compared to traditional computational models (such as WAsP, Mesoscale, CFD etc...). The ROI for the Dual-Doppler lidar is estimated to be around 12.56 times the value of deploying a lidar in the field for a year, compared to a single Doppler lidar which is expected to gain an ROI of 10.51 times the value of deploying a lidar. A current study is under progress by Lockheed Martin Coherent Technologies (Keith et al. 2013), where multiple Doppler lidars are deployed in the field for a period of

3 months. A tool for calculating ROI and NPV for a wind farm is developed. The details of the scanning pattern are provided as a part of Appendix B.

Table 15. Return of Investment calculations for various resource assessment configurations for a 250MW wind farm

	20 Year NPV (\$)	Additional Equipment Cost to baseline (\$)	Δ 20 year NPV (\$Mil)	ROI
Tower	\$ 51,807,695	--	--	--
Dual Lidar + Tower	\$ 70,649,212	\$ 1,500,000	18.84	<u>12.56</u>
Single Lidar + Tower	\$ 59,691,210	\$ 750,000	7.88	<u>10.51</u>

After further analysis of the field deployment data, currently in progress, the ROI of the lidar for field deployment can be validated with the estimates shown in Table 15. The value proposition of lidar for wind resource assessment is high, although further research needs to be performed to validate this analysis at various terrain conditions. Currently a field study is being performed in Colorado, by Lockheed Martin Coherent Technologies (LMCT), to estimate the shear and micro-siting uncertainties and further understand the various wind power financing options currently available. The scanning strategy for the dual-Doppler lidar deployment, for the study conducted in Colorado, is provided in Appendix B.

8. LIDAR ASSISTED WIND FARM CONTROL – FEASIBILITY STUDY

8.1 Wind turbine and farm control theory

Wind farm control has gained a lot of interest in recent years, in order to reduce loads and maximize power on existing wind turbines and reduce grid fluctuations.

Detailed theories about the turbine and farm level control are provided in sections below.

8.1.1 Wind turbine control basics

All the control algorithms discussed here are for Horizontal Axis Wind Turbines (HAWT). The main components of HAWTs are towers, nacelles, rotors, and the blades. The nacelle has the generator, which is driven by the high speed shaft. The high speed shaft is usually driven by a gear box, which steps up the rotational speed from the low-speed shaft. The low-speed shaft is connected to the rotor, which includes the airfoil-shaped blades. Blades capture the kinetic energy in the wind and transform it into rotational kinetic energy for the wind turbine.

Wind turbine control design objectives for each wind speed region of the power curve (shown in Figure 53) can be specified by:

- Limitation and smoothing of electrical power in the above-rated power area,
- Generation of maximum power in the below-rated power area, and
- Minimization of transient loads in all turbine components.

When power production is below the rated power for the machine, the turbine operates at variable rotor speeds to capture the maximum amount of energy available in the wind. Generator torque provides the control input to vary the rotor speed, and the blade pitch angle is held constant (Pao et al. 2011). For high wind speeds, the primary

objective is to maintain constant output power to its rated value. This is generally achieved by holding the generator torque constant and varying the blade pitch angle. In both control regimes, the turbine response to transient loads must be minimized.

Before deriving a new control method for wind turbines, it is beneficial to review the current and past control approaches. Currently, two types of control strategies being researched: single wind turbine control and wind farm control. The two main categories of control methodology used for wind turbines: classical controls and state-space controls. Below all the above classifications are discussed in detail. Wind turbines may be variable or fixed pitch machines, variable or fixed speed machines. Although fixed pitch machines are less expensive initially, their reduced ability to control loads and change the aerodynamic torque results in higher costs over their life-time. Variable pitch turbines allow parts of their blades to rotate along the pitch axis. Variable speed turbines tend to operate closer to their maximum aerodynamic efficiency for a higher percentage of time, but need to maintain the proper frequency to the electrical grid.

The power curve for a variable speed wind turbine has four zones, Region 1, Region 2, Region 2.5, Region 3 and Region 4 (as shown in Figure 53). When the wind speed is low (i.e., Region 1 - turbine not operational), the power available in the wind is low compared to losses in the turbine systems. When the wind speeds are in the optimal range (Region 2), the turbines are set for maximum power output by maintaining a constant pitch angle. Region 2.5 is the transition range, where the turbine has not reached its rated capacity yet, hence the load mitigation controls are activated in this region. In high wind speed regions (Region 3), when the turbine reaches rated power, the loads are reduced on the turbines by changing the pitch angle and maintaining a constant rotor

speed. Region 4 is the high wind cut-out range, wind speeds above which the wind turbine is powered down and stopped or feathered to avoid excessive operating loads. High wind cut-out typically occurs at wind speeds above 20-30 m/s for large wind turbines.

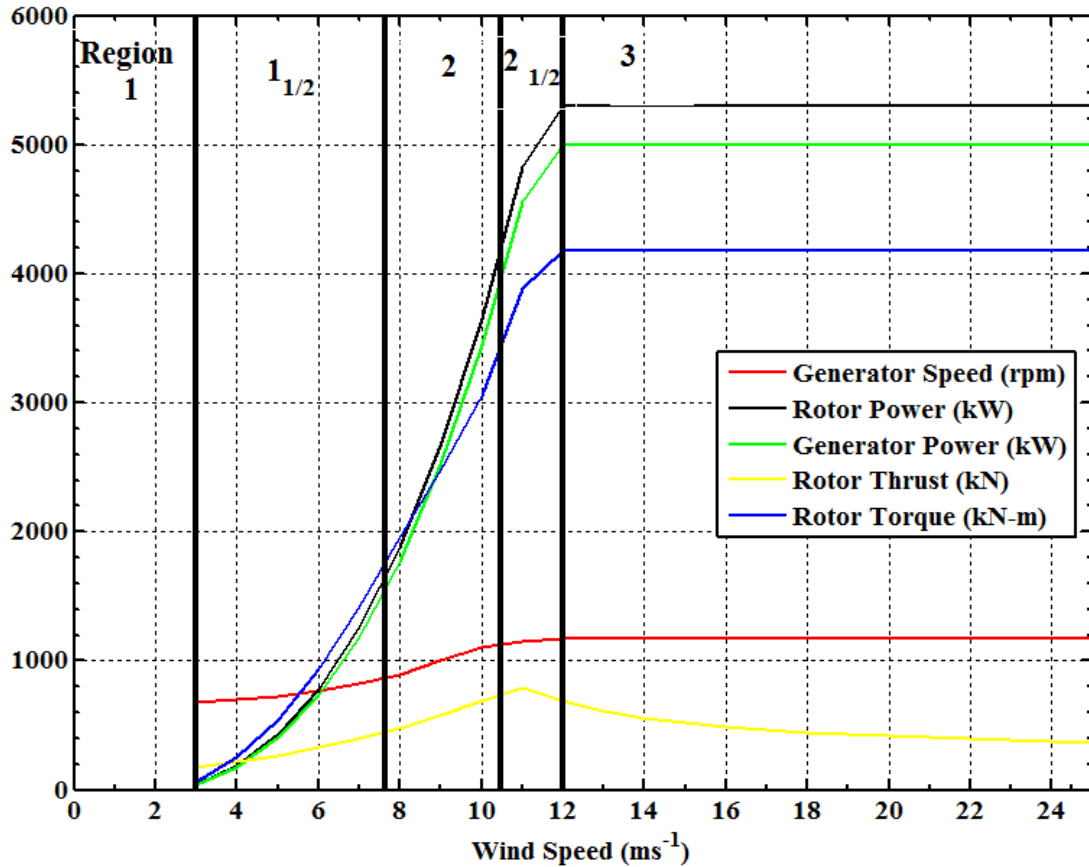


Figure 53. NREL 5MW Turbine parameters (Jonkman et al. 2009).

A wind turbine cannot capture the entire kinetic energy available in the wind. As given in actuator disc theory, the theoretical maximum aerodynamic efficiency is approximately 59% of the wind power (Betz 1926). The reason that an efficiency of 100% cannot be achieved is that the wind must have some kinetic energy remaining after

passing through the rotor disc as else the wind would, by definition, be stopped and would be unable able to pass through the rotor to provide energy to the turbine. The aerodynamic efficiency is the ratio of turbine power to wind power and is known as the turbine's power coefficient, C_p :

$$C_p = \frac{P}{P_{wind}} \quad (18)$$

where P is the power captured by the turbine and P_{wind} is the power available in the wind for a turbine of that size. The power available in the wind is given by:

$$P_{wind} = \frac{1}{2} \rho A \bar{v}^3 \quad (19)$$

Where ρ is the air density, A is the rotor swept area and v is the instantaneous wind speed. The swept area is a circle, with its area equal to πR^2 , where R is the rotor radius. The wind speed, v , is assumed to be uniform across the entire wind turbine rotor swept area. The aerodynamic rotor power is given by

$$P = \tau_{aero} \omega \quad (20)$$

where τ_{aero} is the aerodynamic torque applied to the rotor by the wind and ω is the rotor angular speed. The maximum C_p value for the NREL 5MW wind turbine is 0.48.

For variable speed wind turbines operating in region 2, the control objectives is to maximize energy capture by operating the turbine at the peak of C_p -Tip speed ratio-pitch surface of the rotor. The Tip Speed Ratio (TSR, λ) is defined as;

$$\lambda = \frac{\omega R}{v} \quad (21)$$

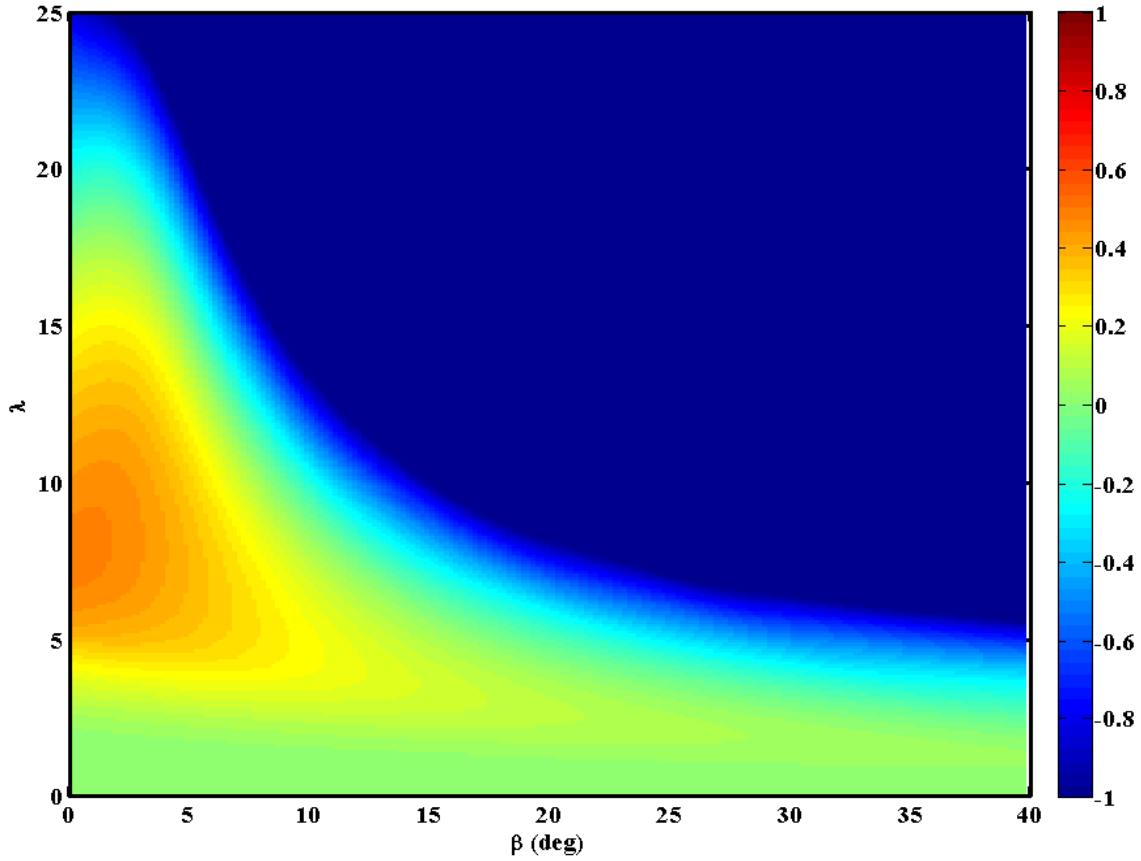


Figure 54. $C_p (\lambda, \beta)$ versus tip-speed ratio and pitch for NREL 5MW wind turbine.

The NREL 5MW C_p data was extracted from `wt_perf.exe` at the NREL website. Since the turbine power is proportional to the power coefficient C_p , the turbine is ideally operated at the peak of the surface. Blade pitch angle is a control variable, whereas tip-speed ratio is controlled indirectly using generator torque control. A turbine's C_p surface can change due to several atmospheric factors. Negative C_p corresponds to motoring operation during which the turbine draws energy from the utility grid. The maximum C_p value for the NREL 5MW wind turbine is 0.485, which is obtained at $\beta^* = 0$, and $\lambda^* = 7.5$.

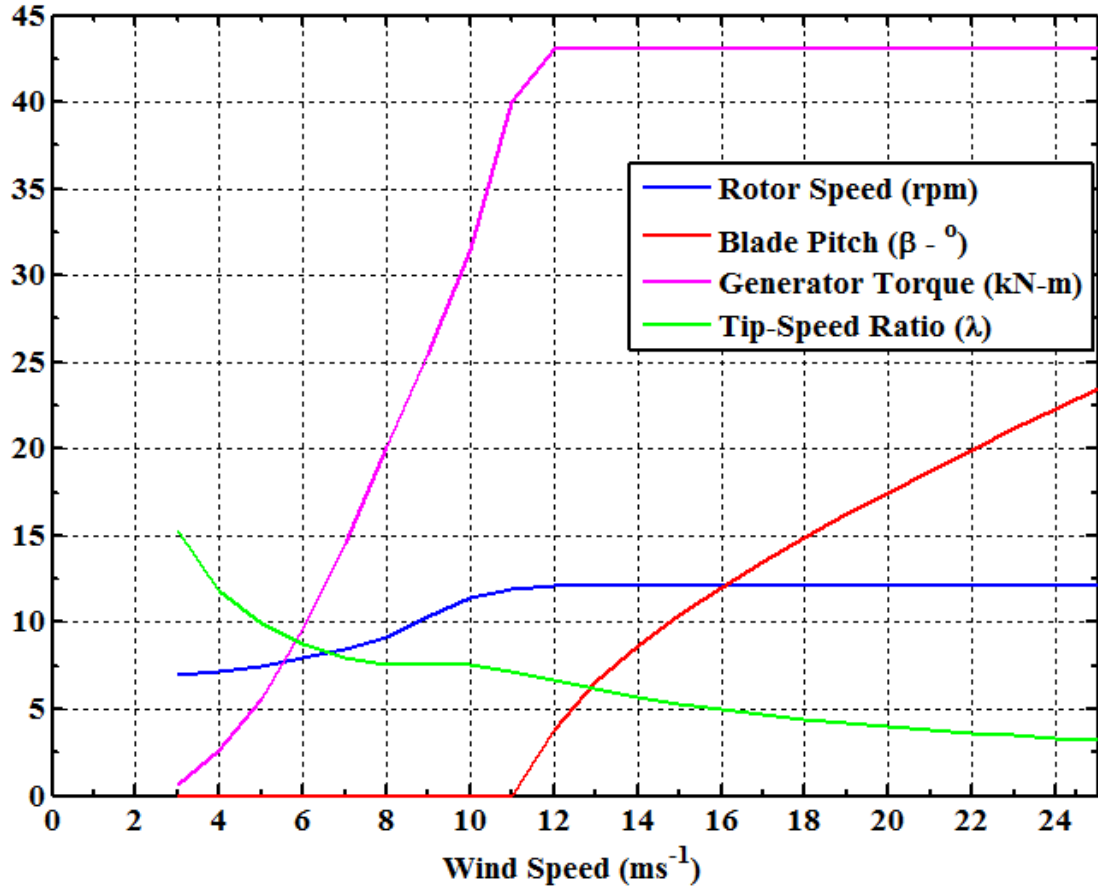


Figure 55. NREL 5MW turbine performance properties

The control torque τ_c is defined as:

$$\tau_c = K\omega^2 \quad (22)$$

the gain K is given by

$$K = \frac{1}{2} \rho A R^3 \frac{C_{p \max}}{\lambda_*^3} \quad (23)$$

λ_* is the tip-speed ratio at which the maximum power coefficient $C_{p \max}$ occurs.

Assuming that the rotor is rigid, the angular acceleration $\dot{\omega}$ is given by

$$\dot{\omega} = \frac{1}{J} (\tau_{aero} - \tau_c) \quad (24)$$

J is the combined rotational inertia of the rotor, gearbox, generator, and shafts and the aerodynamic torque τ_{aero} , is given by (derived from equations above)

$$\tau_{aero} = \frac{1}{2} \rho A R C_q(\lambda, \beta) v^2$$

where

$$C_q(\lambda, \beta) = \frac{C_p(\lambda, \beta)}{\lambda} \quad (25)$$

8.1.2 Classical control designs

Almost all commercial wind turbines currently use classical control. PI (Proportional and Integral) and PID (Proportional, Integral and Derivative) are very popular in the wind industry for power and torque control and recently have been investigated by Bossanyi (2003) for load control. A PID controller has the following equation:

$$y = \left(\frac{K_i}{s} + K_p + \frac{K_d s}{1 + s\tau} \right) x \quad (26)$$

where x is the input error signal, y is the control action, K_i , K_p and K_d are the integral, proportional and derivative gains. The time constant τ prevents the derivative term from becoming too large at high frequency, where it is susceptible to signal noise. For a PI controller $K_d = 0$.

While classical controls have primarily been used in the wind industry to control power, this control also leads to reduction of drive train loads. Such is the case with blade pitch control on fixed speed machines and variable speed variable pitch machines

where the blade pitch serves not only to control the electrical power, but also reduces the rotor torque.

Bossanyi (2003) proposed a load control strategy using individual actuation of full span blade pitch. As the wind turbine blade sweeps through rotor disc, it experiences changes in both wind speed and wind direction as the result of wind shear, yaw misalignment, and turbulence. These variations result in a large once-per-revolution (1P) component of the blade loads, together with harmonics of this frequency, i.e. 2P, 3P, 4P, etc. In three bladed wind turbines these harmonics are generally limited to 3P, 6P, etc. with the other harmonics normally canceling out.

8.1.3 Modern control designs

Classical controls do not address the effect of more than one control objective. When multiple control loops are used, such as pitch and torque loops, the complexity of the controller is greatly increased and stability issues may arise. Oftentimes, artificial methods are used to saturate one control loop so as not to interfere with the other. These details often dominate the actual turning process of a new controller.

Since the controller in a classical Single Input Single Output (SISO) control loop uses only a single measured turbine output as the basis of its control and does not have direct knowledge of the system dynamics of the turbine it is difficult to properly address the control-structure interaction issues using and guarantee system stability. Modern control designs using state space methods more adequately address these issues, since the controller uses a linearized turbine model to determine system states. The controllers can

then be designed to not only maximize power or regulate speed, but also to add damping to important flexible modes, through full state feedback.

In modern design formulation, the linear model for the wind turbine system can be expressed as:

$$\begin{aligned}\dot{\underline{x}} &= A(t)\underline{x} + B(t)\underline{u} + B_d(t)\underline{u}_d \\ \underline{y} &= C\underline{x} + D(t)\underline{u}\end{aligned}\tag{27}$$

Where $\underline{x} \in R^N$ is the state vector, $\underline{u} \in R^M$ is the control input vector, $\underline{u}_d \in R^o$ is the disturbance input vector, $\underline{y} \in R^P$ is the control (or measured) output, $A \in R^{N \times N}$ is the state matrix, $B \in R^{N \times M}$ is the control input gain matrix, $B_d \in R^{N \times o}$ is the disturbance input gain matrix, $C \in R^{P \times N}$ relates the measured output (y) to the turbine states, $D \in R^{P \times M}$ relates the output to the control input and $\dot{\underline{x}}$ represents the time derivative of \underline{x} .

For modern conventional wind turbines, the principal control input is rotor blade collective pitch. The disturbance is the wind input and may included hub height velocity, vertical and horizontal wind shears, while the primary system states include aeroelastic mode consisting of rotor and/or generator speed, blade flap displacement and velocity, tower displacement and velocity. Measured control signals include typical measurements commonly found in existing wind turbines like: generator and/or rotor speed, tower accelerations, and generator torque. They may also include more advanced sensors that have the capability to measure: blade displacement, velocity and acceleration; tower displacement, velocity and acceleration, etc. The controller would then be designed for an optimal mix of rotor speed control, fatigue reduction, and computational complexity.

8.1.4 Turbine modeling

The NREL 5MW turbine (Jonkman et al. 2009) is taken as reference turbine and the characteristics as mentioned in Jonkman (2009) is used for this analysis. The components of the turbine are shown in the figure below.

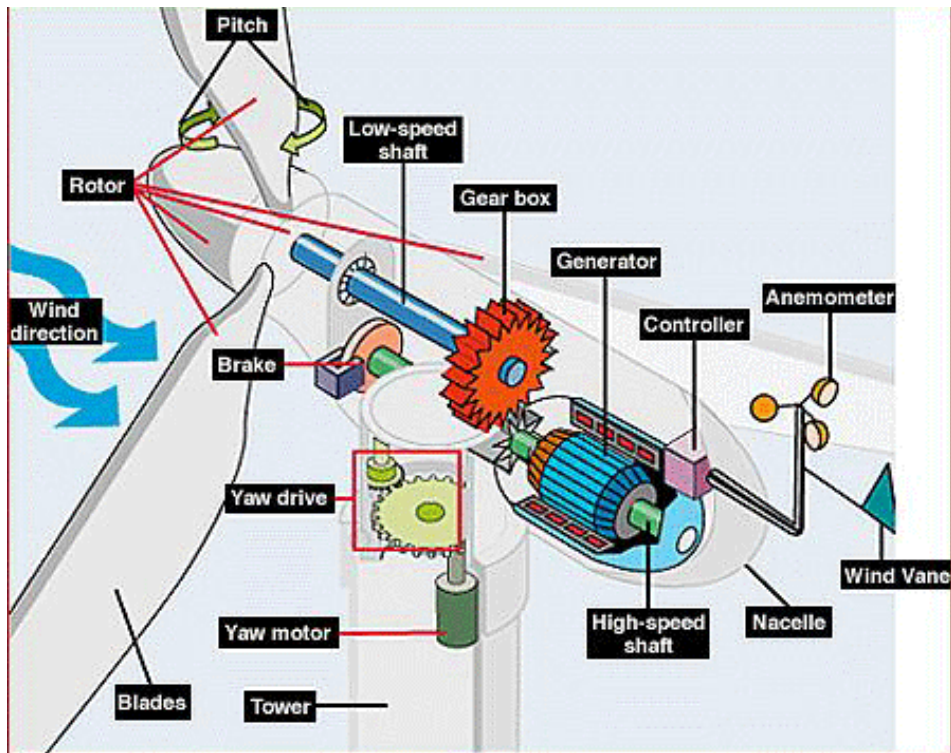


Figure 56: Wind turbine nacelle schematic. All the turbine components shown in the figure are modeled (Picture Courtesy of NREL).

The aerodynamics of the turbine can be described using the relationships:

$$\tau = \frac{P_r}{\omega_r} = \frac{1}{2} V^3 \rho A C_p(\lambda, \beta) \omega_r^{-1} \quad (28)$$

$$F_t = \frac{1}{2} V^2 \rho A C_T(\lambda, \beta) \quad (29)$$

where T_s is the main shaft torque, F_t is the thrust force and ω_r is the rotor speed. C_p and C_T are two look-up tables derived from the geometry of the blades with tip-speed ratio and pitch angles as inputs. The tables for NREL 5MW turbine are generated using wt_perf.exe (found in the NREL website - nrel.gov). Typical thrust coefficients are shown below in Figure 57. From the thrust and torque relations above, it is evident that an incremental change in pitch is accompanied by changes in the rotor thrust and torque that depend on the local gradients of the thrust and torque coefficients in Figure 54 and Figure 57

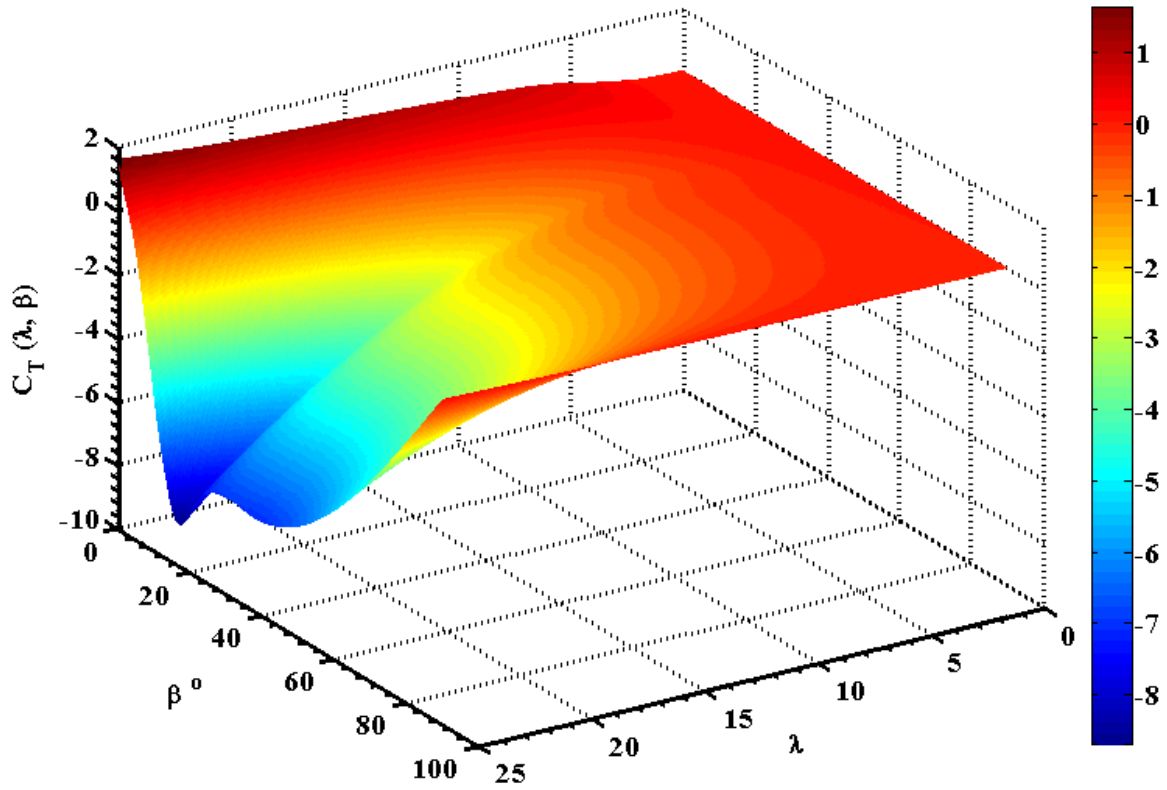


Figure 57. C_T versus tip-speed ratio and pitch for NREL 5MW wind turbine.

The drive train model consists of a low-speed shaft rotating with a speed ω_r and a high-speed shaft rotating with a speed ω_g , having inertias J_r and J_g , respectively. The shafts are interconnected by a gear with a ratio N . A torsion stiffness K together with a torsion damping K_d results in a torsion angle α that describes the twist of the flexible shaft. This leads to the following drive train model (Stotsky et al. 2012).

$$\dot{\omega}_r = \frac{1}{J_r} (T_s - \alpha K_s - \dot{\alpha} K_d) \quad (30)$$

$$\dot{\omega}_g = \frac{1}{J_g} \left(\frac{1}{N} (\alpha K_s + \dot{\alpha} K_d) - T_g \right) \quad (31)$$

$$\dot{\alpha} = \omega_r - \frac{1}{N} \omega_g \quad (32)$$

Multiplication of both sides of equation 30 and 31, by N and after summation, leads to

$$J_r \dot{\omega}_r + N J_g \dot{\omega}_g = T_s - N T_g \quad (33)$$

where the term $K_s \alpha + K_d \dot{\alpha}$ that represents the torque between the shafts is cancelled. The torsion rate $\dot{\alpha}$ is several times smaller than the turbine speed ω_r . Therefore, the generator speed divided by the gear ratio is an acceptable approximation of the turbine speed. A simple generator model is also implemented, with the power reference as an input.

The pitch actuator is modeled as a first-order lag with the rate and range constraints. The PI based control is based on power gain scheduling approach linearized at various control region set-points (P_{dem}^*) and generator speed error. The gains (i.e., integral and proportional) are calculated based on linearization of the power production sensitivity to

blade pitch angle (Spudic et al. 2010). The pitch angle calculated based on power reference and generator speed error is shown below:

$$\beta = K_p \omega_{err} + K_i \int \omega_{err} \quad (34)$$

K_p and K_i are the proportional and integral gains, which are a function of the pitch angle. The tower deflections of the NREL 5MW turbine are modeled as a spring damper system. Several advanced turbine controllers as discussed in Bossanyi et al. 2012 can be implemented. The NREL 5MW turbine parameters are provided in Appendix C.

8.1.5 Wind farm wake modeling

An important part of wind farm control is modeling the wake propagation in the wind farm. The incoming winds from lidar are fed as inputs to the wind model, for future prediction of wake structure and wake meandering. This has to be modeled accurately to guide the wind turbines behind the front row of turbines. The wind direction is taken into account for evolving wake structures. To this respect, Frandsen's (2006) model for single wake and multiple wakes are modeled in Simulink (Matlab 2010). Modifications for evolving wind directions are taken into account (Larsen et al. 2008). As shown in Frandsen et al. 2006, the model encompasses three regimes (shown in figure below).

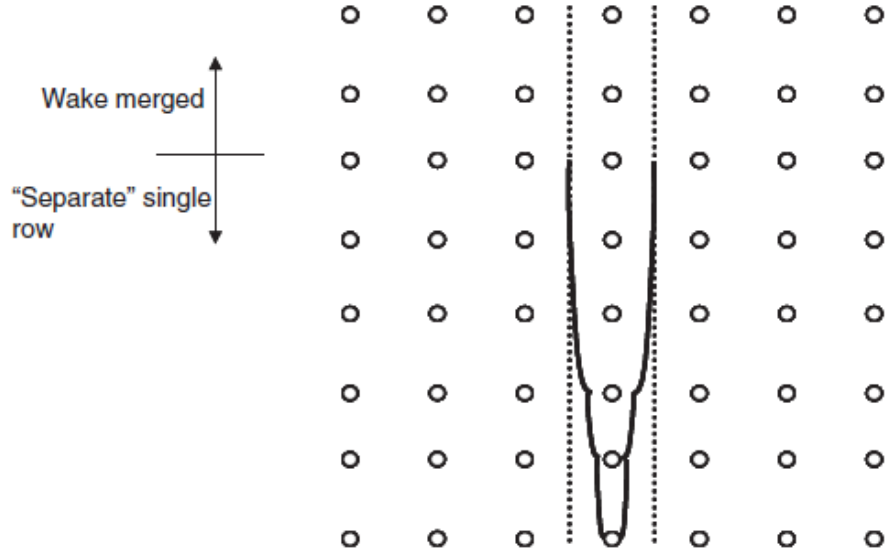


Figure 58. Illustration of regimes of the Frandsen's (2006) model. The wind from south is parallel to the direction of the rows.

Based on incoming wind direction, turbines upwind and downwind are recognized, and the effect of the upwind turbines on downwind turbines are modeled. If the turbine is in free-flow conditions (i.e., no wake effects), the deficit is 1, else the wake effects from multiple or single turbines are modeled as shown above. As per the Frandsen's model, the wake diameter is modeled as:

$$D(x) = (\psi^{(k/2)} + \varepsilon s)^{1/k} D_o, \quad (35)$$

where $s = x/D_o$ and the initial wake diameter is $\sqrt{\psi} D_o$ & $\psi = \frac{1}{2} \frac{1 + \sqrt{1 - C_T}}{\sqrt{1 - C_T}}$. Based

experimental data, k is assumed to be equal to 2 and ε is 0.5. The deficit for a single turbine is then given as:

$$\frac{U}{U_o} \cong 1 - \frac{1}{2} C_T \frac{A_o}{A}. \quad (36)$$

For multiple wakes the recursive deficit equation as mentioned in Frandsen et al. 2006 is used as shown below. Only a single row of wind turbines is considered and in that row the wake between wind turbine n and n+1 is described in the equation below. The case of multiple wakes is dealt with as illustrated in Figure 59.

$$\frac{U_{n+1}}{U_o} = 1 - \left(\frac{A_n}{A_{n+1}} \left(1 - \frac{U_n}{U_o} \right) + \frac{1}{2} \frac{A_R}{A_{n+1}} C_T \frac{U_n}{U_o} \right). \quad (37)$$

The computed model was compared to data (as observed by Frandsen), and are compared in Figure 60. Good correlation is observed between data and the model. This provides the validation, that the model was computed with reasonable accuracy. The model does not account for atmospheric stability, terrain. The Achilles heel for improving wind farm performance is the lack of predictability of wake effect models in a wind farm. Therefore, a site/condition enhancement to the wake model should yield more accurate results. The wake diameter for various downwind distances as estimated by the model (Equation 35) is shown in Figure 61.

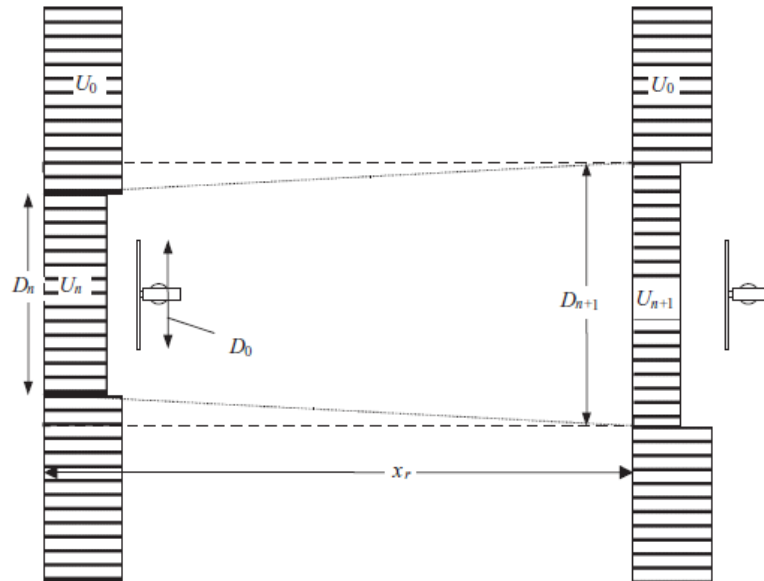


Figure 59. Flow between two wind turbines in a row of wind turbines (Frandsen et al. 2006).

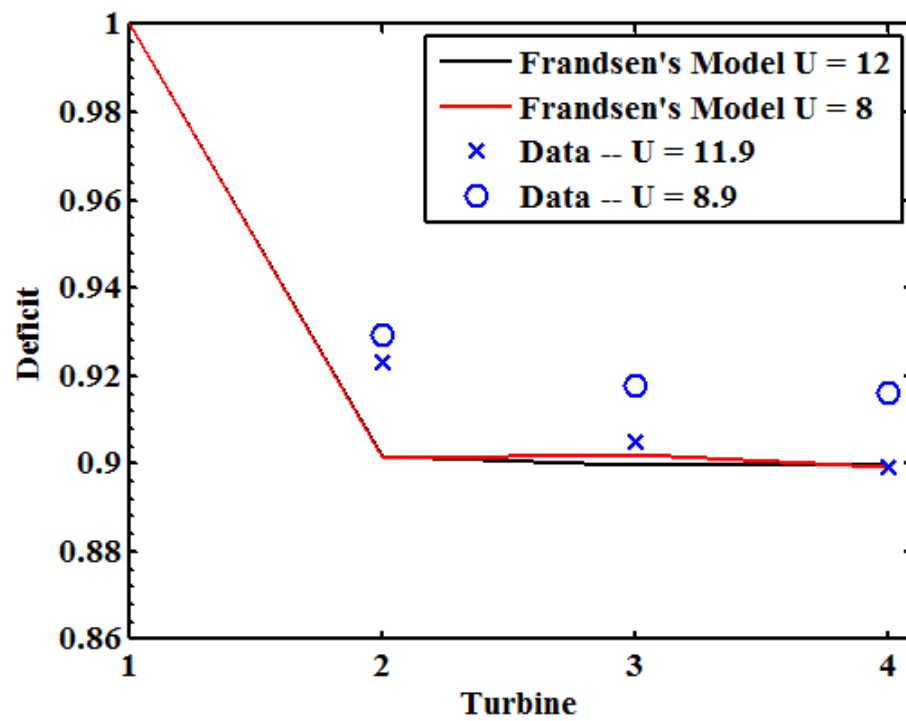


Figure 60. Frandsen's Model deficit comparison to data extracted from Frandsen et al. 2006

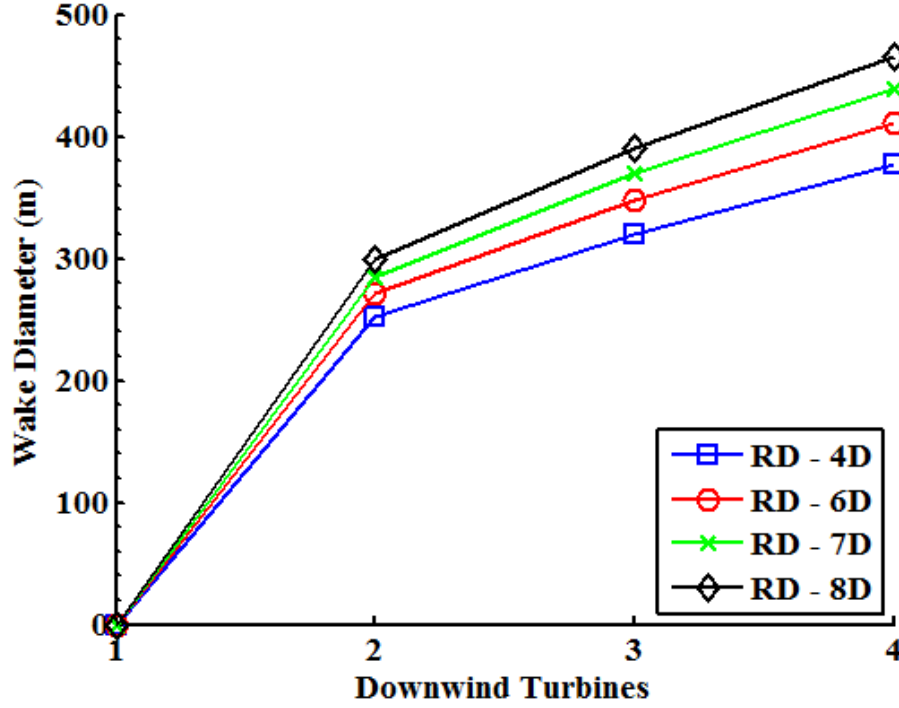


Figure 61. Wake diameter for 3 turbines downwind as estimated based on Equation 31. For various downwind spacing or Rotor Diameter (RD) and $C_T = 0.8$.

The upstream turbines are estimated based on the mean wind direction observed by the lidar at 1 km away from the wind farm. The turbines not affected by wake are given a deficit of 1. The upstream turbines are estimated based on the angle subtended by each turbine on the given wind direction, as described below. Given the wind direction θ , any two turbines, i and j located within the wind farm, the angle β_{ij} , between the vector, originating at turbine j 's cone vertex A to turbine i and the vector, originating at A turbine j , β_{ij} , ($0 \leq \beta \leq \pi$) is calculated as:

$$\beta_{ij} = \cos^{-1} \left\{ \frac{(x_i - x_j) \cos \theta + (y_i - y_j) \sin \theta + R/k}{\sqrt{(x_i - x_j + R/k \cos \theta)^2 + (y_i - y_j + R/k \sin \theta)^2}} \right\} \quad (38)$$

Thus if the angle, β_{ij} , is greater than the wake expansion angle ($\alpha = \arctan(k)$), then the turbine j is not in the wake of turbine i . k is equal to the wake expansion coefficient, which is assumed to be equal to 0.106 (based on experimental data observed in Frandsen et al. 2006). Hence the angle subtended by the wake is equal to 6.05° . If any angle subtended by one turbine on the other is greater than 6.05° , the turbine is flagged with a 0 index, while if less than the angle, it's flagged with a 1 index. Hence the upstream and downstream turbines can be easily categorized for wake analysis.

8.1.6 Wind speed evolution model

Lidar data measured 1-2 kilometers ahead of the wind farm at hub height evolves before it reaches the wind farm. To capture the evolution of the wind, the Mann spectral method is applied (Mann 1994). In the Mann uniform shear turbulence model the isotropic von-Karman energy spectrum is assumed to be rapidly distorted by a uniform, mean velocity shear (estimated by simple power law currently). The spectral coherence parameters as specified in International Energy Commission (IEC) standards are used in this study. These parameters are site specific, therefore for more accurate modeling, all the parameters, e.g., the integral length scale (L_o) and the dissipation rate (ϵ), need to be calculated for the site under consideration. The IEC standard parameters were validated for a flat terrain site and work well under those conditions. For a complex terrain scenario, these models are not expected to be as accurate. The Mann spectral tensor components $\Phi_{ij}(k_1, k_2, k_3)$ are given by the following equations:

$$\Phi_{11}(k_1, k_2, k_3) = \frac{E(k_0)}{4\pi k_0^4} [k_0^2 - k_1^2 - 2k_1(k_3 + \beta(k)k_1)\zeta_1 + (k_1^2 + k_2^2)\zeta_1^2], \quad (39)$$

$$\Phi_{22}(k_1, k_2, k_3) = \frac{E(k_0)}{4\pi k_0^4} [k_0^2 - k_2^2 - 2k_2(k_3 + \beta(k)k_1)\zeta_2 + (k_1^2 + k_2^2)\zeta_2^2], \quad (40)$$

$$\Phi_{33}(k_1, k_2, k_3) = \frac{E(k_0)}{4\pi k_0^4} [(k_1^2 + k_2^2)], \quad (41)$$

$$\Phi_{12}(k_1, k_2, k_3) = \frac{E(k_0)}{4\pi k_0^4} \left[-k_1 k_2 - k_1(k_3 + \beta(k)k_1)\zeta_2 - k_2(k_3 + \beta(k)k_1)\zeta_1 + (k_1^2 + k_2^2)\zeta_1 \zeta_2 \right], \quad (42)$$

$$\Phi_{13}(k_1, k_2, k_3) = \frac{E(k_0)}{4\pi k_0^2 k^2} [-k_1(k_3 + \beta(k)k_1) + (k_1^2 + k_2^2)\zeta_1], \quad (43)$$

$$\Phi_{23}(k_1, k_2, k_3) = \frac{E(k_0)}{4\pi k_0^2 k^2} [-k_2(k_3 + \beta(k)k_1) + (k_1^2 + k_2^2)\zeta_2], \quad (44)$$

and the Mann coherence spectrum for spatial separations normal to the along-wind direction is given by:

$$\gamma_{ij}^2(f) = \frac{\left| \int_{-\infty-\infty}^{+\infty+\infty} \int_{-\infty-\infty}^{+\infty+\infty} \Phi_{ij}(k_1, k_2, k_3) e^{-ik_2\delta_2} e^{-ik_3\delta_3} dk_2 dk_3 \right|^2}{\int_{-\infty-\infty}^{+\infty+\infty} \int_{-\infty-\infty}^{+\infty+\infty} \Phi_{ii}(k_1, k_2, k_3) dk_2 dk_3 \int_{-\infty-\infty}^{+\infty+\infty} \int_{-\infty-\infty}^{+\infty+\infty} \Phi_{jj}(k_1, k_2, k_3) dk_2 dk_3}, \quad (45)$$

where i and $j = 1, 2, 3$ for the along-wind, cross-wind and vertical turbulence components, respectively, $\delta_1, \delta_2, \delta_3$ are the non-dimensional spatial separation vector components,

defined as $\delta_i = D_i / l$, k_1, k_2, k_3 are the non-dimensional spatial wave numbers, defined

as $k_i = 2\pi f l / U$, l is an isotropic scale parameter proportional to the isotropic integral

length scale L , $k = \sqrt{k_1^2 + k_2^2 + k_3^2}$, $k_0 = \sqrt{k^2 + 2\beta(k)k_1k_3 + [\beta(k)k_1]^2}$, and

$$\zeta_1 = C_1 - (k_2 / k_1) C_2, \quad (46)$$

$$\zeta_2 = (k_2 / k_1) C_1 + C_2, \quad (47)$$

$$C_1 = \frac{\beta(k)k_1^2 \{k_1^2 + k_2^2 - k_3 [k_3 + \beta(k)k_1]\}}{k^2 (k_1^2 + k_2^2)}, \quad (48)$$

$$C_2 = \frac{k_2 k_0^2}{(k_1^2 + k_2^2)^{3/2}} \arctan \left(\frac{\beta(k)k_1 \sqrt{(k_1^2 + k_2^2)}}{k_0^2 - [k_3 + \beta(k)k_1] \beta(k)k_1} \right), \quad (49)$$

The non-dimensional, von Karman isotropic energy spectrum is given by,

$$E(k) = \frac{1.453k^4}{(1+k^2)^{17/6}}, \quad (50)$$

and the eddy lifetime is given by

$$\beta(k) = \frac{\gamma}{k^{2/3} \sqrt{{}_1F_2\left(\frac{1}{3}, \frac{17}{6}, \frac{4}{3}, -k^{-2}\right)}}, \quad (51)$$

and γ is the shear parameter, while ${}_1F_2(\cdot)$ is the hyper-geometric function. The hyper-

geometric function is defined as (Oberhettinger 1972)

$$F(n, d, z) = \sum_{p=0}^{\infty} \frac{M_{n,p}}{M_{d,p}} \frac{z^p}{p!},$$

where

$$M_{n,p} = \prod \frac{\Gamma(v_j + k)}{\Gamma(v_j)}$$

Once the covariance tensor is estimated, to simulate the 3-D wind field, the stochastic velocity field in terms of a generalized Fourier integral is given as:

$$\mathbf{u}(\mathbf{x}) = \int e^{ik \cdot \mathbf{x}} d\mathbf{Z}(\mathbf{k}) \quad (53)$$

where the integration is over all wave number space. \mathbf{Z} is connected to the spectral tensor by

$$\langle dZ_i^*(k) dZ_j(k) \rangle = \Phi_{ij}(k) dk_1 dk_2 dk_3 \quad (54)$$

which is valid for infinitely small dk and $*$ represents the complex conjugate. The Fourier integral can be converted to discrete series by:

$$\mathbf{u}(\mathbf{x}) = \sum_k e^{ik \cdot \mathbf{x}} C_{ij}(k) n_j(k) \quad (55)$$

Once the coefficients are estimated (as shown in Mann 1994), the wind field can be evaluated by Fourier Transform (FFT). The IEC standard parameters are currently used for wind field simulation, these parameters needs to be tweaked based on site conditions. The IEC standard parameters used for the current simulation are shown in the Table 16 below.

Table 16: IEC Standard Parameters

Shear Parameter (γ)	3.9
Power Law Shear Exponent (α)	0.2
Turbulence in U (σ_u)	$TI * (0.75 * U_{hub} + 5.6)$
Turbulence in V (σ_v)	$0.7 * \sigma_u$
Turbulence in W (σ_w)	$0.25 * \sigma_u$
σ_{iso}	$0.55 * \sigma_u$
Isotropic Scale Parameter (l)	33.6

The Mann simulation was performed for various input wind speeds from 3 ms^{-1} to 25 ms^{-1} , for various TI and shear exponent values. A look-up table was created, which can be used in the control option, to reduce the computational complexity for real-time operation.

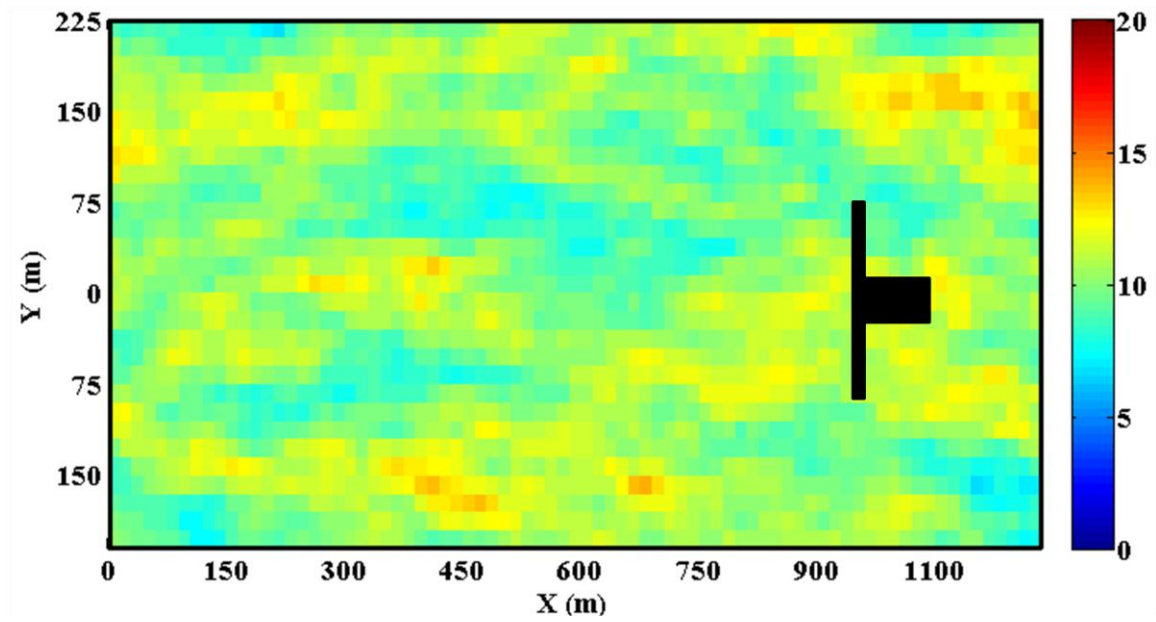


Figure 62: Sample spatial wind field from the Mann Spectral model at hub height wind speed of 10m/s, TI of 12% and IEC standard parameters. The color bar represents wind speed in ms^{-1} and X, Y represents the horizontal & lateral displacement distance.

For lidar winds observed at distances greater than 5 km, the energy content measured ahead is used to estimate the available power at the wind farm. This information can be used by the demand operator to schedule balance generators, but the wind speed evolution is not applied for distances greater than 2 km.

8.1.7 Lidar assisted wind farm control theory

The wind interaction between turbines, due to wakes, results in varying power outputs for each turbine. The central idea behind Lidar Assisted Wind Farm (LAWF) control is to sense the winds ahead of the wind farm (a few minutes ahead), and use the information to adjust the wind turbine parameters, optimize the array compared to “greedy” individual turbine control and reduce grid variability. Multiple wind farm control strategies are analyzed in this study:

- a) Maximize total wind farm power, based on long-range scanning lidar input few kilometers ahead of the wind farm,
- b) Maintain the total power demand for the wind farm as set by the operator, based on grid load requirement and lidar input,
- c) Minimize the loads on downwind turbines, by maintaining the balance between available wind power and demand power.

The control of the wind farm is split into farm level control and turbine level control. The wind farm control distributes power set-points to all the turbines in the farm, i.e. each turbine is given a reference power set-point which needs to be met by the turbine, as provided by the wind farm controller (shown in Figure 63). The local turbine controller in each wind turbine ensures that the output power of turbine tracks the given power set-point. At the same time, the local wind turbine controller seeks other objectives, e.g. ensures structural stability. The wind farm controller distributes power set-points to each turbine based on the three options chosen above. The wind farm controller has access to the lidar measurements ahead of the wind farm and also interacts with the utility operator. Currently, in the industry, the wind farm controller determines the power based on wind measurements (behind the nacelle of the turbine) in the wind farm and on long term wind predictions. Based on these measurements, static power set-points to all the turbines in the farm are provided.

In this work, we examine how to exploit the freedom in choosing the power set-points dynamically, such that the loads on the turbines in the wind farm are reduced. Moreover, the power requirement set by the demand operator is also attained, with

information about winds ahead of the wind farm using a scanning coherent Doppler lidar.

The overall wind farm control system is shown below:

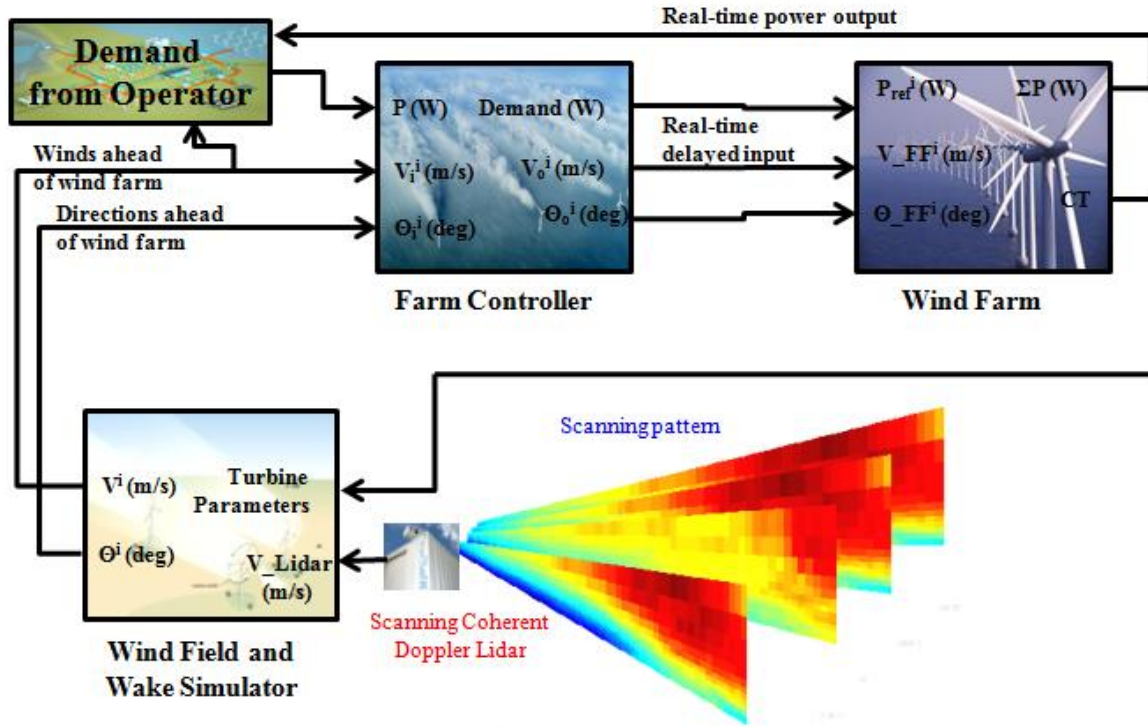


Figure 63. Coherent Doppler lidar informed wind farm control structure.

The input to the turbines is the power demand from the grid. The power demand for each turbine is based on different scenarios a) equal power distribution to all the turbines based on the demand, b) less power demand for the upstream turbines (by increasing the pitch angles and reducing the loads on the turbines) and optimizing total wind farm power and c) maintaining grid efficiency by taking maximum power from the upstream turbines and reducing the power for turbines affected by wakes/turbulence (results in load reduction of the turbines). Several other optimization procedures can be applied explicitly to help reduce the loads (based on tweaking the C_p and C_t values), but

are beyond the scope of this thesis. For power optimization based on loads, please refer to Soleimanzadeh et al. 2012.

8.1.8 Wind farm demand based control

On the farm level, the control input to a turbine is the power reference (P_{ref}). Therefore, the power reference for each turbine is an input from the lidar data ahead of the wind farm to maximize power production and any other set power demand as set by the operator. A turbine will only respond to farm control if the reference power is greater than minimum available power and less than the maximum available power i.e.

$$P_{min} \leq P_{ref} \leq P_{avail} \quad (56)$$

where P_{min} is the minimum available power a turbine can sustain to produce power, and P_{avail} is the maximum available power of the turbine for the given wind speed. The ideal power tracking curve is shown in Figure 64.

During the demand based control option, the wind turbines can be coordinated to reduce loads on the downwind turbines and maintain the demand as set by the controller. The downwind turbines are categorized based on incoming direction by lidar measurements. By reducing the power reference signals of downwind turbines and maintaining the total demand power, the lifetime of individual downwind turbines can be increased. The distribution of available power can be controlled in several different ways, two methods analyzed in this study are:

a) Upwind Equal Power: By distribution of the demand based on available power at the wind farm, where the power references are provided by distribution of available

power based on the total demand set by the wind farm demand controller as shown below:

$$P_{ref}^i = P_{demand} \left(\frac{P_{avail}^i}{\sum_i P_{avail}^i} \right) \quad (57)$$

where P_{ref}^i is the reference power provided to each turbine, P_{demand} is the total wind farm power demand set by the operator, P_{avail}^i is the available power at each turbine.

b) Upwind Direction Control: This is performed by reducing only the downwind turbine power reference and extracting maximum power from upwind turbines. This is expected to reduce fatigue loads on downwind turbines.

The results for all the options are shown below. Further effects of reducing power signals (or derating) on wind turbines are shown in Deshpande et al. 2012.

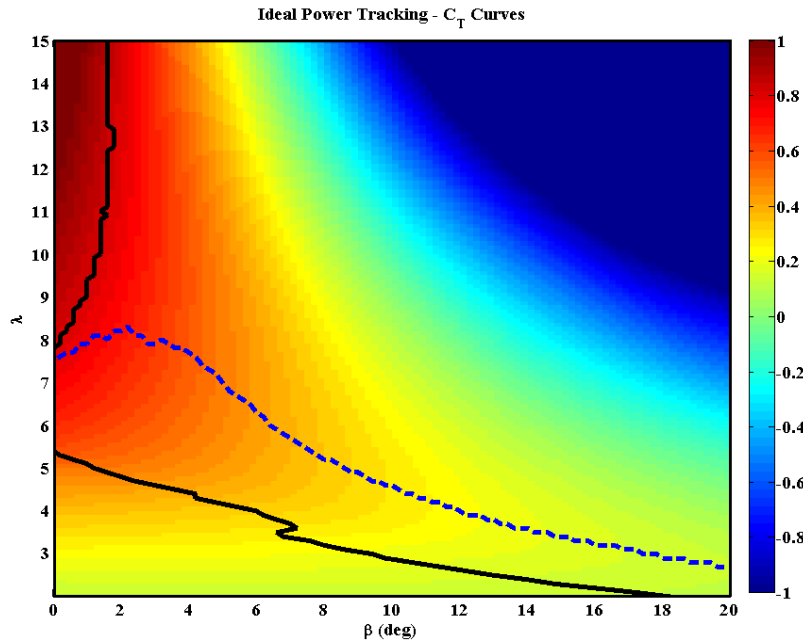


Figure 64: Ideal power tracking β and λ curves. The black line shows optimal pitch angles for various λ and blue dotted line represents optimal λ for various pitch angles.

8.2 LAWF control results

Coherent Doppler Lidar systems are able to measure wind conditions 5- 15 kilometers in front of wind turbines and are therefore able to sense approaching changes of extractable energy content in the wind. In this research study, a preview-based control is investigated as a basis for novel control for wind farm power maximization and load mitigation.

LAWF is tested on existing Doppler lidar-retrieved wind fields on a designed wind farm layout. The first-order effects of wind turbine loads are explored. Wind fields which could be challenging for current “blind” control algorithms will be used to test the efficiency of the control algorithms. An inability to “see” approaching flow disturbances translates into late or inappropriate wind farm control. The stochastic nature of wind resources, the high initial capital cost, and the increasing structural flexibility of modern turbines motivate the adoption of advanced instrumentation and measurement technologies. CDL measurements make it possible to employ wind farm control strategies using a preview of actual wind speeds, instead of employing wind estimates obtained from measurements at the turbine nacelle which do not provide any preview.

8.2.1 LAWF turbine model comparison to NREL FAST model

To evaluate the performance of the LAWF turbine controller, it was compared to the NREL FAST model (single wind turbine controller, developed by NREL) which is publicly available for download at www.nrel.gov. The NREL FAST model computes the loads and power output from a single turbine. A few notable differences between the NREL FAST Controller and the control described in this thesis are as follows:

- a) LAWF calculates only the first-order dynamics of the turbine control,
- b) LAWF models the entire wind farm, while FAST models a single turbine

- c) LAWF models wind farm wakes and accounts for wake interaction effects,
- d) FAST assumes Taylor's hypothesis for wind farm advection, while LAWF take real-time lidar input and uses the spectral Mann model for advection,
- e) FAST uses torque reference as input, while LAWF uses power reference as input,
- f) The turbine pitch control in LAWF is based on power reference input,
- g) A simple PID yaw control is also modeled in LAWF,
- h) LAWF also optimizes the turbine outputs based on power demand from the grid operator.

For appropriate comparison to FAST, the NREL 5MW turbine characteristics were applied to the LAWF control, which can be easily altered to any turbine characteristics. Several wind speed scenarios, as computed by TurbSim model, were inter-compared. Reasonable comparisons between the LAWF and FAST controls are observed. Turbsim generates winds over a 3D grid space, which is used as an input into the FAST model. The standard parameters of the TurbSim model were used, while the average hub-height winds were changed for various iterations. Standard FAST degrees of freedom (DOF) were used to simulate the loads and power of the 5MW wind turbine. Figure 65 shows the comparison between LAWF and FAST for a wind speed input of 18ms^{-1} . Although good comparisons are found in general, the LAWF control does not damp the signal as much as FAST controller. Several differences mentioned above are a few reasons for various variations observed between both the controllers. The LAWF controller averages the response of the available power based on ideal reaction curves. Figure 66 shows the power output comparison between both the controllers. The power set-points for the LAWF controller was set to 5MW (rated power), and it can be observed that the standard

deviation of power set-point and the power output from the controller is small. Figure 67 shows the pitch angles for various power set-points of the LAWF controller. It can be observed that the pitch angles increase with reduced power reference set-points.

Therefore, the loads on the turbines can be reduced by increasing pitch angles and maintaining grid efficiency. The LAWF controller was compared for various wind speed scenarios. Figure 68 shows the comparison between the controllers for a low-wind speed scenario (average wind speed of 5ms^{-1}), and reasonable comparison can be observed.

The LAWF controller matches the available power fluctuations well, while the FAST controller is designed to reduce the loads and not maximize power. The pitch angles for both the controllers are set to zero, to maximize power at low wind speeds. Figure 69 shows the generator torque and tower thrust forces computed by both the controllers.

The FAST controller is better at reducing loads compared to the LAWF controller; the reason for the improved performance could be due to various DOF's introduced in the FAST controller. Therefore, by increasing the DOF in the LAWF controller could improve the performance in load reduction. Figure 70 shows the tower deflections observed by both the controllers. Reasonable comparison can be observed between both the controllers, the LAWF controller has smaller tower fluctuations compared to the FAST controller.

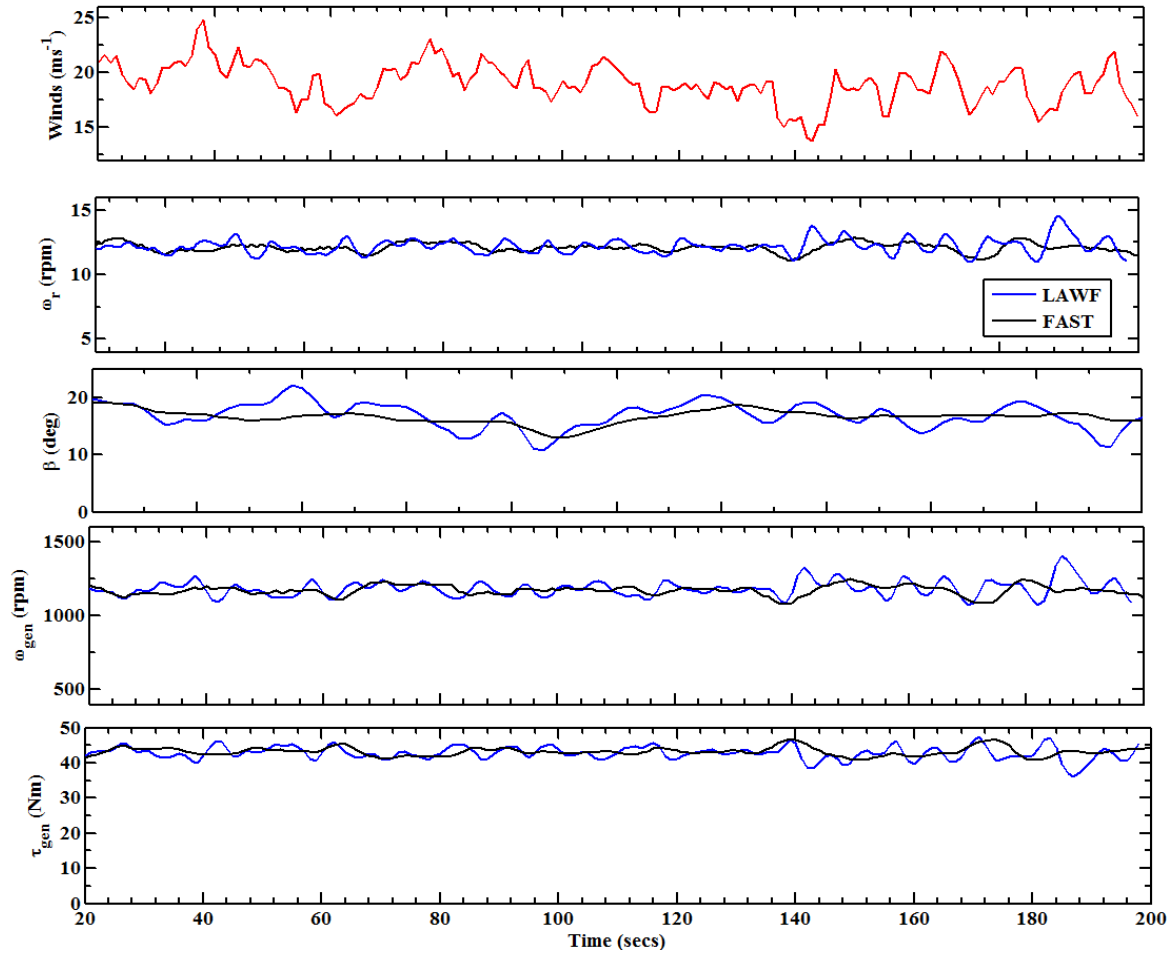


Figure 65. LAW control comparison to NREL FAST for an average turbulent wind speed of 18m/s, as simulated in TurbSim. The figure above shows a) winds, b) rotor speed, c) pitch angle, d) generator speed, and e) generator torque.

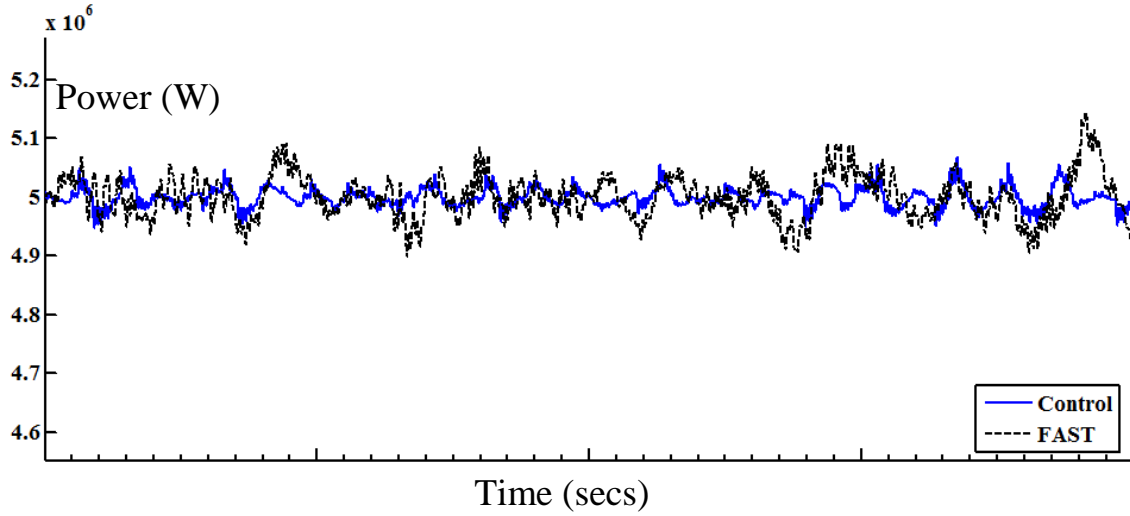


Figure 66. Power time series comparison between LAWF and FAST for turbulent wind speed at 18ms^{-1} .

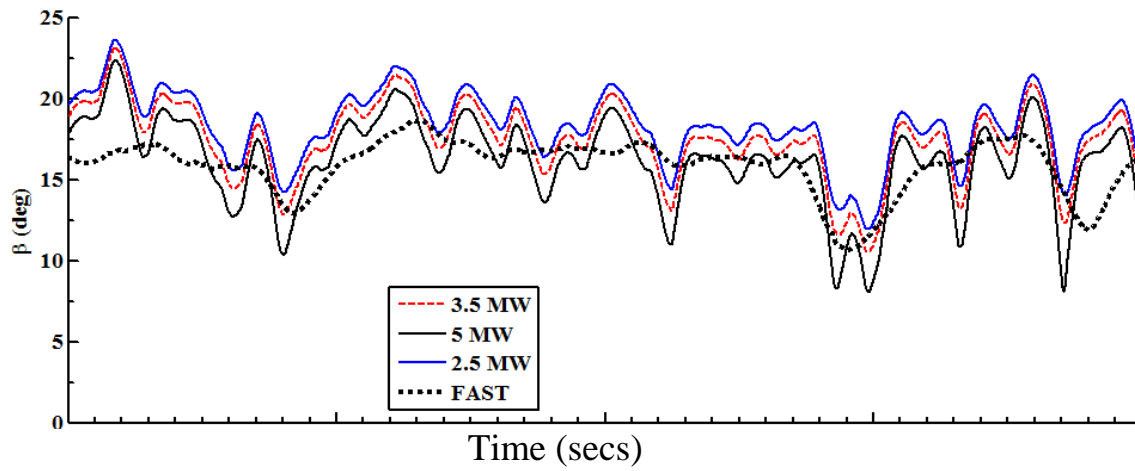


Figure 67. Pitch angle variation for various turbine power set points for a turbulent wind speed at 18ms^{-1} . The rated wind speed of NREL 5MW turbine is 12ms^{-1} .

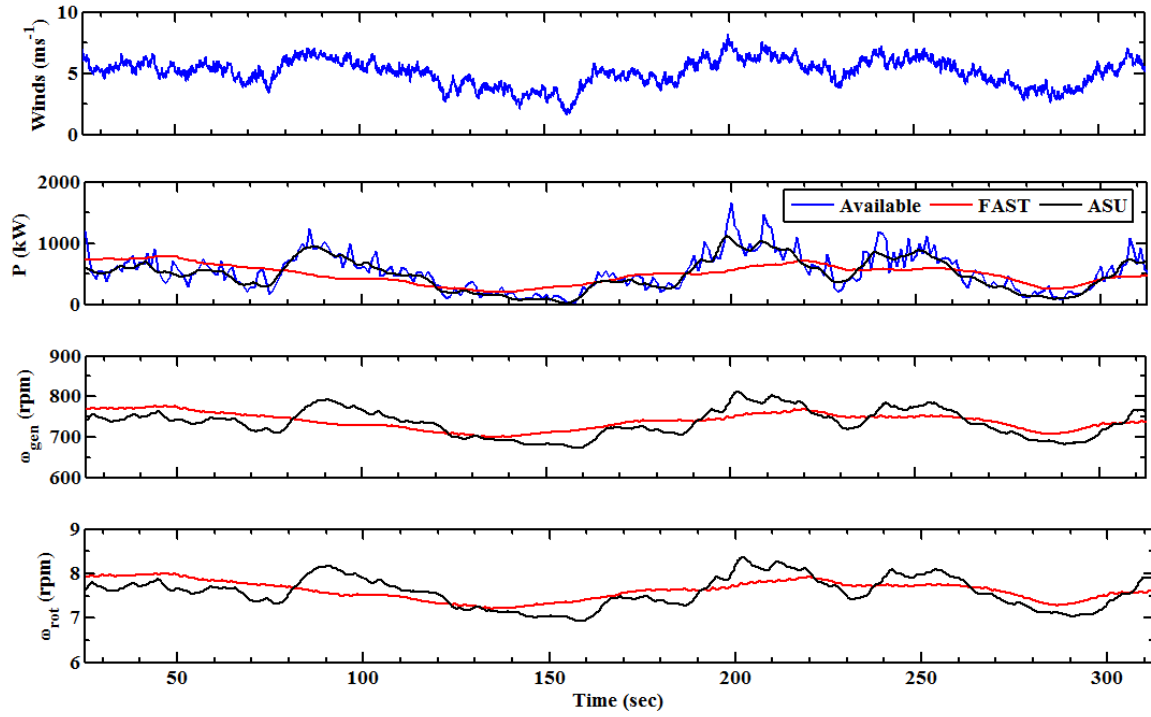


Figure 68. FAST comparison to control at 5ms^{-1} average winds (using TurbSim). The winds, power (P), generator speed (ω_{gen}) and rotor speed (ω_{rot}) are shown above.

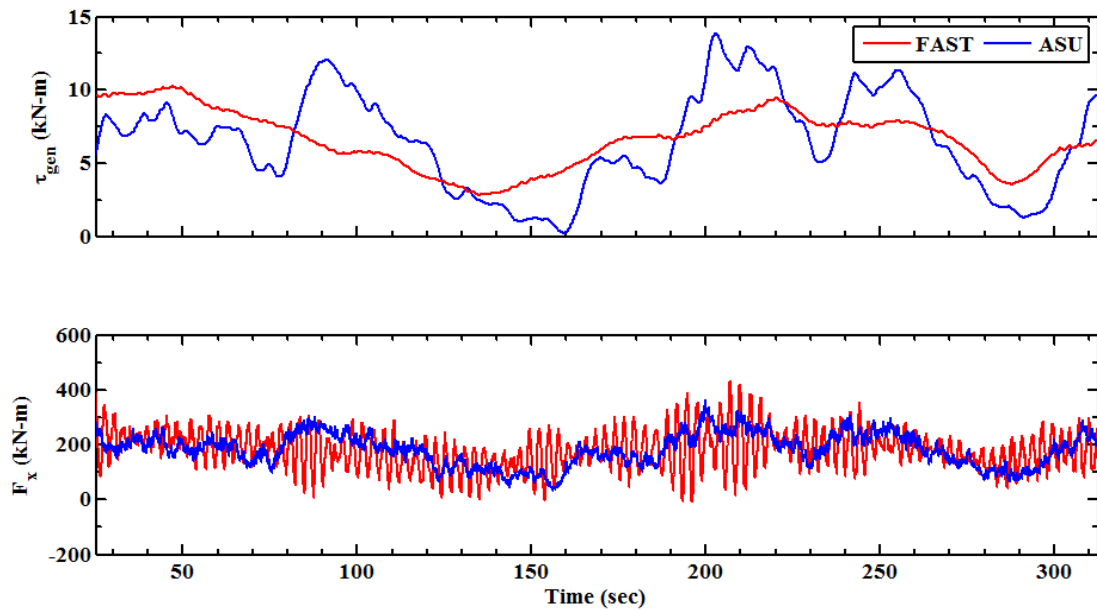


Figure 69. Forces computed using FAST and LAWF control for an average wind speed of 5ms^{-1} (shown in Figure 68 above). The generator torque (τ_{gen}) and thrust force (F_x) are compared.

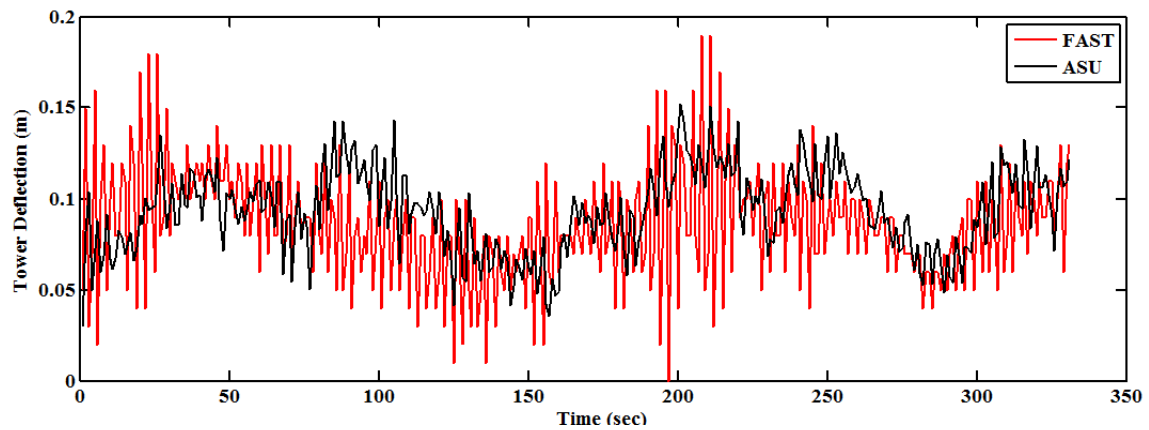


Figure 70. Tower deflection as estimated by FAST and LAWF.

A yaw controller is also developed in the LAWF controller, which uses the upwind measurements from lidar and orients the direction of the downwind turbines in the average upwind directions. The FAST does not have a yaw control in-built, therefore no comparisons could be performed. The turbine yaw control performs reasonably well compared to input upwind directions provided after accounting for wake interaction effects. The responses from the lidar were time shifted for appropriate comparison in Figure 71.

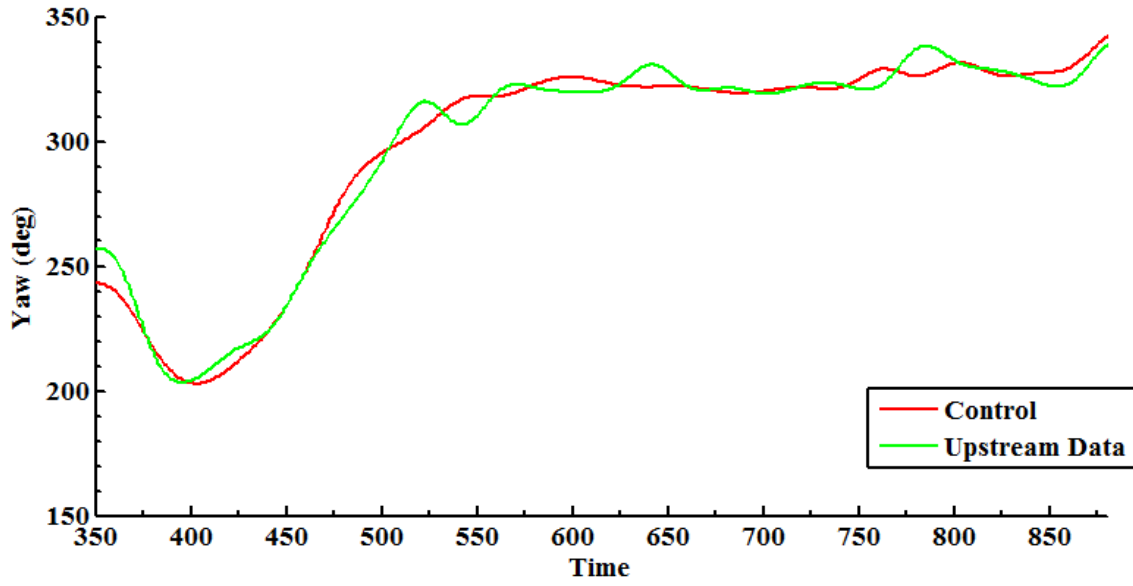


Figure 71. Yaw control results for an upwind turbine.

Further research is required for improved performance of the LAWF yaw controller. Various advanced controllers could be implemented, to understand the second and third order effects of the turbine.

8.2.2 Remote dispatch based control

The remote dispatch based control is based on providing upwind lidar measurements to the load demand operator, couple of minutes ahead of the dispatch signal to the grid, in which time the operator can schedule various other renewable energy sources and balance generators to meet the demand requirements. As shown in Figure 2, the operator schedules the power at various time-scales. Scanning Doppler lidar can provide wind speed and directions up to 15 km ahead of the wind farm (depending on atmospheric conditions at the site), which relates to a lead time of 15-20 mins for the

wind farm operator for various scheduling activities. Based on the Renewable Portfolio Standard (RPS) (IEA 2013), a certain percentage of produced power needs to be renewable (such as wind, solar, hydro). Due to high uncertainty in wind prediction models (as shown in Section 6), wind farm operators face a challenge currently with wind power scheduling, in turn results in large losses in power and revenue. As shown in Figure 2, when wind curtailment occurs, the operator schedules the power one minute ahead of distribution. With scanning Doppler lidar measurements ahead of the wind farm, the operator can improve energy scheduling processes to maximize renewable power production. The operator can provide dynamic power set-points ahead of time and optimize other renewable sources to maintain the RPS requirement.

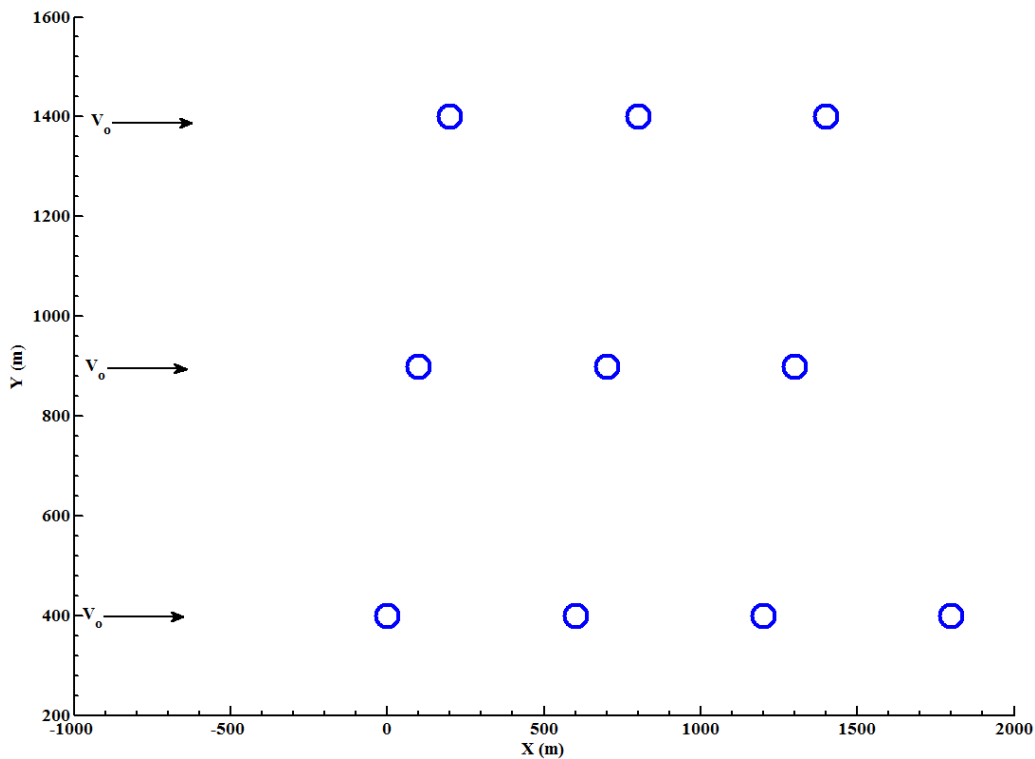


Figure 72. Wind Farm Layout Design (10 NREL 5MW wind turbines) used for analysis

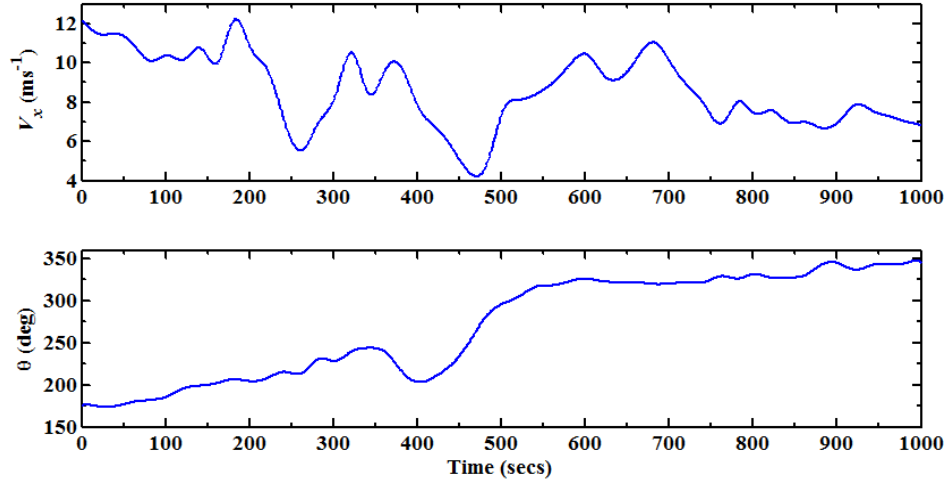


Figure 73. Average scanning Lidar winds and direction upwind of the wind farm.

The wind farm control algorithm is performed for a realistic wind farm array of 10 turbines, as shown in Figure 72. Lidar wind speed and direction input, 1 km upstream of the wind farm, are used as shown in Figure 73. Figure 74 shows the control adaptation to the demand curve provided by the operator. The available power in the wind is also shown Figure 74.

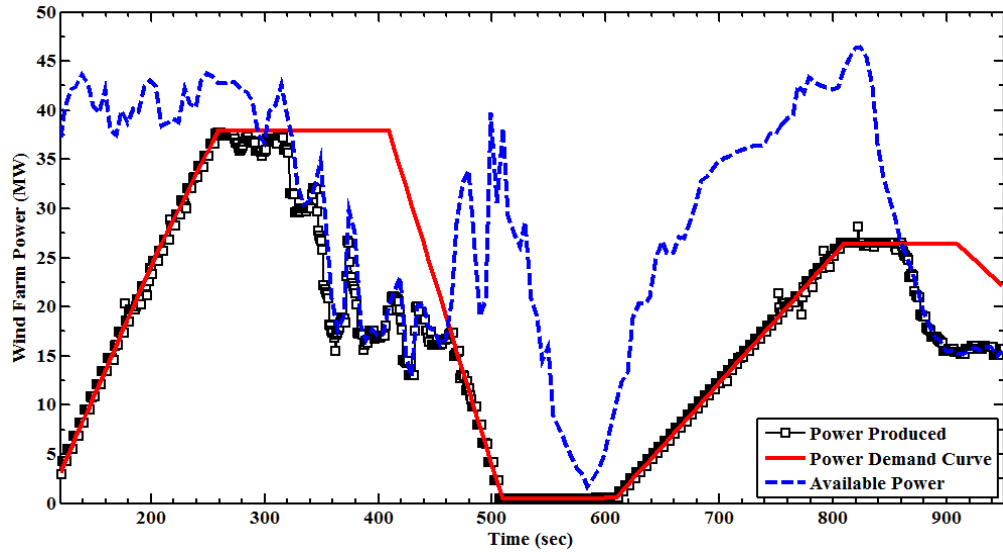


Figure 74. Demand based control. Wind farm power demand curve is shown in red, the power available is shown in dashed blue line, and the power produced is shown as the black line with square boxes.

The power demand curve shown in Figure 74 was artificially generated. As shown in Figure 74, the power produced matches the demand curve reasonably well, even though the available power at the wind farm is higher. At locations, where the demand is more than the available power, the controller is notified of possible reduction in demand power. By reducing the power set-points, the loads on the turbines are decreased, since the blades are pitched higher than required for maximum power (as shown in Figure 67).

The demand operator has the control to meet the demand and also reduce the loads on downwind turbines (affected by wakes). In this feature of the control, the operator can schedule maximum power to the upwind turbines and reduce the power set-points for the downwind turbines, in turn reducing the loads on turbines. This is done by altering the pitch angles of the downwind turbines to match the power reference provided. Figure 75 shows the power reference changes performed to meet the demand of 26 MW, by reducing the power set-points for downwind turbines and maintaining the power set-points for upwind turbines. One of the reasons for not optimizing the loads on all turbines is the uncertainty in current wake models. Wake models do not perform as expected, since it varies based on atmospheric conditions and are strongly affected by terrain. Figure 75 also shows the reduction in thrust forces of downwind turbines, compared to conventional controller where maximum power is extracted from every turbine. The demand operator can also equally distribute the load among all the turbines equally, it's based on the ratio of power available and the total demand load at the given instant. This is shown as equal power distribution curve in Figure 75.

Further improvements can be performed to the controller by real-time calculation of wake parameters (such as the wake spread constant, boundary layer height etc...) from lidar, and feeding the information as an input into the wake model. Currently, industry standard parameters are applied.

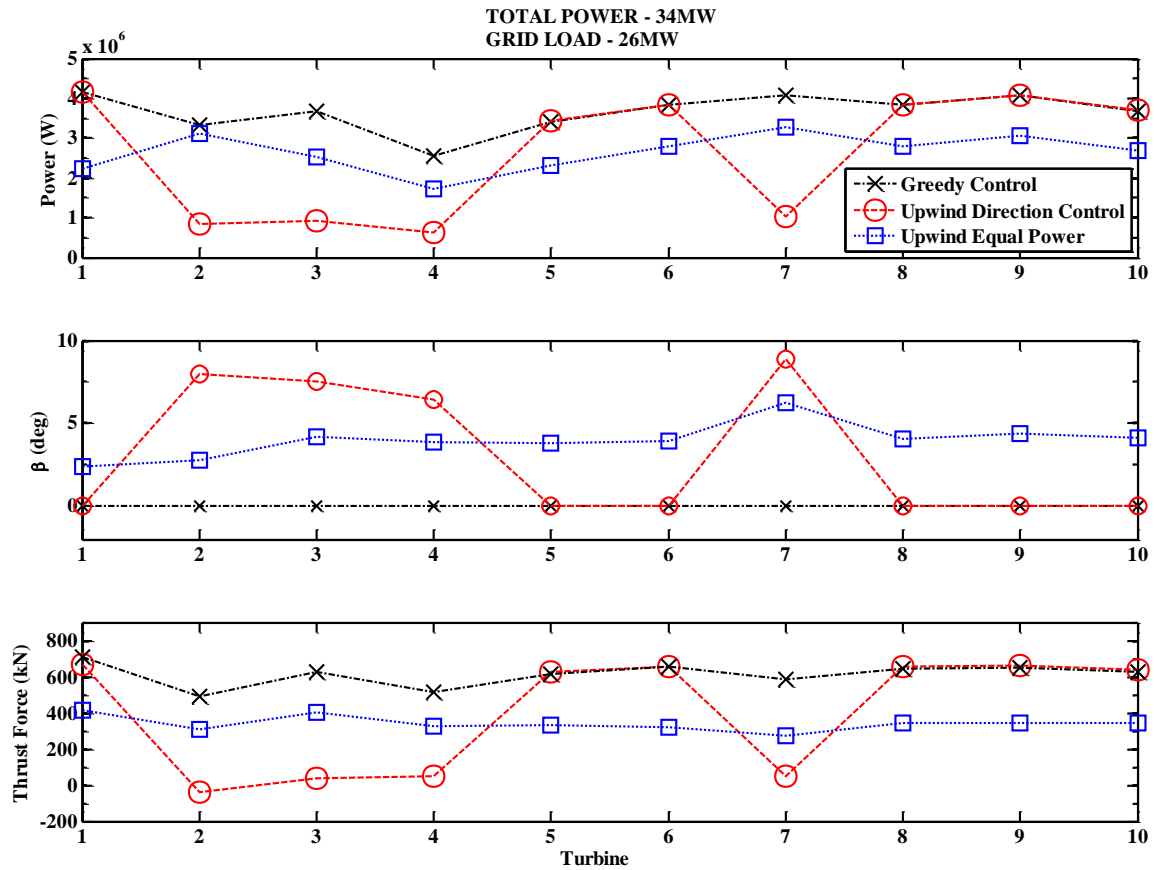


Figure 75. Various options for Demand based control. The maximum available power (“greedy control”) is shown in black line (34 MW), while direction based control and equal power distribution options are shown in red and blue respectively.

9. WIND FARM CONTROL OPTIMIZATION

9.1 Wind farm power optimization

The wind turbine controller described in above sections is based on power reference set points, as provided by the demand operator or upwind lidar measurements, and simulated wind speed at turbine locations. The power from a turbine is a function of velocity ahead of the wind turbine and coefficient of power (C_p). C_p is a function of the turbine pitch angle (β) and tip-speed ratio (λ), therefore by selecting the appropriate pitch angle and maintaining the suitable tip-speed ratio, the power at each turbine can be method to the operator set power demand, even if the turbine has the potential to produce more power. Therefore, a formulation is developed which re-calculates the C_p and C_T of each turbine based on power reference and wind speed input (Madjidian et al. 2012) as shown in Equation 58 and 59. The modified C_p^* and C_T^* coefficients are shown in Figure 76 and Figure 77.

$$C_p^*(P^{ref}, v) = C_p(\lambda(P^{ref}, v), \beta(P^{ref}, v)) \quad (58)$$

$$C_T^*(P^{ref}, v) = C_T(\lambda(P^{ref}, v), \beta(P^{ref}, v)) \quad (59)$$

Therefore by altering the C_p^* and C_T^* for each turbine, the entire wind farm power can be optimized. The power of each turbine can now be formulated as:

$$P_i = \frac{1}{2} \rho A C_p^*(P_i^{ref}, v_i) v_i^3 \quad (60)$$

The velocity deficits, as estimated by Frandsen's model, for downwind turbines can be calculated, by altering the C_T^* coefficient as shown in Equation 61 below.

$$\frac{V_{i+1}}{V_o} = 1 - \left(\frac{A_n}{A_{i+1}} \left(1 - \frac{V_i}{V_o} \right) + \frac{1}{2} \frac{A_R}{A_{i+1}} C_T^*(P_{i+1}^{ref}, v_{i+1}) \frac{V_i}{V_o} \right) \quad (61)$$

The power capture of downwind turbines can be enhanced by limiting the power extracted from upwind turbines. The optimization algorithm is to maximize the wind farm power production (as shown in Equation 62), by reducing the power reference on upwind turbines. This is expected to increase the available power to downwind turbines and hence potentially expected to increase the total wind farm power production and reduce loads on downwind turbines. Therefore, the two step procedure for optimization is given as,

Step 1: Reduce upwind turbines power references by say, X MW,

$$\text{Step 2: } P_n^{ref*} = \underset{P_n^{ref}}{\operatorname{argmax}} \sum_{i=1}^N P_i \quad (62)$$

This algorithm is looped over multiple turbines in the array, based on upwind direction. Initially all the turbines are set to capture maximum power. The optimization procedure provides maximum power reference set-points for each turbine, given the objective function of maximizing total wind farm power. The algorithm maximizes C_P and minimizes C_T , or in other words choosing the maximum power for the entire wind farm at every time step increment t . The turbine power set-points for the upwind turbines can be altered by the user, based on demand requirement.

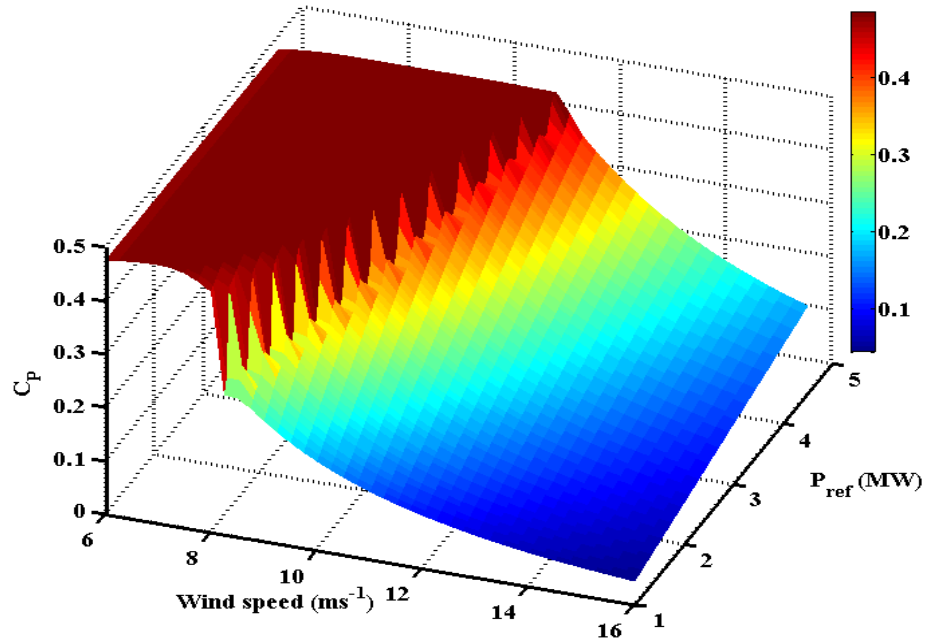


Figure 76. C_p as a function of reference power (P_{ref}) and wind speed (V). The streaks represent the non-linear part of the power curve.

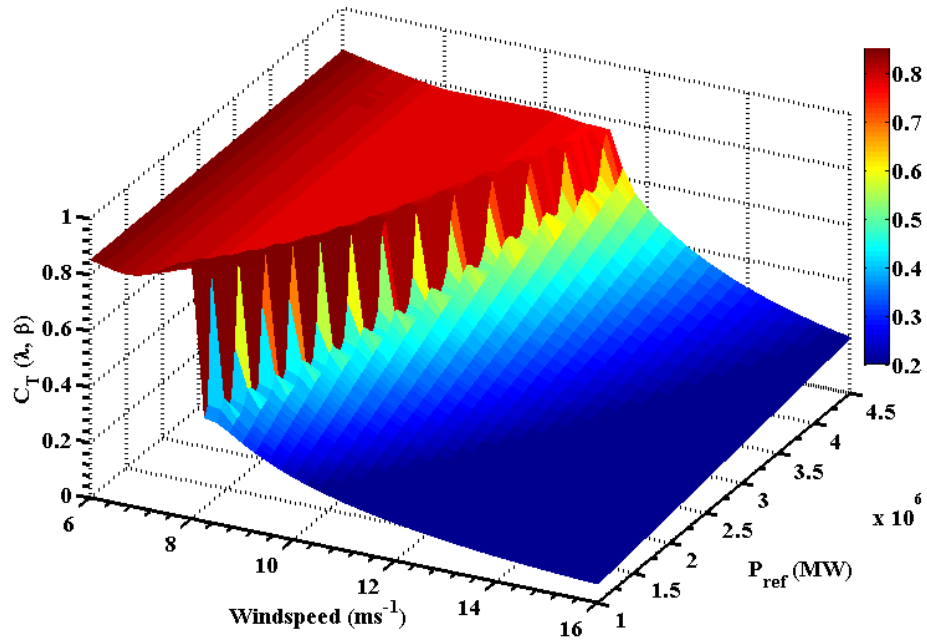


Figure 77. C_T as a function of reference power (P_{ref}) and wind speed (V). The streaks represent the non-linear part of the power curve.

9.2 Wind farm power optimization results

For the controller described above, wind farm power is based on wind speed input and the power set-points provided at each turbine location. The upwind turbines extract maximum power from the wind, and let the remaining energy to be captured by downwind turbines. Therefore, it can be hypothesized that the power extracted from downwind turbines is strongly dependent on the amount of energy extracted from the upwind turbines. An optimization algorithm has been implemented, which intentionally reduces the power set-points for the upwind turbines and increases the energy content for the downwind turbines. To prove this theory, a linear array of 10 NREL 5 MW wind turbines as shown in Figure 78 is considered, with an initial wind speed input. Wake deficits behind each turbine are estimated based on Frandsen et al. 2006.

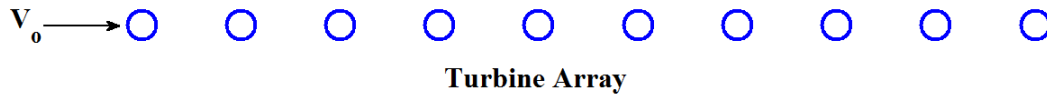


Figure 78. Sample array of 10 5MW wind turbines

As explained in Section 3, the C_P and C_T coefficients of each turbine can be altered based on the energy content extracted from each upwind turbine and the power available at the current turbine location. Since the C_P and C_T coefficients can be reformulated based on reference power and wind speed (as shown in Section 3 and Figure 76 & Figure 77), optimum power and thrust coefficients can be extracted, for increased farm power based on a nonlinear optimization algorithm in MATLAB[®]. Results from three cases for a mean wind speed input of 11ms^{-1} are shown below: a) Maximum Power

– each turbine extracts maximum possible power available at each location or “greedy” control, b) Optimized Power – the reference power for the first turbine is reduced by 0.5 MW, and the increased energy available for the downwind turbines is optimized for increase in total farm power, c) Reduced P_{ref1} – the reference power for the first turbine is reduced by 0.5MW, but the power reference for the downwind turbines is set equal to the power attained from the Maximum Power scenario. This shows the amount of available power present in the downwind turbine locations, for reduced power set-points than available power at downwind turbine locations. Figure 79 shows the increase in velocity, power and reduction in thrust coefficients compared to “greedy” control. The effect of reducing the power set-points for the upwind turbines has a two pronged effect, a) more available power for downwind turbines and b) reduced structural loading on downwind turbines. Therefore, by maximizing the wind farm power and reducing structural loading, an optimum can be obtained which improves wind farm efficiency. Figure 80 shows the results from the optimization algorithm.

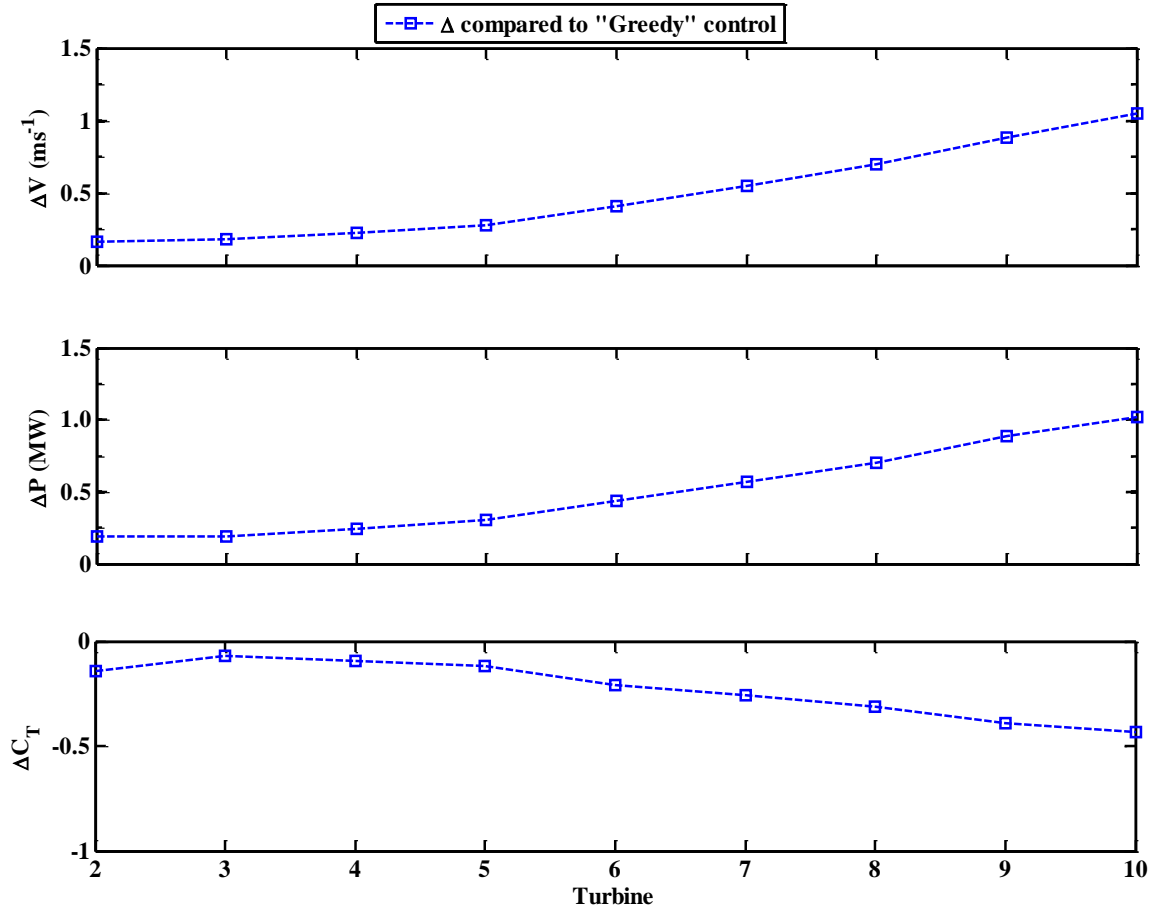


Figure 79. The increase in velocity, power and reduction of thrust coefficients at downwind turbines compared to “greedy” control, due to reduced power reference at the turbine 1 by 0.5 MW.

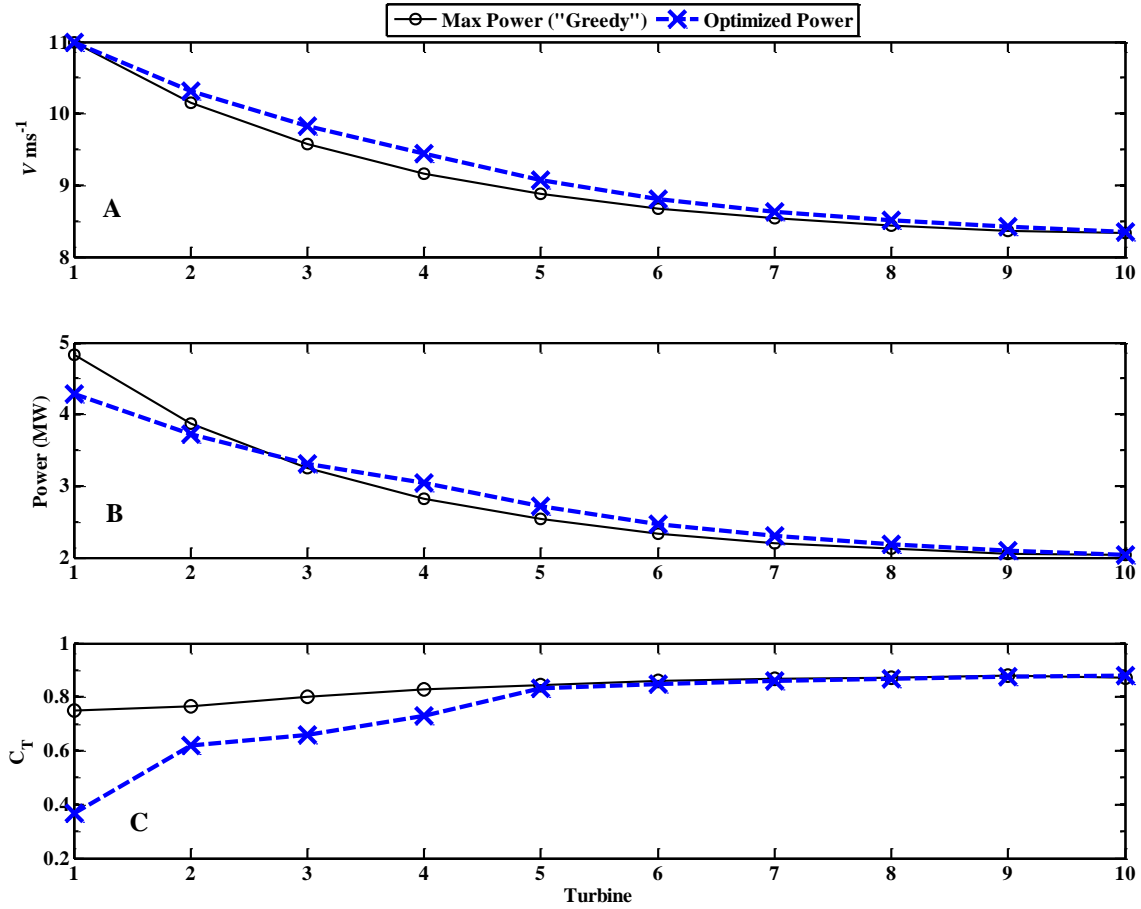


Figure 80. A) Velocity at each turbine for a linear array of 10 5MW wind turbines at an input wind speed of 11 ms^{-1} . The blue curve represents the optimized power after reducing the first turbine power set-point by 0.5MW and matching other turbines power reference set points to previous maximum power control ("greedy control"). B) Power output for a linear array of turbines at input wind speed of 11 ms^{-1} . C) Coefficient of thrust (C_T) for a linear array of turbines at input wind speed of 11 ms^{-1} .

The effect of reducing the power reference on upwind turbine is further analyzed.

Figure 81 shows the increase in power of downwind turbines for various scenarios by decreasing the upwind power reference. Figure 82 shows the reduction in the coefficient of thrust on downwind turbines for various scenarios. The optimized power not only increases the power of the entire farm, but also minimizes the loads on turbines. It can be observed that, the thrust coefficients reduce considerably when the power reference of the

upwind turbine was reduced by 1 MW. Table 17 and Table 18 show the % changes of power and thrust coefficients for various upwind power reference values. As shown in the tables above, the downwind turbines power increases with increase in reduction of P_{ref1} of upwind turbines, simultaneously the downwind turbines thrust reduces with increased reduction of P_{ref1} of upwind turbines. Although significant increase in power for the downwind turbines is observed, total wind farm power increases by around 1%.

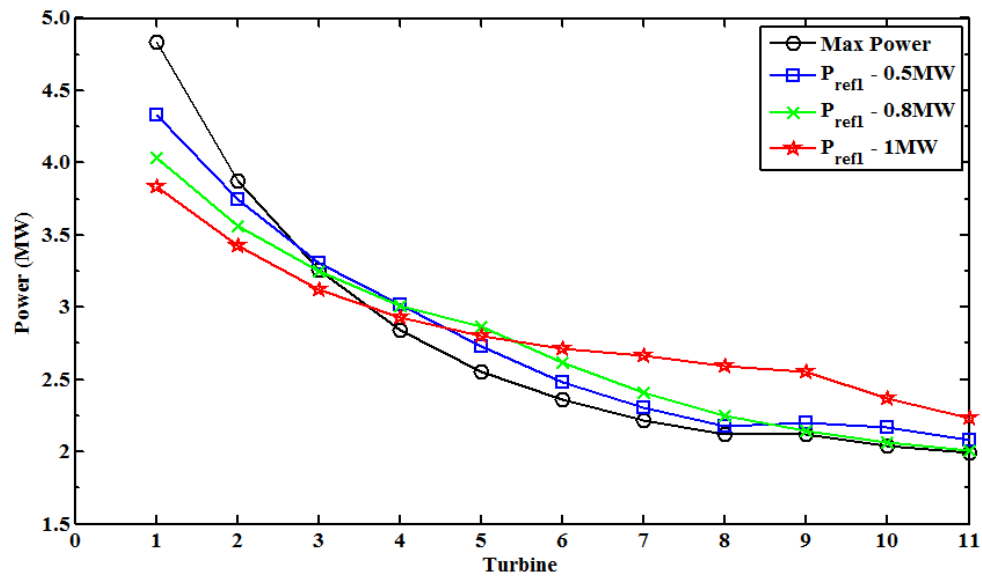


Figure 81. Power effect of reducing power reference of upwind turbines on downwind turbines at input wind speed of 11 ms^{-1} . Maximum power control (“greedy”) is also shown.

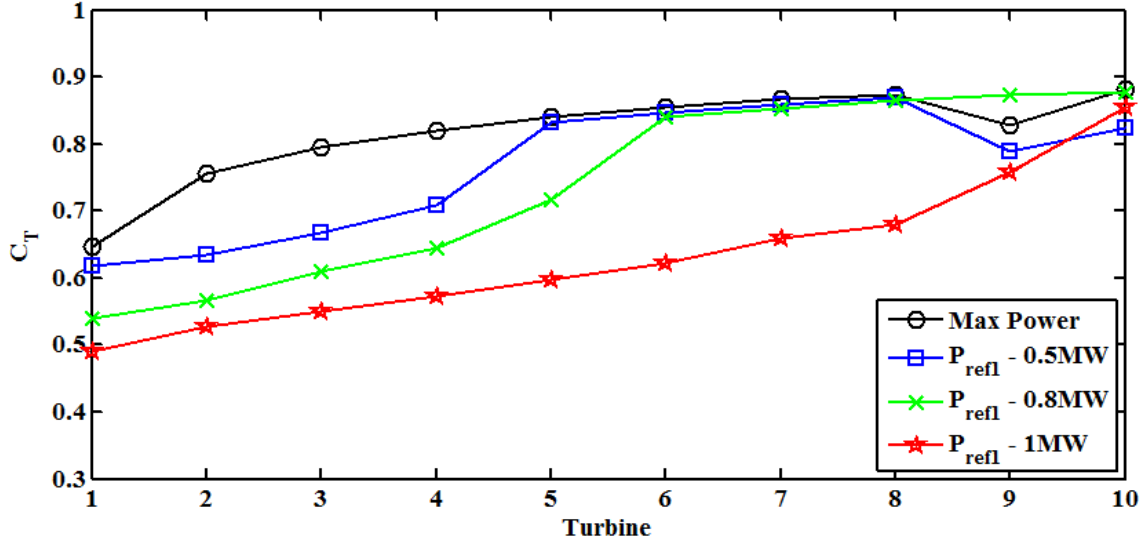


Figure 82. Thrust effect of reducing power reference of upwind turbines on downwind turbines at input wind speed of 11 ms^{-1} .

Table 17. Average power increase in downwind turbines for various upwind reference powers and input wind speed of 11 ms^{-1} .

Upwind P_{refl} Reduction (MW)	% Increase in Downwind Turbines	% Increase in Total Wind Farm
0.5	3.07	0.86
0.8	3.58	0.13
1.0	5.14	0.71

Table 18. Average thrust coefficient reduction in downwind turbines for various upwind reference powers and input wind speed of 11 ms^{-1} .

Upwind P_{refl} Reduction (MW)	% Decrease
0.5	4.06
0.8	6.13
1.0	10.51

To account for turbine interaction in multiple rows and wind direction effects, a wind farm layout as shown in Figure 72 is used to understand array effects. Figure 73 shows the average lidar winds and direction upwind of the wind farm. This is real processed scanning lidar data from a wind farm development site in USA. Rapid changes in direction and wind speed were observed during the time frame. Figure 83 shows the power output for the layout from winds and direction shown in Figure 73. Lidar winds are extracted 1 km ahead of the wind farm and the power output, accounting for wake interaction effects are shown as a red curve in Figure 83. Wind evolution model (i.e., Mann Spectral Model) was applied to the lidar data 1 km ahead of the wind farm at every upwind turbine location and a dynamic delay parameter, based on wind speed at every time step was used to propagate the wind field. The wind farm control power is based on maximum power extraction of upwind turbines, while the optimized power shows the wind farm power based on the optimization algorithm discussed above. The reference power was reduced for upwind turbines, in cases where it affects multiple downwind turbines, by 0.1 MW. This results in a 0.5% increase in total wind farm power, for this scenario. A further reduction in upwind power reference resulted in reduction of power compared to maximum power (“greedy” power) and drastic thrust/loads on the turbines. Therefore, depending on the requirement of the load demand operator, a balance between power maximization and load reduction can be chosen. This concept needs to be validated based on data at a real lidar wind farm site, with SCADA data of individual wind turbines at the site.

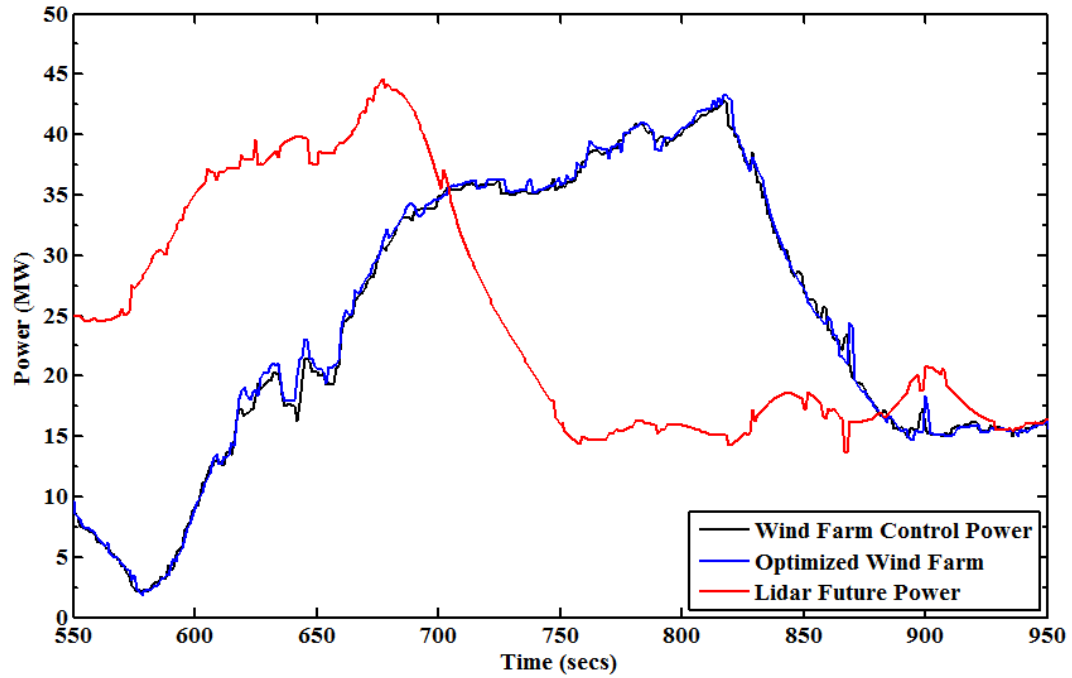


Figure 83. Wind farm power output for the winds and direction shown in Figure 73. Lidar wake induced wind farm power 1 km ahead of the wind farm is also shown. The optimized power algorithm was performed, when multiple downwind turbines are affected by upwind turbine performance.

10. SUMMARY

A Doppler lidar was used to obtain radial velocities over multiple wind farm domains. Mean wind speeds were obtained on a terrain-following surface at hub-height. The wind speed distributions were shown to be obtainable with reasonable accuracy with the given algorithms. For site1, the wind speed distribution was shown to vary significantly with spatial location. Therefore, a key result of this study is that (spatially varying) mean wind speeds and their distributions can be *measured* from one central location in the wind farm – although an important caveat is that more experimental data is required to fully define and understand the error structure of the products, particularly in the regions of the domain perpendicular to the mean wind. Field experiments which also deploy instruments capable of measuring winds and their distributions at multiple heights in the off-mean-wind direction would be a valuable next step for validating scanning Doppler lidar products for wind energy. As a demonstration, an example wind farm layout, based on global optimization and simple algorithms, was designed to maximize power subject to several constraints (wake interaction, domain size etc). 3D Doppler lidar data can be used to produce "layered" wind and power estimates, accounting for wind variations at different elevations of the rotor-swept area. Future work will focus on control of turbines in a wind farm with lidar measurements.

Doppler Lidar and tower measurements from a wind farm development project have been compared with mesoscale modeling predictions from COAMPS. A key aspect of this study is the inter-comparison of spatially resolved wind maps on wind farm domains. COAMPS under-predicted wind speed estimates over much of the wind farm domain. Although mean wind and direction estimates were forecasted reasonably well,

abrupt changes in wind direction were not captured as well. Wind speed correlations (30 minute averaged) of approximately 40% and directional correlations of 22% were observed between the lidar and model. Spatial monthly averaged wind speed and power differences between lidar and COAMPS estimates showed significant spatial differences. Modeled wind speed distributions showed a bias of 1-2 m s⁻¹ for much of the wind farm area (in comparison with tower and lidar distributions, which closely agree). After bias correction, the wind speed differences were reduced by almost 70% for most of the domain. Spatial analysis of differences between lidar and model results (after bias correction) revealed larger wind speed deviations at some locations where wind speeds were initially over-predicted by simulations. Therefore, although an aggregate monthly bias correction improves wind estimates at most locations, particular regions of the domain were degraded by the bias correction. Complex terrain likely makes simple bias correction more challenging. Several ramp events estimated by lidar were not well captured by the numerical model predictions - with issues with both magnitude and timing of the ramp events. This paper presents a methodology to systematically evaluate nested mesoscale model forecast results using spatially distributed measurements obtained with scanning Doppler lidar. In order to produce wind products of sufficient accuracy to inform commercial wind resource assessments or high-value short-term forecasts for wind farm domains, even well-established mesoscale models with relatively fine inner nest resolutions (333 m) may benefit from further comparisons with (or assimilation of) spatially distributed Doppler lidar data. Improper mesoscale model run could result in large economic losses and inappropriate wind farm characterization.

Coherent Doppler lidar for wind farm control developed in this thesis could be a valuable tool for wind farm developers and wind farm demand operators. The control provides accurate wind speed and direction data ahead of wind farm power scheduling operations and improves the performance of the wind farm by coordinating wind turbines. Measuring the spatial energy content of the wind ahead of the wind farm, provides the demand operator <15 minutes of time to improve wind farm performance and optimize balance generators to maintain grid demand. The controller developed also calculates the first-order load effects of individual turbines for assessing the effect of tower vibrations, generator performance, drive train and aerodynamic loads. The controller accounts for wind farm wake interaction effects, but turbulence is not included in the model, which could be valuable to assess the loads on individual turbines. The wind farm optimization algorithm increases the total wind farm power by 1%, and reduces the thrust forces by 4%. This theory needs to be validated in a field study. Finally the value proposition of coherent Doppler lidar for wind farm assessment and control resulted in a ROI of 1200% for a dual-Doppler lidar and ~1000% for a single Doppler lidar. Therefore, a lidar for wind resource assessment could prove valuable for improving wind farm financing.

Future research could potentially include, turbulence, turbine effects on the entire rotor swept area, accounting for wind shear and directional shear ahead of the wind farm. Knowledge of these events ahead of the wind farm, using lidar, could further optimize wind farm performance.

JOURNAL ARTICLES FROM CURRENT RESEARCH

J1. R Krishnamurthy, R Calhoun, and H Fernando, 2009:” Large-eddy simulation based retrieval of dissipation from Coherent Doppler lidar”, *Boundary layer meteorology*, 136, 1, 45-57

J2. R. Krishnamurthy, R. Calhoun, B. Billings, and J. Doyle, 2010: “Wind Turbulence Estimates in a Valley by Coherent Doppler Lidar”, *Meteorological Applications*, 18: 361–371. doi: 10.1002/met.263.

J3. R. Krishnamurthy, A. Choukulkar, R. Calhoun, J. Fine, A. Oliver, and K. Barr, 2012: “Coherent Doppler Lidar for Wind Farm Characterization”, *Wind Energy*, doi: 10.1002/we.539.

J4. R Krishnamurthy, R Calhoun, B Billings, J Doyle, 2013: “Mesoscale Model Evaluation with Scanning Doppler Lidar for Wind Farm Assessment”. *Remote sensing letters*. (Accepted). 4: 6, 579-588. doi: 10.1080/2150704X.2013.769285

J5. R Barthelmie, S Pryor, C Smith, H Wang, R Krishnamurthy, R Calhoun, & N Capaldo, 2013: “3D wind and turbulence characteristics of the atmospheric boundary-layer”, *Bulletin of American Meteorological Society* (Abstract Accepted).

In Preparation:

J6. R Krishnamurthy, R Calhoun (2013): “Wind Farm Control using 3D coherent Doppler Lidar”. In Preparation

J7. R Krishnamurthy, R Calhoun et al. (2013): “Dual-Doppler scanning lidars for wind resource assessment”. In Preparation

Conferences

C7. K Barr, D McReavy, J Sharp, D Wolfe, R Krishnamurthy, R Calhoun (2013). “Comparing WindTracer Long Range Scanning Lidar data to In-situ Anemometry and Vertical Lidars “, AWEA WindPower, Chicago, USA.

C6. R Krishnamurthy, A Choukulkar, R Calhoun, G Poulos, & K Barr (2012). “Multiple Three-Dimensional Scanning Doppler Lidars and Wind Resource Assessment”, AWEA Wind Resource Assessment Conf., Pittsburgh, PA. [Invited]

C5. Barthelmie, Pryor, Smith, Crippa, Wang, R. Krishnamurthy, Calhoun, Valyou, Marzocca, Matthiesen & Capaldo (2012). “An integrated approach to offshore wind energy assessment: Great Lakes 3D Wind Experiment. Part I. Calibration and testing”. AWEA Offshore Windpower Conf., Virginia beach, VA, USA. (Poster)

C4. R Calhoun, R Krishnamurthy, A Choukulkar & K Barr (2012). “Wind Farm Assessment using Coherent Doppler lidar”, ISARS Conf., CO, USA.

C3. R Krishnamurthy, R Calhoun, B Billings, J Doyle (2012). “Evaluation of Mesoscale model with Coherent Doppler lidar for Wind Farm assessment”, Texas Tech Univ. Symp., Texas, USA

C2. R Krishnamurthy, Choukulkar, Calhoun, Sutton, Yu, Jeanneret (2010). “Coherent Doppler lidar for wind farm characterization”, CWE Conf., North Carolina, USA

C1. R. Krishnamurthy, R. Calhoun, H. Fernando, G. Poulos, 2007: “Measurements of Turbulence Parameters and Dissipation in Complex Terrain”, 12th Conference on Mesoscale processes, 6-9, August, NH.

REFERENCES

1. Ainslie, J. F. (1988). Calculating the flowfield in the wake of wind turbines. *Journal of Wind Engineering and Industrial Aerodynamics*, 27(1), 213-224.
2. Allard, R. A., Campbell, T. J., Smith, T. A., Jensen, T. G., Cummings, J. A., Chen, S., ... & Carroll, S. N. (2010). Validation Test Report for the Coupled Ocean/Atmosphere Mesoscale Prediction System (COAMPS) Version 5.0 (No. NRL/MR/7320--10-9283). NAVAL RESEARCH LAB STENNIS SPACE CENTER MS OCEANOGRAPHY DIV.
3. Amar FB, Elamouri M, Dhifaoui R. Energy assessment of the first wind farm section of Sidi Daoud, Tunisia. *Renewable Energy* 2008; **33**: 2311-2321.
4. Archer, C. L. and M. Z. Jacobson, 2005: Evaluation of global windpower. *J. Geophys. Res.-Atm.*, 110, D12110, doi:10.1029/2004JD005462.
5. AWEA, <http://www.awea.org>, 2010.
6. Banta RM, Newsom RK, Lundquist JK, Pichugina YL, Coulter RL, and Mahrt L, Nocturnal lowlevel jet characteristics over Kansas during CASES-99. *Boundary-Layer Meteorology* 2002; **105**: 221-252.
7. Banta RM, Pichugina YL, Kelley ND, Jonkman B, and Brewer WA. Doppler lidar measurements of the Great Plains low-level jet: Applications to wind energy. 14th International Symposium for the advancement of Boundary Layer Remote Sensing 2008.
8. Barthelmie R, Folkerts L, Larsen G, Pryor SC, Frandsen ST and Schepers G. Comparison of wake model simulations with offshore wind turbine wake profiles measured by sodar, *Journal of Atmospheric and Oceanic Technology*, 2006; **23**(7), 888-901.
9. Barthelmie, R, S Pryor, C Smith, P Crippa, , H Wang, R. Krishnamurthy, R Calhoun, Valyou, Marzocca, Matthiesen & N Capaldo, 2012: “*An integrated approach to offshore wind energy assessment: Great Lakes 3D Wind Experiment. Part I.*”

Calibration and testing”. AWEA Offshore Windpower Conf., Virginia beach, VA, USA.

10. Barthelmie, R. J., B. Grisogono, and S. C. Pryor (1996), Observations and simulations of diurnal cycles of near-surface wind speeds over land and sea, *J. Geophys. Res.*, 101(D16), 21,327–21,337, doi:10.1029/96JD01520.
11. Barthelmie R J and L. E. Jensen, “Evaluation of wind farm efficiency and wind turbine wakes at the Nysted offshore wind farm,” *Wind Energy*, vol. 13, no. 6, pp. 573–586, 2010.
12. Belu R, Koracin D. Wind Characteristics and wind energy potential in western Nevada. *Renewable Energy* 2009; **34**: 2246-2251.
13. Betz, A. 1926. Wind Energy and its Exploitation by Windmills. Gottingen: Vandenhoeck & Ruprecht. 64 pp. (In German)
14. Belsley, D.A., E Kuh, and R.E., Welsh (1980). Regression Diagnostics; Identifying Influential Data and Sources of Collinearity. John Wiley and Sons, 292 pp.
15. Bingöl F, Mann J, Larsen GC. Light Detection and Ranging Measurements of Wake Dynamics Part I: One-dimensional scanning. *Wind Energy* 2010; **13**: 51-61.
16. Boccippio D J. A diagnostic analysis of the VVP single-Doppler retrieval technique . *Journal of Atmospheric and Oceanic Technology* 1995; **12**: 230–248.
17. Bossanyi E, “Individual blade pitch control for load reduction,” *Wind Energy*, vol. 6, no. 2, pp. 119 – 128, 2003.
18. Bossanyi, E., Savini, B., Iribas, M., Hau, M., Fischer, B., Schlipf, D., & Carcangiu, C. E. (2012). Advanced controller research for multi-MW wind turbines in the UPWIND project. *Wind Energy*.
19. Browning KA, Wexler R. The determination of kinematic properties of a wind field using Doppler radar. *Journal of Applied Meteorology* 1968; **7**: 105–113.

20. Burton, T., D. Sharpe, N. Jenkins, and E. Bossanyi, Wind Energy Handbook. John Wiley and Sons, 2001.
21. Calhoun R, Heap R, Princevac M, Newsom R, Fernando H, and Ligon D. Virtual towers using coherent Doppler lidar during the Joint Urban 2003 Experiment. *Journal of Applied Meteorology* 2006; **45**: 1116-1126.
22. Chan PW, Shao AM. Depiction of Complex Airflow Near Hong Kong International Airport Using a Doppler LIDAR with a Two-dimensional Wind Retrieval Technique. *Meteorologische Zeitschrift* 2007; **16**: 491-504.
23. Chin S H-N, Glascoe L, Lundquist J, Wharton S, 2010: Impact of WRF physics and grid resolution on low-level wind prediction: Towards the assessment of climate change impact on future wind energy, Fifth international symposium on computational wind engineering, Chapel Hill, North Carolina, USA.
24. Choukulkar A., Calhoun R., Billings B., Doyle J. (2011): Investigation of a complex nocturnal flow in Owens Valley using lidar and COAMPS. *Boundary Layer Meteorology*, Accepted.
25. Darby, L. S., R. M. Banta, and R. A. Pielke, 2002: Comparisons between mesoscale model terrain sensitivity studies and Doppler lidar measurements of the sea breeze at Monterey Bay. *Mon. Wea. Rev.*, **130**, 2813–2838.
26. Deshpande, A. S., & Peters, R. R. (2012, July). Wind turbine controller design considerations for improved wind farm level curtailment tracking. In *Power and Energy Society General Meeting, 2012 IEEE* (pp. 1-6). IEEE.
27. Doviak RJ, and Zrnic´ DS. *Doppler Radar and Weather Observations*. Academic Press. 1993; 2 edition 304 pp.
28. Drechsel S, Chong M, Mayr G, Weissmann M, Calhoun R, and Dörnbrack A. Three-dimensional wind retrieval: application of MUSCAT to dual Doppler lidar. *Journal of Atmospheric and Oceanic Technology* 2009; **26**: 3, 635-646.

29. Dvorak, M. J., C. L. Archer, and M. Z. Jacobson, 2010: California offshore wind energy potential. *Renewable Energy*, doi:10.1016/j.renene.2009.11.022.
30. Fast, Jerome D., Lisa S. Darby, 2004: An Evaluation of Mesoscale Model Predictions of Down-Valley and Canyon Flows and Their Consequences Using Doppler Lidar Measurements during VTMX 2000. *J. Appl. Meteor.*, **43**, 420–436.
31. Frandsen, S., Barthelmie, R., Pryor, S., Rathmann, O., Larsen, S., Højstrup, J., & Thøgersen, M. (2006). Analytical modelling of wind speed deficit in large offshore wind farms. *Wind Energy*, 9(1-2), 39-53.
32. Frehlich R, Hannon S, and Henderson S. Coherent Doppler Lidar Measurements of Wind Field Statistics. *Boundary-Layer Meteorology* 1998; **86**: 233-256.
33. Gal-chen T, Xu M, Eberhard W. Estimations of atmospheric boundary layer fluxes and other turbulence parameters from Doppler lidar data. *Journal of Geophysical Research* 1992; **97**: 409-418.
34. Hannon SM, Barr K, Novotny J, Bass J, Oliver A and Anderson M. Large scale wind resource mapping using a state-of-the-art 3-D scanning lidar. *European Wind Energy Conference*, 2008.
35. Henderson SW, Hale CP, Magee JR, Kavaya MJ, and Huffaker AV. Eye-safe coherent laser radar system at 2.1 μm using Tm, Ho:YAG lasers. *Optics Letters* 1991; **16**: 773–775.
36. Henderson SW, Suni PJM, Hale CP, Hannon SM, Magee JR, Bruns DL, and Yuen EH. Coherent laser radar at 2 μm using solid-state lasers. *IEEE Transactions of Geoscience and Remote Sensing Society* 1993; **31**: 1, 4–15.
37. Hill M, Calhoun R, Fernando H, Wieser A, Dörnbrack A, Weissmann M, Mayr G, and Newsom R. Coplanar Doppler Lidar Retrieval of Rotors from T-REX. *Journal of the Atmospheric Sciences* 2010; **67**: 3, 713–729.

38. Hodur RM. 1997. The Naval Research Laboratory's Coupled Ocean/Atmosphere Mesoscale Prediction System (COAMPS). *Monthly Weather Review* **125**: 1414-1430.
39. Jensen, N. O. (1983). *A note on wind generator interaction*.
40. Jiang, Q., J. D. Doyle, T. Haack, M. J. Dvorak, C. L. Archer, and M. Z. Jacobson (2008), Exploring wind energy potential off the California coast, *Geophys. Res. Lett.*, **35**, L20819, doi:10.1029/2008GL034674.
41. Jimenez, B., F. Durante, B. Lange, T. Kreutzer, and J. Tambke, 2007: Offshore wind resource assessment with WAsP and MM5: comparative study for the German Bight. *Wind Energy*, **10**, 121–134.
42. Johnson, K and N. Thomas, "Wind farm control: Addressing the aerodynamic interaction among wind turbines," in Proceedings of the American Control Conference, June 2009, pp. 2104–2109.
43. Jonkman, J. M., Butterfield, S., Musial, W., & Scott, G. (2009). *Definition of a 5-MW reference wind turbine for offshore system development*. National Renewable Energy Laboratory.
44. Kamath C, (2010). "Using simple statistical analysis of historical data to understand wind ramp events," LLNL Technical report LLNL-TR-423242.
45. Käsler Y, Rahm S, Simmet R, Kühn M. Wake Measurements of a Multi-MW Wind Turbine with Coherent Long-Range Pulsed Doppler Wind Lidar. *Journal of Atmospheric and Oceanic Technology*, 2010; **27**: 9, 1529-1532
46. Kongara S, Calhoun R, Choukulkar A, and Boldi M. Velocity retrieval for coherent Doppler lidar. *International Journal of Remote Sensing*. 2012.
47. Koscienny, A. J., R.J. Doviak and R. Rabin (1982). Statistical considerations in the estimation of divergence from single-Doppler radar and application to prestorm boundary-layer observations. *J. Appl. Meteor.*, **21**, 197-210.

48. Krishnamurthy, R., Calhoun, R., & Fernando, H. (2010). Large-Eddy Simulation-Based Retrieval of Dissipation from Coherent Doppler Lidar Data. *Boundary-Layer Meteorology*, 136(1), 45-57.
49. Krishnamurthy R, Choukulkar A, Calhoun R, Fine J, Oliver A, Barr K. Coherent Doppler Lidar for Wind Farm Characterization, Wind Energy 2012; doi: 10.1002/we.539
50. Krishnamurthy, R., Calhoun, R., Billings, B. and Doyle, J. (2011), Wind turbulence estimates in a valley by coherent Doppler lidar. *Meteorological Applications*, 18: 361–371. doi: 10.1002/met.263
51. Krishnamurthy, R., Calhoun, R., Billings, B., Doyle, J., Oliver, A. (2013), Mesoscale model Evaluation with Coherent Doppler Lidar for Wind Farm Assessment. *Remote Sensing Letters* 4: 6, Pg 579-588.
52. Kristalny, M and D. Madjidian, “Decentralized feedforward control of wind farms: prospects and open problems,” in Proceedings of the Joint IEEE Conference on Decision and Control and European Control Conference, Dec. 2011.
53. Kusiak Andrew, Song, Z. Design of wind farm layout for maximum wind energy capture, Wind Energy, 2010, 35, 685-694.
54. Lackner, M. A., Rogers, A. L., & Manwell, J. F. (2007). Uncertainty analysis in wind resource assessment and wind energy production estimation. In *45th AIAA Aerospace Sciences Meeting and Exhibit*, AIAA-2007-1222.
55. Laks, Jason, et al. "The use of preview wind measurements for blade pitch control." *Mechatronics* 21.4 (2011): 668-681.
56. Laks JH, Pao LY, and Wright A. Control of wind turbines: Past, present, and future. In *Proceedings of American Control Conference* 2009; St. Louis, MO.
57. Larsen, G. C., Madsen, H. A., Thomsen, K., & Larsen, T. J. (2008). Wake meandering: a pragmatic approach. *Wind Energy*, 11(4), 377-395.

58. Lin C, Xia Q, Calhoun R. Retrieval of urban boundary layer structures from Doppler lidar data. Part II: Proper orthogonal decomposition. *Journal of Atmospheric Sciences* 2008; **65**: 1, 21-42.

59. Mann, J. (1998). Wind field simulation. *Probabilistic engineering mechanics*, 13(4), 269-282.

60. Manwell JF, McGowan JG and Rogers AL *Wind energy explained: theory, design and application*, John Wiley & Sons, London, 2009.

61. Mellor G L and Yamada T. 1982. Development of a turbulent closure model for geophysical fluid problems. *Reviews of Geophysics and Space Physics* **20**: 851-875.

62. Mikkelsen T, Mann J and Courtney M. Windscanner: A full-scale Laser Facility for Wind and Turbulence Measurements around large Wind Turbines. *European Wind Energy Conference* 2008; Brussels (BE), 31 March - 3 April.

63. Mikkelsen, T., N. Angelou, K. Hansen, M. Sjöholm, M. Harris, C. Slinger, P. Hadley, R. Scullion, G. Ellis, and G. Vives. "A spinner-integrated wind lidar for enhanced wind turbine control." *Wind Energy* (2012).

64. Newsom R, Ligon D, Calhoun R, Heap R, Cregan E, Princevac M. Retrieval of microscale wind and temperature fields from single- and dual-Doppler lidar data. *Journal of Applied Meteorology* 2005; **44**: 9, 1324-1345.

65. Newsom R, Calhoun R, Ligon R, Allwine J. Linearly organized turbulence structures observed over a suburban area by dual-Doppler lidar. *Boundary-Layer Meteorology* 2008; **127**: 1, 111-130.

66. Oberhettinger, F. "Hypergeometric Functions." *Handbook of Mathematical Functions with Formulas, Graphs, and Mathematical Tables*. (M. Abramowitz and I. A. Stegun, eds.). New York: Dover, 1972.

67. Parks, K., Wan YH, Wiener G, Liu Y, 2011: Wind Energy Forecasting. NREL Report.

68. Pao, L and K. Johnson, "Control of wind turbines: Approaches, challenges, and recent developments," *IEEE Control Systems Magazine*, vol. 31, no. 2, pp. 44–62, April 2011.
69. Peterson EW and Hennessey JP. On the use of power laws for estimates of wind power potential. *Journal of Applied Meteorology* 1978; **17**: 390-394
70. Pullen, J., Doyle, J. D., & Signell, R. P. (2006). Two-way air-sea coupling: A study of the Adriatic. *Monthly weather review*, 134(5), 1465-1483.
71. Rawlings, J.O., (1988). *Applied Regression Analysis: A Research Tool*. Wadsworth and Brooks/Cole, 533 pp.
72. Rawn, B. G., Lehn, P. W., & Maggiore, M. (2006). Toward controlled wind farm output: adjustable power filtering. In *Power Engineering Society General Meeting, 2006. IEEE* (pp. 6-pp). IEEE.
73. Retallack C, Calhoun R, Fernando HJS, Rayner K, Stuart A, Sutton J and Hibberd MF. Flow and pollution transport during Wagerup 2006: a case study. *Meteorological Applications*, 2010; **17**: 269–278. doi: 10.1002/met.161
74. Rodriguez-Amenedo J, S. Arnaltes, and M. Rodriguez, "Operation and co-ordinated control of fixed and variable speed wind farms," *Renewable Energy*, vol. 33, no. 3, pp. 406 – 414, 2008.
75. Schlipf, David, Dominik Johannes Schlipf, and Martin Kühn. (2012a). "Nonlinear model predictive control of wind turbines using LIDAR." *Wind Energy*
76. Schlipf, D., Pao, L. Y., & Cheng, P. W. (2012b). Comparison of feedforward and model predictive control of wind turbines using LIDAR. In *Decision and Control (CDC), 2012 IEEE 51st Annual Conference on* (pp. 3050-3055). IEEE.
77. Scholbrock, A. K., Fleming, P. A., Fingersh, L. J., Wright, A. D., Schlipf, D., Haizman, F., & Belen, F. (2013). Field Testing LIDAR Based Feed-Forward Controls on the NREL Controls Advanced Research Turbine.

78. Sempreviva A, Barthelmie R and Pryor S. Review of methodologies for offshore wind resource assessment in European seas. *Surveys in Geophysics* 2008; **29**: 471-497.
79. Shimada, S., and T. Ohsawa, 2011: Accuracy and characteristics of offshore wind speeds simulated by WRF. *SOLA*, **7**, 21–24.
80. Shaw J W, Lundquist K J, Schreck J S, US DOE workshop report: Research needs for wind resource characterization, NREL, 2008.
81. Siggia, A, D., and J.M. Holmes. (1991). One pass velocity unfolding for VVP analysis. Preprints, 25th Radar Meteorology Conf., Paris, AMS., 882-884.
82. Smith DA, Harris M, Coffey AS, Mikkelsen T, Jørgensen HE, Mann J, Danielian R. Wind LIDAR evaluation at the Danish wind test site in HØvsØre. *Wind Energy* 2006; **9**: 87-93.
83. Smith A T, Campbell J T, Allard A R, Carrol N S, 2010: User's Guide for the Coupled Ocean/Atmospheric Mesoscale Prediction System (COAMPS) Version 5.0, Naval Research Laboratory.
84. Soleimanzadeh, M and R. Wisniewski, "Controller design for a wind farm, considering both power and load aspects," *Mechatronics*, vol. 21, no. 4, pp. 720–727, June 2011.
85. Soleimanzadeh, M., Wisniewski, R., & Kanev, S. (2012). An optimization framework for load and power distribution in wind farms. *Journal of Wind Engineering and Industrial Aerodynamics*.
86. Sørensen J, S. Frandsen, and N. Tarp-Johansen, "Effective turbulence models and fatigue reliability in wind farms," *Probabilistic Engineering Mechanics*, vol. 23, no. 4, pp. 531 – 538, 2008.

87. Spudic, M. Baotic, M. Jelavic, and N. Peric, “Hierarchical wind farm control for power/load optimization,” in *Proceedings of the Conference Science of Making Torque from Wind*, 2010.
88. Steinbuch, M., W. W. de Boer, O. H. Bosgra, S. Peters, and J. Ploeg, “Optimal control of wind power plants,” *Journal of Wind Engineering and Industrial Aerodynamics*, vol. 27, pp. 237–246, 1988.
89. Stotsky, A., & Egardt, B. (2012). Model-based control of wind turbines: look-ahead approach. *Proceedings of the Institution of Mechanical Engineers, Part I: Journal of Systems and Control Engineering*, 226(8), 1029-1038.
90. Suselj, K., and A. Sood, 2010: Improving the Mellor-Yamada-Janjic Parameterization for wind conditions in the marine planetary boundary layer. *Bound.-layer Meteor.*, **136**, 301–324.
91. Wagner R, Antoniou I, Pedersen SM, Courtney MS and Jørgensen HE. The influence of the wind speed profile on wind turbine performance measurements. *Wind Energy* 2009; **12**: 348–362. doi: 10.1002/we.297
92. Waldteufel P and Corbin H. On the Analysis of Single-Doppler Radar Data. *Journal of Applied Meteorology* 1979; **18**: 532–542.
93. Wang, N., Johnson, K. E., & Wright, A. D. (2012). FX-RLS-Based Feedforward Control for LIDAR-Enabled Wind Turbine Load Mitigation. *Control Systems Technology, IEEE Transactions on*, 20(5), 1212-1222.
94. Weisser, D. and Foxon, T. (2003), Implications of seasonal and diurnal variations of wind velocity for power output estimation of a turbine: a case study of Grenada. *International Journal of Energy Research*, 27: 1165–1179. doi: 10.1002/er.938
95. Wind Energy Technology Market report, US Department of Energy, 2010.
96. Wu, W., Zhang, B., Chen, J., & Zhen, T. (2012, July). Multiple time-scale coordinated power control system to accommodate significant wind power

penetration and its real application. In *Power and Energy Society General Meeting, 2012 IEEE* (pp. 1-6). IEEE.

97. Xia Q, Lin C, Calhoun R, Newsom R. Retrieval of urban boundary layer structures from Doppler lidar data. Part I: Accuracy assessment. *Journal of Atmospheric Sciences* 2008; **65**: 1, 3-20.
98. Xin L, Reuter WG. VVP Technique Applied to an Alberta Storm. *Journal of Atmospheric and Oceanic Technology* 1997; **15**: 587-592.
99. Xu Q, Liu S, Xue M. Background Error Covariance Functions for Velocity Wind Analysis using Doppler Radar Radial-Velocity Observations. *Quarterly Journal of the Royal Meteorological Society* 2006; **132**: 2887-2904.
100. Zhang, Da-Lin, Wei-Zhong Zheng, 2004: Diurnal Cycles of Surface Winds and Temperatures as Simulated by Five Boundary Layer Parameterizations. *J. Appl. Meteor.*, **43**, 157–169.

APPENDIX A

ATTRIBUTES AND CAPABILITIES OF THE *WINDTRACER* DOPPLER LIDAR

Lidar (Light Detection and Ranging) systems are similar to radar (Radio Detection and Ranging) systems, but use light instead of radio waves. Light has a number of benefits over radio waves for some measurement applications, the most significant being that lidar systems can make atmospheric measurements in relatively clear air using naturally occurring aerosol particles. The Wind Tracer is an infrared Doppler radar. Equivalent terms used in this literature include infrared Doppler lidar, Doppler lidar, lidar, and coherent lidar.

There are some similarities and differences between Lidar and Radar. The primary difference between lidar and radar is lidar uses much shorter wavelengths of the electromagnetic spectrum. Typically, radar can only provide atmospheric measurements when precipitation or visible clouds are present. Lidar does not suffer from this same limitation. Unfortunately, the reverse side of the coin is that radar does work in clouds, but lidar does not, due to the rapid attenuation and absorption of the light by the water particles (Doviak and Zrinc, 2001).

Additional benefits of Lidar are seen when a coherent laser is used as the light-generating source. The coherent laser beam has very little divergence, so whether measurements are made close to the laser source or far from it, the overall sample volume for any given range block is substantially the same size as any other. Also, the “pencil-beam” characteristic of a laser eliminates side lobe reflections, which are a source of problems in radar measurement.

The term Infrared Doppler Radar connotes the fact that, although there are clear differences as highlighted above, the sensor is similar in many respects to the more well-established microwave radar systems. In reality, the sensor can really be thought of as a

radar operating at a different frequency. The term coherent lidar refers to the fact that the sensor uses heterodyne, or coherent, detection through the use of a laser local oscillator to achieve increased sensitivity. The Wind Tracer utilizes a 1.6 or 2 μm laser source. This means the following:

- The transmitted light is infrared, so that it is invisible to the naked eye
- Detectable signals arise from transmitter light scattered by particles that are roughly 0.5-1 μm diameter and larger.
- The wavelength is greater than 1.4 μm , in what is known as the “eyesafe” wavelength region.

Basic Principles of Wind Tracer Operation: The Wind Tracer operates in the following manner. A pulse of laser light is generated and emitted into the atmosphere. As the light travels away from the system, small portions of the light are reflected back to the system by very small particles in the air called aerosols. This reflected light is detected and recorded. By examining the difference in time between when the pulse of light left the laser and when the reflected light returned, a distance to the particle that reflected the light can be determined. In addition, by measuring the frequency of the original pulse and the frequency of the reflected light, a shift in frequency can be measured (called a Doppler shift). The Doppler shift is induced by the component of the velocity of the particle directly towards or away from the laser. By analyzing the frequency shift, a direct measurement of the radial component of velocity of the aerosol particle is made.

Figure 84 highlights the basic principles of operation. The length of the pulses transmitted by the system is approximately 90 m and pulses are transmitted 500 times per second (a pulse repetition frequency, or PRF, of 500 Hz). This means that the beam is a

series of ‘pencils’ that are emitted every 2 milliseconds, each 90 m long and 10-30 cm wide, depending on the distance away from the system. Note that some other Wind Tracer systems use a PRF other than 500 Hz.

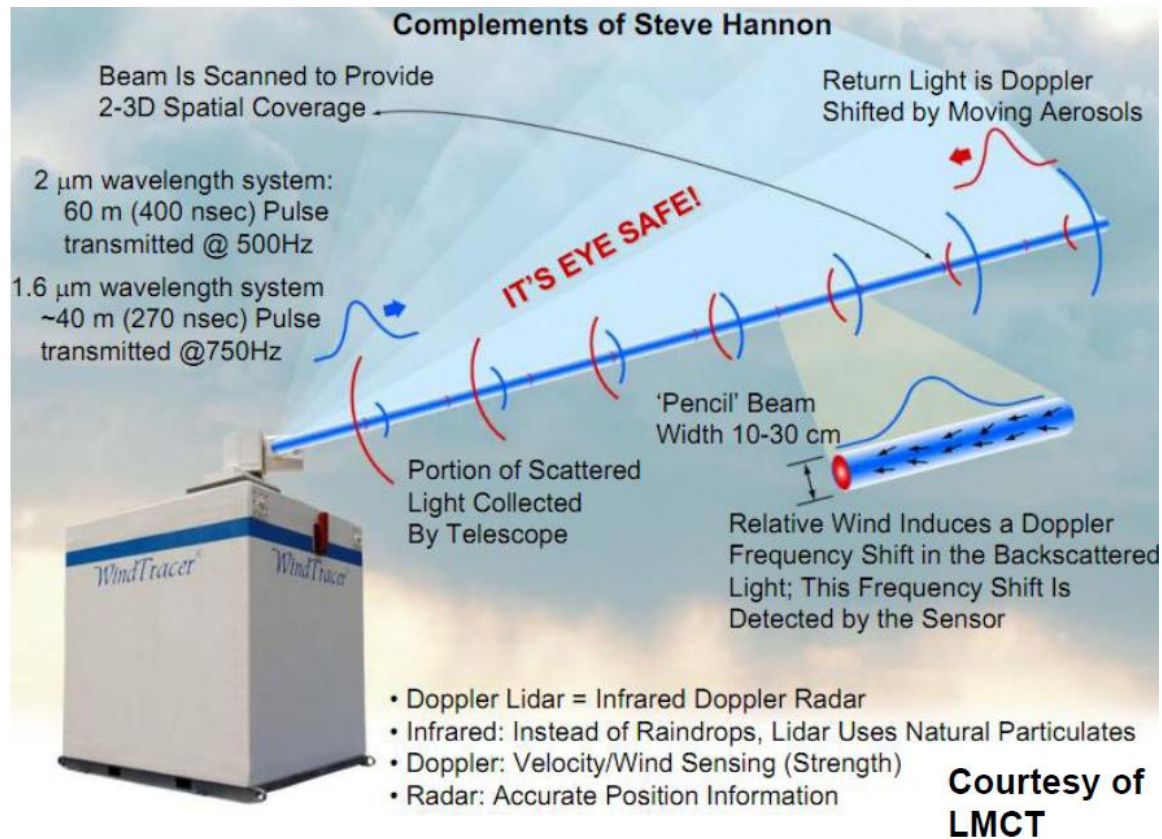


Figure 84. Coherent Doppler lidar basic operation principle.

The Doppler frequency shift is $\Delta\nu = -2v_r/\lambda$, where v_r is the radial velocity and λ is the operating wavelength. For a 1.6 μm operating wavelength, the frequency shift is roughly 1.25 MHz per meter/second of particle velocity.

Uses of Coherent Doppler Lidar

The Wind Tracer Doppler Lidar system is designed for moderate range, high spatial resolution wind field measurements. The system is ideally suited for range-resolved and

volumetric clear air wind-field mapping and the measurement of aerosol concentration levels over urban areas. Typical applications include:

- Airport Atmospheric Surveillance - wind shear detection, detection and measurement of terrain--induced wind shear and turbulence, local area forecasting, and wake vortex detection and tracking.
- Airline Safety And Efficiency – for airborne installations; clear air turbulence detection, detection of favorable wind conditions above or below the flight path.
- Environmental Monitoring - backscatter profiles for relative particulate density profiles; high resolution volumetric wind and aerosol measurement integrated with plume dispersion and hazard prediction models.

APPENDIX B

DUAL-DOPPLER LIDAR FOR WIND RESOURCE ASSESSMENT – CASE STUDY

Scanning Doppler lidars has gained significant interest in the wind energy community for wind resource assessment and characterization. Scanning Doppler lidars can provide spatial information of wind speed and direction across the entire wind farm domain. Since lidar provides radial velocity estimates (i.e., velocity component in the laser look direction), previous studies have shown that the accuracy of wind speed estimates in locations orthogonal to the wind direction are not up to standards for wind resource assessment. A pair of Doppler lidar systems can provide more accurate wind speed estimates over the entire wind farm domain, by measuring the wind from two different directions. This technique has been previously used in several meteorological studies and significant improvement in wind speed and direction estimates has been documented. In this Appendix, the logistics of performing the dual-Doppler lidar and single Doppler lidar for wind resource assessment are provided. The results from this study will be used to evaluate several aspects of wind resource assessment, such as wind shear, micro-siting and improvement of dual-Doppler wind speed and direction estimates compared to a single Doppler lidar. This study intends to further provide validation for using scanning lidars for accurate wind resource assessment.

I. Possible scanning strategy

Proposed scanning strategies based on lidar locations for complete coverage of wind farm domain (6km x 4km x 120 m) below, assuming GPS coordinates given in previous email.

A possible scanning strategy would be overlapping PPI stacks (with 12 individual PPI's for each lidar). The azimuth and elevation angles chosen could produce wind maps at 60, 90 and

120 m AGL for every 4.5 minutes, assuming a spatial resolution of 300 m x 300 m x 20 m per retrieval grid cell (boxes on plots below).

Table 19. 12 Elevation angles (deg) for stack of PPI's from each lidar's

Lidar 1					Lidar 2				
-0.30	-0.18	-0.06	0.13	0.26	0.33	0.41	0.54	0.65	0.71
	0.39	0.52	0.65	0.78		0.77	0.85	0.90	0.95
		0.91	1.04	1.43			1.00	1.10	1.31

Table 20. Azimuth Angles (deg) for stack of PPI's from each lidar's

Lidar 1	Lidar 2
285 to 50°, 5.5 deg/sec	240.5 to 5.5 deg, 5.5 deg/sec

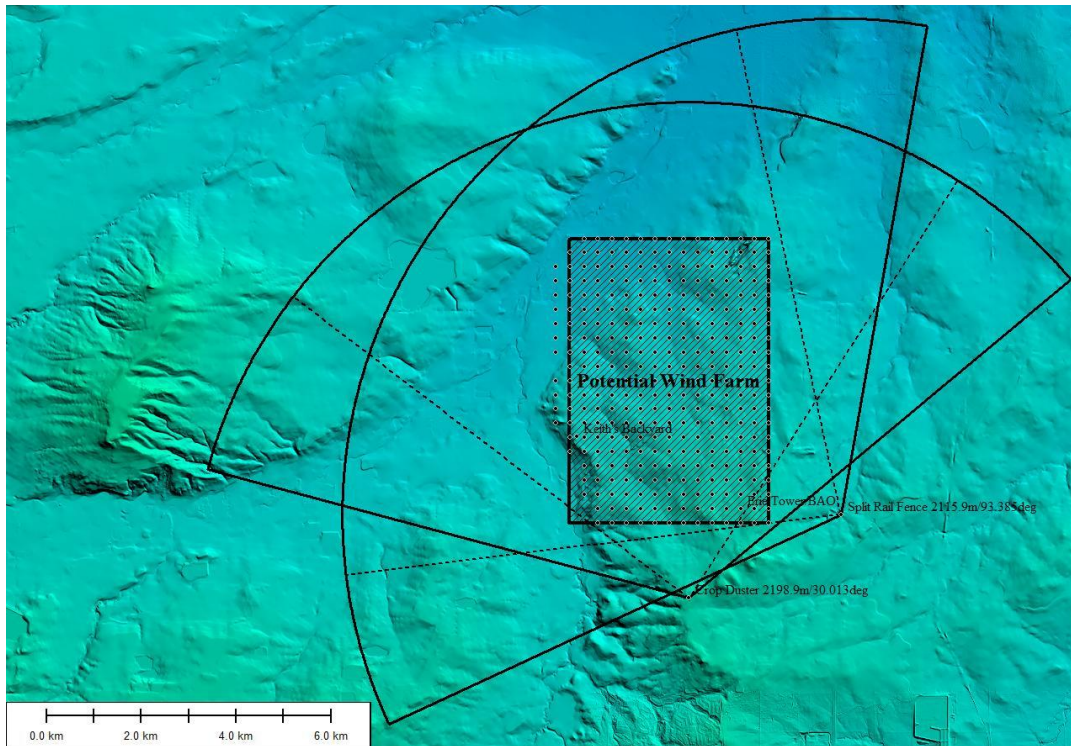


Figure 85. Potential Lidar locations for Dual-Doppler deployment covering a 6 km x 4 km potential wind farm domain. Lidar 1 is located at the crop-duster site and Lidar 2 is located near SRF site. [Assuming a max. lidar range of 10K with 95 m range-gate spacing]

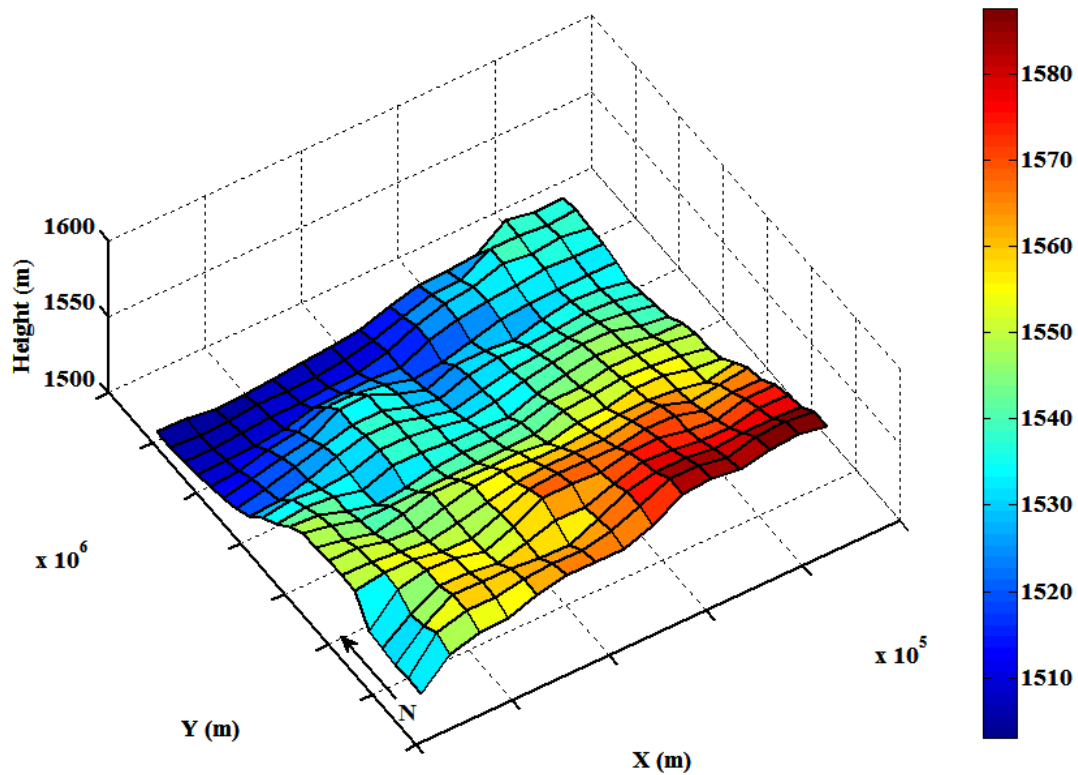


Figure 86. Terrain of the potential wind farm shown in Figure 1.

II. Analysis of proposed scanning strategy:

Based on 750 PRF with 150 pulses averaging (5 Hz data) and 5.5 deg/second scanning rate, each scan would take ~22.60 seconds to cover a 125 deg azimuth angle at one elevation angle (1.1 degree separation between beams). With 12 elevation angles, each volume stack would take approximately ~4.5 minutes.

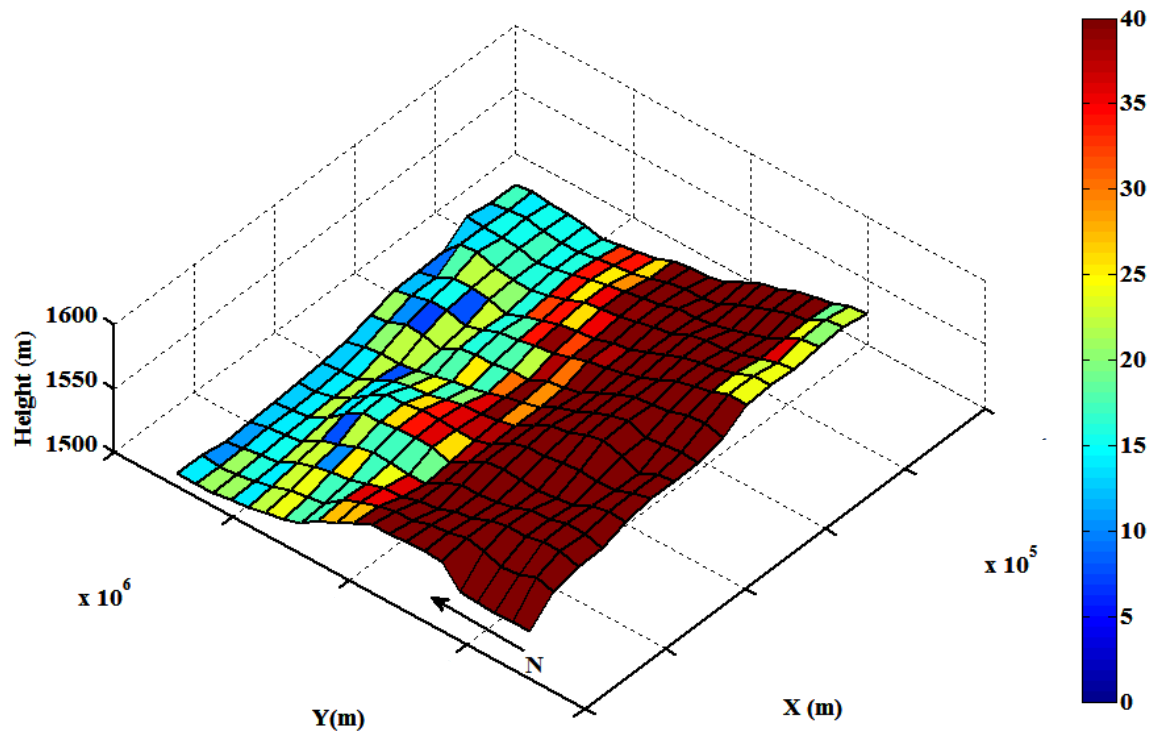


Figure 87. No. of radial velocity “hits” from both lidars in each 300 m x 300 m x 20 m grid cell box within 4.5 minutes over the wind farm domain shown in Figure 1 at 90 m (hub-height). [This result is for a terrain-following layer centered on 90 m AGL.] The number of samples in each grid might reduce after accounting for terrain-blockages or data filtering.

Figure 87 above shows the number of samples available (based on sweep rate, volume size, and PRF) to provide a vector retrieval for a given cell. This has been done to assess whether the results would be statistically stable. This is assuming a volume box of 300 x 300 x 20 m cell. The given scanning pattern and grid spacing (cell size) would produce a filtered result, including temporal smoothing (4.5 minutes), as well as spatial smoothing.

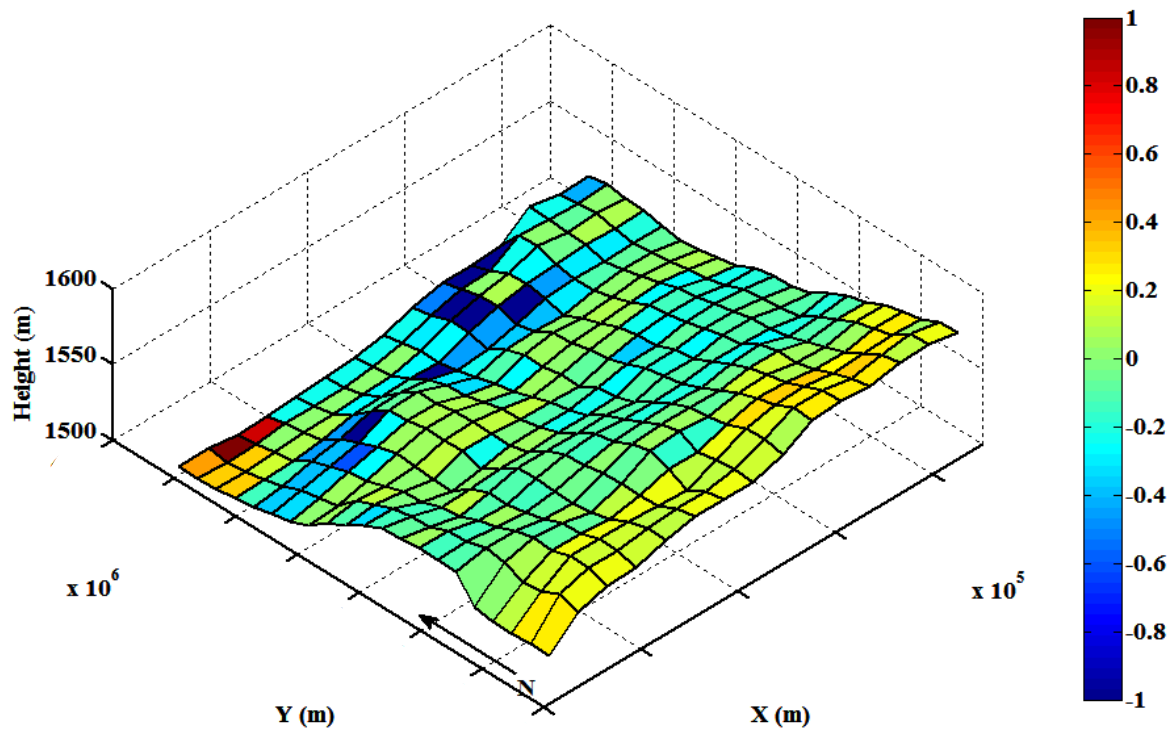


Figure 88. Ratio of “hits” from each lidar covering the wind farm region at 90 m AGL

Definition: Ratio in each grid cell = (Hits from Lidar 1 – Hits from Lidar 2)/ Total no. of points. Therefore, negative value indicates more hits from Lidar 2 at that particular grid cell and vice-versa. We want the ratio to be as close to zero as possible.

Figure 89 below shows the maximum temporal difference between “hits” inside a given grid cell (colored value) over 4.5 minute period (full PPI stacks from each lidar).

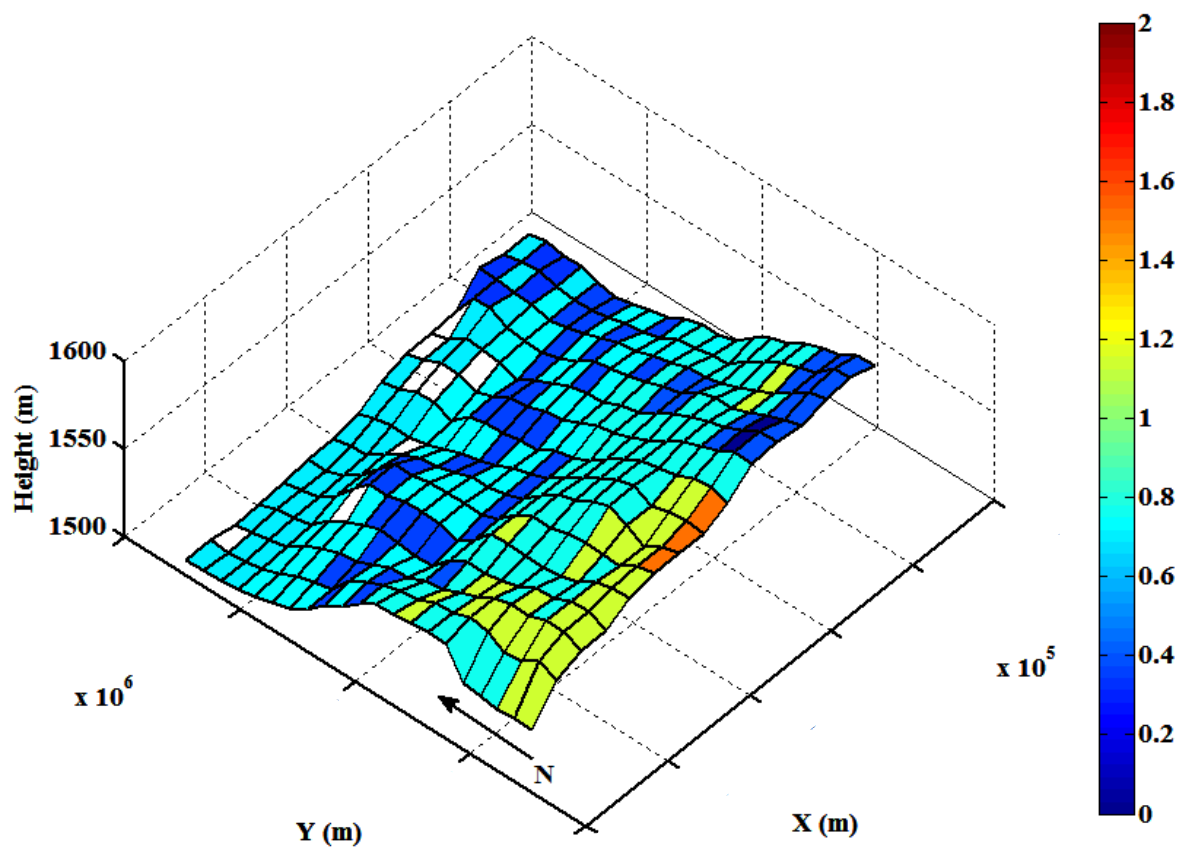


Figure 89. Maximal temporal difference (Δt) between hits at each grid cell in a 90 m AGL layer (± 10 m in vertical). Colors represent Δt in minutes. Data holes represent data only from one of the lidar's would be collected at that grid cell.

APPENDIX C

NREL 5MW WIND TURBINE PROPERTIES

Table 21. NREL 5MW - Mass and Inertia Properties

Length (w.r.t. Root Along Preconed Axis)	61.5	m
Mass Scaling Factor	4.536	%
Overall (Integrated) Mass	17,740	kg
Second Mass Moment of Inertia (w.r.t. Root)	11,776,047	kg-m ²
First Mass Moment of Inertia (w.r.t. Root)	363,231	kg-m
c.g. Location (w.r.t. Root Along Preconed Axis)	20.475	m
Structural Damping Ratio (All Modes)	0.477465	%

Table 22. NREL 5MW - Hub and Nacelle Properties

Elevation of Yaw Bearing Above MSL	87.6	m
Vertical Distance Along Yaw Axis from Yaw Bearing to Shaft	1.96256	m
Distance Along Shaft from Hub Center to Yaw Axis	5.01910	m
Distance Along Shaft from Hub Center to Main Bearing	1.912	m
Hub Mass	56,780	kg
Hub Inertia About Shaft Axis	115,926	kg-m ²
Nacelle Mass	240,000	kg
Nacelle Inertia About Yaw Axis	2,607,890	kg-m ²
Nacelle c.g. Location Downwind of Yaw Axis	1.9	m
Nacelle c.g. Location Above of Yaw Bearing	1.75	m
Equivalent Nacelle Yaw Linear Spring Constant	9,028,320,000	N-m/rad
Equivalent Nacelle Yaw Linear Damping Constant	19,160,000	N-m/rad/s

Table 23. NREL 5MW - Drive train and generator Characteristics

Rated Rotor Speed	12.1	rpm
Rated Generator Speed	1173.7	rpm
Gearbox Ratio	97:1	
Electrical Generator Efficiency	94.4	%
Generator Inertia About High-Speed Shaft	534.116	kg-m ²
Equivalent Drive Shaft Torsional Spring Constant	867,637,000	N-m/rad
Equivalent Drive Shaft Torsional Damping Constant	6,215,000	N-m/rad/s
Fully-Deployed High-Speed Shaft Brake Torque	28,116.2	N-m
High-Speed Shaft Brake Time Constant	0.6	sec
Height Above MSL	87.6	m
Overall (Integrated) Mass	347,460	kg
c.g. Location (w.r.t. MSL Along Tower Centerline)	38.234	m

Table 24. NREL 5MW - Control Characteristics

Corner Frequency of Generator Speed Low Pass Filter	0.25	Hz
Peak Power Coefficient	0.482	
Tip Speed Ratio at Peak Power Coefficient	7.55	
Rotor Collective Blade Pitch Angle at Peak Power Coefficient	0.0	°
Generator Torque Constant in Region 2	0.0255764	N-m/rpm ²
Rated Mechanical Power	5.296610	MW
Rated Generator Torque	43,093.55	N-m
Transitional Generator Speed Between Regions 1 and 1 1/2	670	rpm
Transitional Generator Speed Between Regions 1 1/2 and 2	871	rpm
Transitional Generator Speed Between Regions 2 1/2 and 3	1,161.963	rpm
Generator Slip Percentage in Region 2 1/2	10	%
Minimum Pitch For Ensuring Region 3 Torque	1	°
Maximum Generator Torque	47,402.91	N-m
Maximum Generator Torque Rate	15,000	N-m/s
Proportional Gain at Minimum Pitch Setting	0.01882681	sec
Integral Gain at Minimum Pitch Setting	0.008068634	
Pitch Angle at Which Rotor Power Has Doubled	6.302336	°
Minimum Pitch Setting	0	°
Maximum Pitch Setting	90	°
Maximum Absolute Pitch Rate	8	%/sec
Equivalent Blade Pitch Linear Spring Constant	1,069,020,000	N-m/rad
Equivalent Blade Pitch Linear Damping Constant	230,000	N-m/rad/s

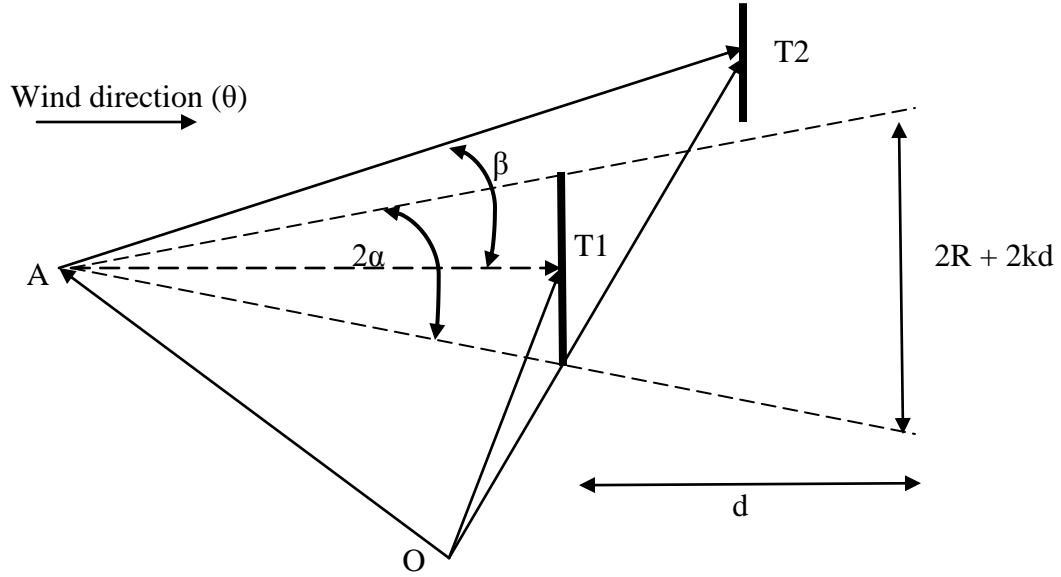
Table 25. NREL 5MW - Tower Properties

Tower-Top Height Above MSL	87.6	m
Tower-Base Height Above MSL	10	m
Water Depth (From MSL)	20	m
Overall (Integrated) Mass	522,617	kg
c.g. Location (w.r.t. Mudline Along Tower Centerline)	37.172	m
Structural Damping Ratio (All Modes)	1	%

APPENDIX D

UPWIND TURBINE DERIVATION

Derivation for upwind turbine detection based on lidar direction input. The sketch below shows the setup for any two turbines (T1 and T2, or vectors \mathbf{x}_1 & \mathbf{x}_2). Given the upwind wind direction (θ) from lidar measurements and any two turbines T1 and T2, the length of the vector \vec{AT}_1 is equal to R/k , where R is the rotor diameter and k is the wake decay constant (assumed to be equal to 0.106).



The vector \vec{OA} can be expressed as,

$$\vec{OA} = \mathbf{x}_1 - \vec{AT}_1, \quad (D1)$$

Therefore, the vector \vec{AT}_2 can be expressed as:

$$\vec{AT}_2 = \mathbf{x}_2 - \vec{OA} = \mathbf{x}_2 - \mathbf{x}_1 + \vec{AT}_1, \quad (D2)$$

If the angle, β ($0 \leq \beta \leq \pi$) between the vectors \vec{AT}_1 and \vec{AT}_2 is greater than α

(where, $\alpha = \tan^{-1}(k)$), T2 is not inside the cone. Therefore, β is given by:

$$\beta = \cos^{-1} \left(\frac{\left(\vec{AT_2} \right)' \vec{AT_1}}{L_{\vec{AT_2}} L_{\vec{AT_1}}} \right), \quad (\text{D3})$$

$$\begin{aligned} \vec{AT_1} &= (R/k \cos \theta, R/k \sin \theta), \\ \vec{AT_2} &= (x_2 - x_1 + (R/k) \cos \theta, y_2 - y_1 + (R/k) \sin \theta) \end{aligned} \quad (\text{D4})$$

Substituting, D4 into D3 gives the angle β , for any two turbines i and j :

$$\beta_{ij} = \cos^{-1} \left\{ \frac{(x_i - x_j) \cos \theta + (y_i - y_j) \sin \theta + R/k}{\sqrt{(x_i - x_j + R/k \cos \theta)^2 + (y_i - y_j + R/k \sin \theta)^2}} \right\}.$$